# Simulation of Self-Organized Growth Kinetics of Quantum Dots

(Simulation der selbstorganisierten Wachstumskinetik von Quantenpunkten)

vorgelegt von
Diplom-Physiker
Matthias Meixner
aus Berlin

von der Fakultät II – Mathematik und Naturwissenschaften
der Technischen Universität Berlin
zur Erlangung des akademischen Grades

‘Doktor der Naturwissenschaften’
- Dr. rer. nat. -

genehmigte Dissertation

Promotionsausschuss:

| | |
|---|---|
| Vorsitzender: | Prof. Dr. M. Dähne |
| Berichter : | Prof. Dr. E. Schöll |
| Berichter : | Prof. Dr. W. Richter |

Tag der wissenschaftlichen Aussprache: 18. Januar 2002

Berlin 2002
D 83

# Abstract

The growth of sub-monolayer islands in heteroepitaxial semiconductor systems is simulated by means of the Monte Carlo method. As the relevant processes, deposition, diffusion and nearest- and next-nearest-neighbor bonding is included. Diffusion processes occur with Arrhenius-like probability. To account for the elastic strain inherent to lattice mismatched growth, a self-consistently calculated elastic strain field is incorporated.

The influence of macroscopic growth parameters like temperature, flux to the surface during deposition, surface coverage and growth interruption time on size ordering and regular spatial arrangement of islands is analyzed. An optimal parameter range is identified to obtain both a regular spatial arrangement of dots and a narrow size distribution.

The transition from kinetically controlled growth conditions to thermodynamically controlled growth reached after long equilibration times is analyzed and a crossover in island size distributions between both regimes is found for different temperatures.

Simulations with anisotropic elastic strain parameters related to the $SiGe$ system are performed to verify the experimentally observed formation of island chains oriented along $Si(100)$ direction. Simulations are in good agreement with experimental data.

The growth of stacked quantum dot layers is considered by fully taking into account the self-consistently calculated elastic strain field. A transition from vertically correlated growth to anti-correlated growth with increasing buffer layer thickness is observed as well as an improved ordering with respect to island sizes with increasing number of deposited layers.

# Zusammenfassung

Das heteroepitaktische Wachstum von Inseln im sub-monolagen Bereich wird mittels der Monte Carlo Technik simuliert. Die für den Wachstumsprozess relevanten Parameter sind Deposition, Diffusion und nächste sowie übernächste Nachbarbindungen. Diffusionsprozesse geschehen mit einer Wahrscheinlichkeit, die über einen Arhenius Faktor bestimmt wird. Die für gitterfehlangepasstes Wachstum typische, elastische Verspannung wird über ein selbstkonsistent generiertes Verspannungsfeld in das Programm eingebunden, wobei auch eine kubische Anisotropie berücksichtigt werden kann.

Der Einfluß der makroskopischen Wachstumsparameter wie Temperatur, Materialfluß zur Oberfläche während der Deposition, Oberflächenbedeckung und Dauer der Wachstumsunterbrechung auf die Größenordnung und räumliche Anordnung der Inseln wird betrachtet. Dazu wird ein optimaler Arbeitsbereich im Parameterraum bestimmt zu dem sowohl eine reguläre räumliche Anordnung der Inseln als auch eine schmale Größenverteilung erzielt werden kann.

Es wird der Übergang von kinetisch kontrollierten Wachstumsbedingungen, wie sie während der Deposition vorherrschen, zu thermodynamisch kontrolliertem Wachstum, wie es nach langen Relaxationszeiten beobachtet wird, analysiert und ein Übergang zwischen den Wachstumsmodi beobachtet, bei dem sich die Größenverteilungen zu verschiedenen Temperaturen überschneiden.

Es wurden Simulationen mit einem anisotropen elatischen Verspannungsfeld, welches dem von $SiGe$ ähnlich ist, angestellt um experimentell beobachtete Strukturen in der Form von Inselketten, die entlang der $Si(100)$ Richtung orientiert sind, nachzuvollziehen. Die Simulationsergebnisse decken sich auf befriedigende Weise mit den experimentellen Befunden.

Das Wachstum von gestapelten Quantenpunkt Schichten wird betrachtet, wobei das selbstkonsistent berechnete Verspannungsfeld vollständig mitberücksichtig wird. Man findet einen Übergang von vertikal korreliertem Wachstum zu antikorreliertem Wachstum mit zunehmender Pufferschichtdicke sowie zunehmend bessere Größenordnung unter den Inseln mit zunehmender Anzahl der deponierten Schichten.

# Contents

# I.

# Introduction

Nature provides a seemingly endless variety of forms, patterns and shapes and it might take a similarly endless amount of time before scientists have unveiled the precise and detailed mechanisms which are ultimately responsible for their emergence.

As complex as these driving processes might be and indeed quite often they are chaotic in character, it turns out for most cases of 'natural' pattern formation that the resulting macroscopic structures are of suprising simplicity – some say beauty.

These simple patterns are a result of self-organisation. This term generally describes the spontaneous formation of stationary or time-dependent structures in open dissipative systems. The key feature of such systems is the existance of a hierarchy of dynamics. At the lowest level, for example, is the dynamics of single atoms or cells. Their behaviour usually is quite unpredictable. Stochastic processes dominate and the dynamics can be called complex at best. The Brownian motion of a single water molecule might serve as a handy example.

By moving towards larger spatial scales, self-averaging effects reduce the number of degrees of freedom and spatial correlations become apparent, like for instance, a directed flow of water molecules. Also, as an effect of self-averaging macroscopic parameters can be assigned to the flow like direction and velocity. By further increasing the length scales one might end up with the macroscopic picture of a deterministic, laminar flow of water in the shape of a vortex over the drain of a bath tub, which is a rather simple structure compared to the underlying, random motion of water molecules. The formation of a vortex after pulling the plug is actually a result of self-organisation.

The term 'self-organization' can, to some extent, be considered the guiding thread throughout this thesis. Ultimately, it can be held responsible for all the important results derived in the following chapters. Though a very special field of physics, namely the growth of quantum dots on a semiconductor surface under the influence of elastic strain [Sch98d, Bos99a, Bos99b, Bos00, Mei00a, Mei01c, Mei01a, Mei01b], is considered in this work, the observed self-organizing effects are by no means unique to this particular system and it might be instructive to have a closer look at pattern formation in self-organized systems from a more general point of view.

In the following a couple of examples from various fields of scientific endeavour are given to elucidate the universality of self-organized pattern forming processes in nature.

**Chemistry** A very prominent example of a pattern forming process is the so called Belousov-Zhabotinskii reaction [Zha64]. This reaction involves only a few organic

molecules and produces two morphologically different patterns – concentric cirular waves and expanding spiral waves – by a chemical reaction. The reaction is made visible by indicator molecules which turn blue or orange in color depending on the concentration of a certain reaction product.

It is very interesting to note that very similar patterns can be observed on certain forms of sea-shells and even the stripes on a zebra might be related to the Belousov-Zhabotinskii reaction, indicating a certain universality of self-organized, pattern forming processes.

**Biology** Self-organization also governs the evolution of a biological ecosystem, consisting of a certain number od species, some of them predators, some of them prey. As is shown in [Pim91] the evolution of a simple system consisting only of foxes, rabbits and grass, which is the feed for the rabbits, might result in a limit cycle motion of population numbers. The system is driven by periodic population explosions of rabbits due to few foxes and plenty of grass and a consecutive explosion in the population of foxes driven by a surplus of well fed rabbits.

Again, the basic processes of a rabbit gathering grass and trying to escape hungry foxes is a by all means complex process. But seen from a proper distance, the number of life rabbits performs a simple up and down motion in time[1].

**Society** It is claimed in [Kau95] that even in our society self-organisation processes play a vital role in the coexistance of people and in the adaption to changing external conditions in the form of economy and politics.

In physics self-organization has been realized in almost every discipline, from mechanics over optics to electronic transport [Sch87, Sch01, Mei97a, Mei97b, Mei97c, Mei98a, Mei98b, Mei99, Mei00c, Mei00b]. A common problem a scientist faces in dealing with self-organization processes is the choice of a proper hierarchy to describe the problem at hand.

A microscopic view, including many minute details can give a precise description of the dynamic processes which lead to self-organization. Thus, using a large number of microscopic parameters usually is the most general ansatz if it comes to predicting the influence of small parameter changes in the vicinity of a critical point where the dynamical behaviour of the system may change rapidly if certain parameters are tuned. But it is also the least general method, since one is restricted to the system the microscopic model has been designed for and the applicability to other systems is rather limited.

The opposite approach would be to neglect the microscopic fundament from the beginning and to model the dynamics of a given system by a limited set of macroscopic parameters like pressure or temperature to capture the essential features of the system. This approach usually includes a fair amount of educated guesswork but one might end up with differential- or rate equations which describe not only the considered system but a whole class of systems with similar dynamic behaviour, a so called universality class.

The applicability of this macroscopic ansatz sensitively depends on the amount of relevant parameters. It might work fine for large length- and time scales, where only few parameters are sufficient to describe the system. It might, however, be worthless on intermediate scales, where dynamics is determined by

1. The same, of course, goes for the foxes as well

a large number of independent or interacting parameters. Omitting one important parameter might result in an altogether different (and usually wrong) description of the system.

One more important difference exists between the two approaches concerning time scales. Since in macroscopic models no microscopic processes are considered and only parameters enter, which vary on much slower time scales due to self-averaging, statements about the systems long term evolution can be readily obtained. If one is pressed to extract the same information from a microscopic model, since, for example, no macroscopic description of the problem or only crude ones are accessible, one might be facing an unsurmountable obstacle. Though a microscopic model, in principle, would yield the same results as a good macroscopic one, it might take an unacceptably large number of microscopic steps to get there.

Now, this thesis considers a problem just of such character. The growth of quantum dots on a semiconductor surface per se is a microscopic process characterized by atomic interactions. The interaction potentials are rather complex and depend strongly on external parameters and the local atomic environment. Though a complete microscopic treatment is possible, for example by ab-initio methods, the long term evolution of such a system far from equilibrium is still a couple of orders of magnitude beyond the capability of even the most advanced computers available today.

On the other side, purely macroscopic descriptions exist in the form of rate equations, which, for example, can explain the temporal evolution of the average island size depending on temperature or coverage. However, these models are only valid for a limited parameter range and only explain a fraction of the whole growth process.

Still, the complete dynamics of quantum dot growth can be modeled and simulated even for reasonably long times by a method which combines the use of detailed, microscopic single particle events with the generality and speed of a macroscopic approach. This method is called Monte Carlo scheme and relies heavily on computational effort.

The basis of a Monte Carlo simulation are single particle events which do not attempt to cover all atomistic processes but are rather chosen from an intermediate level as characteristic, self-averaged parameters as for example the average binding energies to neighboring particles. To further reduce the complexity of the systems dynamics, all possible microscopic events are sampled by the Monte Carlo algorithm in dependence on few macroscopic parameters as temperature or the bulk elastic moduli.

In this sense the Monte Carlo simulation is placed between the purely microscopic approach of basic, single particle events and the general but not so precise ansatz of macroscopic models.

Of course, the success of a Monte Carlo simulation clearly depends on a proper choice of atomistic events as well as on their relation to the macroscopic parameters. To give a clear understanding of the Monte Carlo model used throughout this work chapter II deals with the atomistic processes in surface growth, explaining all the relevant microscopic effects which enter the Monte Carlo scheme. Since the term 'Monte Carlo' itself is quite a general one, an overview over different Monte Carlo methods is given as well and various Monte Carlo approaches used in surface science are compared.

Chapter III deals with the effect of self-organized growth that leads to the formation of quantum dot structures. The influence of external growth parameters like temperature, deposition rate or coverage on the resulting growth patterns is analyzed and an optimal parameter range identified with respect to size or-

dering and the spatial arrangement of dots.

Macroscopic rate equations for the size distribution of quantum dots on a semiconductor surface can be derived for the dynamic case of during or shortly after the deposition of quantum dot material. The predicted size distributions are, however, completely different from the predictions of thermodynamic equilibrium theory. Here, the IVth chapter makes full use of the Monte Carlo method being an intermediate technique. By performing a long time Monte Carlo simulation it can be shown that growth during deposition indeed agrees with the macroscopic rate equations derived for the dynamic case but then, in the course of equilibration, the size distribution swings towards the equilibrium distribution. It is shown that this process has a pronounced temperature dependence.

By incorporating the elastic anisotropy of the binary semiconductor compound $SiGe$ into the Monte Carlo simulation it will be shown in chapter V, that the regular arrangement of islands along chains oriented along the $(100)$ crystal direction, which can be observed in liquid phase epitaxy (LPE) experiments by [Sch98b] can be explained by a self-organization effect mediated by anisotropic strain. This strain is generated by the lattice mismatched growth of islands on the surface of a $Si$ crystal. Indeed, a very good agreement between the Monte Carlo simulations and the experimental results is found.

The last chapter VI considers stacked layers of quantum dots, so called quantum dot superlattices. In experiments it has been found that quantum dot growth is clearly influenced by the distribution of dots in buried layers beneath the surface. Depending on the thickness of the separating layer, dots tend to grow on top of each other, which is called correlated growth, or they grow anti-correlated. Again the strain field seems responsible for the correlation effects.

The transition from correlated to anti-correlated growth in dependence on the separating layer thickness can be reproduced by the simulations and important insights into the growth dynamics of stacked quantum dot layers can be gained from the Monte Carlo technique.

The whole of the following chapters will identify the Monte Carlo scheme as a versatile and potent tool for the modelling and simulation of quantum dot growth processes at semiconductor surfaces.

# II.

# Theory of Self-Organized Growth

In this work the growth of nanoscale surface structures is considered. From a very simplified point of view the process of growth is very much like spreading sand grains onto a table top. This analogy is, of course, only a very crude one and it does not take a lot of physical insight to spot the evident differences. Sand grains do not behave like atoms and a nanoscale surface is never as level as a table, but most importantly, it is very difficult to obtain little sand piles — preferrably of similar size and in a regular arrangement — by depositing sand uniformly on a table. However, this is just the effect that this work intends to explain since the emergence of quantum dots is observed in experiments dealing with atomic or molecular deposition.

The key words for understanding nanoscale structuring are *diffusion* and *particle interaction*, none of which is present in sand grains. There are, in fact, various ways of diffusive motion possible for atoms on a surface. For example, the deposited atoms will perform a more or less pronounced Brownian motion in dependence on temperature. This can be adapted in the sand example, and it is possible to make the grains diffuse by moving the table. Then, under certain conditions, the diffusion of the sand grains is indeed sufficient to observe pattern formation, like ripples or dunes. Unfortunately, the driving forces in these open systems need to be of a special form and no pattern forming process is known to exist for a purely stochastic motion of particles[1]. There exists, however, another structuring process for atoms that is not present in sand. The electro-chemical interaction of atoms of the same or different elements is responsible for effects on short lengthscales, like atomic bonding, up to long range interactions mediated by elastic strain. These features are ultimately responsible for the emergence of self-organized quantum dots of a well defined average size and lateral arrangement.

This chapter is split into two parts. To elucidate the basic physical concepts and, of course, to emphasize the complexity of self-organized growth mechanisms of nanoscale particles in contrast to the trivial macroscopic sand-on-table experiment, the first part explains a couple of relevant terms and effects in surface science that will be used throughout this text. In the second part an introduction to Monte Carlo techniques is meant to clarify the numerical and computational framework of the simulation routine that has been used to obtain most of the numerical results. Fur-

1. Random diffusion processes can be analyzed by means of the 'Langevin equation' or the 'Fokker-Planck equation'. Both equations do not exhibit instabilities that could lead to self-organized patterns unless some interactions or nonlinear potentials are introduced. This is rather fortunate since these physikal laws, inter alia, govern the distribution of oxygen in our offices.

ther on it will be discussed which of the afore mentioned effects have been included in the present work.

## II.1 Physics of growth on surfaces

### II.1.1 Deposition and diffusion

The first step towards the formation of quantum dots is the deposition of a certain material on a given surface. To this end a couple of technologically different procedures exist that are nevertheless very much alike, as far as the basic processes like deposition of material on the sample surface and diffuson are concerned.

Molecular beam epitaxy (MBE) belongs to the physical vapour deposition methods. The substance to be deposited is vaporized, and the molecules formed into a beam. This beam is under ultra high vacuum conditions directed towards a surface, where the particles condensate. To allow for diffusive motion of the deposited atoms, the sample is heated. Since no other chemically active substances are used in this form of epitaxy, deposition and diffusion is characterized by only the most basic processes. For this reason the growth technique of MBE is very convenient for theoretical modelling of growth.

On the other hand in chemical vapour deposition (CVD) the growth material is brought to the sample in form of a chemical carrier gas solution. A prominent example is metal organic CVD (MOCVD). Deposition occurs via chemical reactions at the sample surface. These reactions can be very complex and since the deposition rate depends sensitively on the concentrations of the various chemically active species the local growth kinetics can become quite involved. Furthermore, reactions usually occur both ways and consequently desorption is much more important in CVD than in MBE.

An other widely used epitaxial method is the liquid phase epitaxy (LPE) where the substrate is submerged into an oversaturated liquid solution. Material precipitates from the solution and is deposited on the sample. Here, again, the relevant deposition processes are basic but diffusion is widely aided by the presence of a liquid phase.

While in MBE and low pressure CVD the interaction of the growing surface with the ambient atmosphere is of minor importance, the theory of growth from dense phases like LPE or growth from the melt can become most complex. Here, for instance, a simultaneous solution of the Navier-Stokes equation and mass- and energy-transport equations is required.

Obviously, the technical details in various epitaxial setups can differ strongly. Nevertheless all methods used for epitaxy follow a simple scheme that consists of transporting material to the sample surface, depositing it and allowing for diffusion.

The deposition might be as simple as scattering atoms on the surface (as in MBE or related sputtering techniques) or complex and dominated by chemical reactions (as in CVD) but ultimately any of the above mentioned techniques ensures a certain *flux* of particles to the surface. The flux is the relevant quantity in terms of growth kinetics and its physical effect is basically independent of the applied method of deposition.

Once an atom is deposited on the surface it can travel from $A$ to $B$ on various paths (Fig.II.1).

Plain surface diffusion (Fig.II.1b) is an important mechanism in all growth techniques and consists of consecutive hops from one lattice site to a neighboring one. Since it is the energetically most favorable way of diffusion, at least for short distances, it generally dominates all other ways of transportation.

The movement of atoms through the bulk

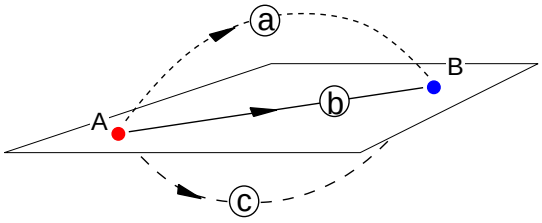


Fig. II.1: Possible ways of diffusion from $A$ to $B$: a - desorption, condensation process, b - surface diffusion, c - volume diffusion.

solid (Fig.II.1c) is usually negligible. Volume diffusion might, however, play a role on intermediate distances, if all other means of transportation are blocked, for example in samples with a capped surface.

Without the help of a chemical agent, desorption processes have to overcome a larger energy barrier than those responsible for surface diffusion. Nevertheless, desorption-condensation processes (Fig.II.1a) are relevant, especially in CVD where adatoms are desorbed from the surface by a chemical back-reaction, and provide an energetically favorable way of travelling long distances. In special cases, like in MBE growth of $GaAs$, desorption can become the dominant effect when at high temperatures arsenic evaporates.

### II.1.2 Growth classification

If material $A$ is deposited on material $B$ it is not at all clear in which way the growth will occur. Additionally, for a given material system the mode of growth depends on external parameters like temperature and pressure.

The simplest growth mode of heteroepitaxy, where one complete monolayer grows after the other is rather the exception than the rule. Under certain conditions rare gases grow layer-by-layer on graphite. Another example is the $Al_xGa_{1-x}N$ film growth on sapphire$(00.1)$ as reported in [Wic94]. This growth mode is also called Frank-Van der Merwe[Fra49] growth mode (Fig.II.2b).

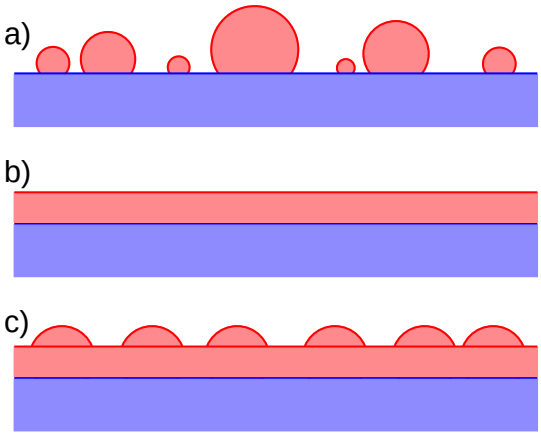


Fig. II.2: Important growth modes in epitaxy: a) Volmer-Weber growth mode, b) Frank-Van der Merwe growth mode, c) Stranski-Krastanov growth mode.

Conversely, in growth experiments with lead on graphite the lead does not form monolayers. It rather forms little droplets very similar to water droplets on a freshly sealed car top. This growth mode is referred to as the Volmer-Weber[Vol26] growth mode (Fig.II.2a).

Indeed, this analogy between lead and water droplets is worth pursuing. By defining the surface tensions for a liquid droplet on a plane surface as $\sigma_{sv}$, $\sigma_{sl}$ and $\sigma_{lv}$ for the interfaces solid/vapor, solid/liquid and liquid/vapor, respectively, one can show that the droplet forms an angle $\theta$ with the solid given as:

$$\cos\theta = \frac{\sigma_{sv} - \sigma_{sl}}{\sigma_{lv}}. \qquad \text{(II.1)}$$

For $\sigma_{sv} < \sigma_{sl} + \sigma_{lv}$ eq.(II.1) is well defined and the liquid is said to be non-wetting. Suprisingly, the same is true for solid lead on graphite, whereas for example xenon is wetting the graphite substrate and is growing layer-by-layer.

But then again solid droplets are not quite like a liquid. Solids come up with additional features like a well defined lattice constant and

certain elastic properties. This is the main reason for the existence of a third growth mode, the Stranski-Krastanov growth mode.

A monolayer of atoms adsorbed on a foreign substrate is subjected to two different effects. The adatom-adatom interaction within the layer favors a certain interatomic distance $a$. In general, the lattice constant of the substrate $b$ is different and the adatom-substrate interaction forces the monolayer towards lattice constant $b$. The lattice misfit $(a-b)/b$ then determines if the growth will occur in a commensurate or incommensurate way. If the adatom-adatom interaction is the dominant one, the adlayer will not adopt the lattice constant of the substrate and grow incommensurately.

For commensurate conditions the lattice misfit is zero or the adatom-substrate interaction is stronger than the interaction of adatoms. The deposited material grows with the same lattice constant as the substrate, i. e. epitaxially.

In contrast to liquids another problem arises, if more than just one monolayer is deposited. The energy gain for the first monolayer wetting the substrate might be large enough to enforce commensurate growth. The corresponding energy gain is proportional to the interface area. Now, every consecutively grown layer has to adopt a commensurate structure and the energy loss is proportional to the deposited volume of adsorbate. It is obvious that at some point the losses of energy outweigh the gain and a transition will occur from commensurate growth to the relaxed crystalline structure of the adsorbate. This transition is characterized by the appearance of *misfit dislocations* (Fig.II.3a) where additional atoms (green) are incorporated into the growing layer to relax elastic strain. This process of strain relief results in a Frank-Van der Merwe like growth mode.

There is, however, another way of reducing the strain generated by commensurate growth. Here, again, the growth continues up to a critical thickness basically without dislocations. Then, instead of the emergence of misfit dislocations the growth proceeds by the formation of small clusters of adsorbate, much like the droplets in Volmer-Weber growth (Fig.II.3b). Here, the strain relief is more efficient by the formation of islands; this growth mode is referred to as Stranski-Krastanov growth mode [Str39, RP98, Dou98].

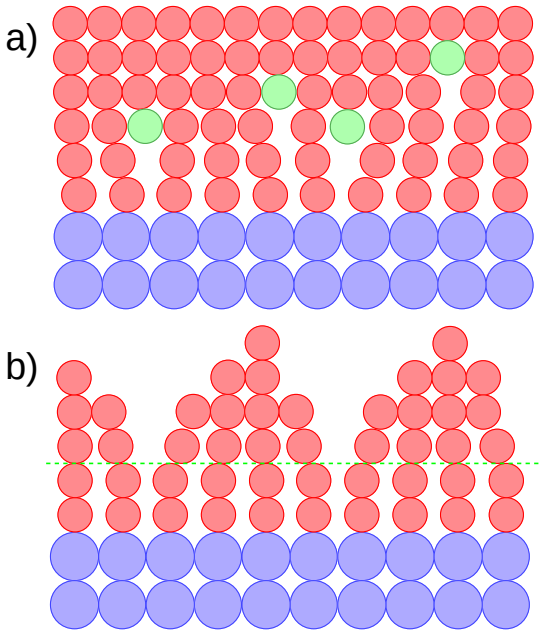


Fig. II.3: Strain relief by a) generation of misfit dislocations (green atoms) and b) Stranski-Krastanov growth mode. The green line marks the end of the wetting layer. Atoms of the substrate are blue, deposited material is red.

Stranski-Krastanov growth can be found in $InAs/GaAs$ growth [Kon98b], $PbSe/PbTe(111)$ [Pin98], in $SiGe/Si$ [Tei98] and $Ag/Si(100)$ [Par98] to name but a few.

### II.1.3 Nucleation and growth of quantum dots

Single atoms that have been adsorbed to the surface are called *adatoms.* Depending on temperature these adatoms will diffuse on the surface with a probability for single hops given by eq.II.2 [Sch97b]. They will continue to diffuse until they find another adatom where they can stick.

The additional binding energy between the two adatoms reduces the diffusion probability dramatically. If temperature is low enough, it is not likely that the adatoms will dissociate again and an island has *nucleated.* For higher temperatures the bond between two adatoms might not be stable for long; then the *critical nucleus* for a nucleation process needs to be larger than just one adatom. It is then likely that a critical nucleus of two adatoms might be suited to allow nucleation of an island if a third adatom attaches.

The so formed islands or terraces can grow by the further collection of other adatoms. During this growth process nucleation will become less important since the existing islands will efficiently compete for incoming atoms. Experimental evidence of nucleation and quantum dot growth is given in [Zha99, Kam94].

At some point the islands will coalesce and yield a complete layer. This process is characteristic of Frank-Van der Merwe growth. Up to the completion of the first monolayer the system is said to have a sub-monolayer coverage. Sub-monolayer coverages are defined as the relation of the number of atoms deposited per unit area to the number of atoms that would cover this area completely. It is usually given in units of percent.

If, however, strain is a relevant factor, the lateral growth of islands might be energetically inconvenient before coalescence becomes important. Then a transition occurs from 2D-growth to three dimensional or vertical growth and islands become droplets or dots [Ter94, Shk98]. The critical layer thickness for this transition is investigated in [Leo94] for $InAs$ dots on $GaAs$ and in [Spr94] for $EuTe$ on $PbTe(111)$.

The actual shape of these dots depends very sensitively on the elastic properties of the adsorbate and may change during the growth process [Gar97, Dar99b]. Discussions of equilibrium shapes of quantum dots can be found in [Mol96, Rob98, Mol98, Lee98b, Wan99] and for $InAs$ on $GaAs(001)$ in [Peh96]. Physical properties of dots on vicinal surfaces in the $InAs/GaAs$ system are examined in [Evt99] and pyramid-like quantum dots are discussed in [Gru95].

If quantum dots are grown in Stranski-Krastanov growth mode the dots have to relax strain, which is only partly possible by a proper choice of shape. In large dots it is very likely that dislocations will appear, additionally. The emergence of dislaoctions as a way of relaxing strain is considered in [Gha89, Mad96]. Dislocations are, however, an undesired effect, since they influence the physical properties of the dots considerably. Instead technological applications demand dislocation free or *coherent* dots.

At low temperatures an effect similar to the 2D – 3D transition can be observed in systems that would grow layer-by-layer at higher temperatures. This effect is called kinetic roughening and is intimately connected to the Schwöbel effect that will be discussed in section II.1.4.b. The Schwöbel effect is basically an extra energy barrier that prevents adatoms from falling off island edges. If adatoms arrive atop an island, they are likely to stay on top because of the Schwöbel barrier, which is even more efficient in low temperature systems. Thereby the nucleation rate in the second growth layer is increased and consecutive layers begin to grow long before the lower lay-

ers are complete [Orr92, Hey97, Ros98].

This, of course, is a kinetic effect and a considerably smoother growth morphology can be achieved by introducing a *growth interruption* that gives the adatoms enough time to find their equilibrium positions [Kam96, Shc99a, Liu00].

In this context it has to be mentioned that the in some sense opposite effect to kinetic roughening – the induced layer-by-layer growth in systems that would otherwise show 3D islanding – can be obtained by the use of *surfactants*. These surfactants are adsorbed impurities that float on the surface during the whole growth process. Their effect is to change local kinetic processes like attachment and detachment to islands and they might even have an influence on nucleation processes [Hwa98, Kan95].

The smoothing action of surfactants can be quite impressive as in the growth of $Ge$ on $Si$. Without surfactants $Ge$ grows in the Stranski-Krastanov growth mode with a wetting layer thickness of three monolayers at 700K. If a surfactant like Antimony or Arsenic is used, the layer-by-layer growth is extended up to thirty monolayers before 3D dots emerge [Cop90].

The impact of surfactants on the growth process have also been verified in Monte Carlo simulations with and without strain in [Liu01] and [Liu99a], respectively.

### II.1.4 Edge effects

Now, the main features of growing adsorbate have been discussed. To construct a good simulation code of heterogrowth, one has to consider a couple of other effects that are caused by the atomic interaction and influence the diffusive motion of adatoms in a specific way.

The diffusion of sand grains on a rough surface is only hindered by the height of the energy barrier they have to surmount with every hop. This is not so for adatoms. Due to interaction phenomena the diffusion barrier height varies in dependence of the local surounding and even depends on the locus to where the adatom is moving, since the considered particles are of a quantum physical nature.

The atomic structure of the surface generates a corrugated potential landscape for adatoms. At least for low temperatures adatoms will be located at the energy minima, the so called *easy sites*. To make a transition from one easy site to another, they have to cross a free energy barrier $E_s$. According to the Gibbs-Boltzmann formula the probability $p$ for an adatom having enough energy for such a transition is

$$p = \nu_0 \exp(-E_s/k_B T) \qquad \text{(II.2)}$$

where the attempt frequency $\nu_0$ is of the order of a typical atomic frequency ($\sim 10^{13} s^{-1}$).

Energy barriers for adatom homodiffusion on (111) and (100) surfaces of $Au$, $Ag$ and $Ir$ have been obtained from first-principles calculations using the full potential linear muffin tin orbital technique [Boi95]. Values range from $0.14 \pm 0.02$eV for Ag(111) to $1.39 \pm 0.04$eV for Ir(100). Results for adatom self-diffusion on $Pt(111)$ are presented in [Boi98]. If strain is present, the diffusion barriers change as is shown in [Rat97b] for $Pt(111)$ and $Ag(111)$.

Ab initio results for microscopic growth processes in $GaAs$ homoepitaxy are derived in [Kra98, Kra99]. A density functional theory derivation of hopping rates is given in [Rat98].

#### *II.1.4.a Edge diffusion*

If other adatoms are present in the immediate vicinity of the hopping atom, the processes become more complex and, for this matter, different from sand diffusion. Here, the diffusional barrier is increased by a number of nearest and, possibly, next nearest neighbor bonds $E_n$. For the motion of an atom away

from its neighbors where a bond has to be broken (Fig.II.4), the diffusion barrier will change from $E_s$ to $E_{\text{off}} = E_s + E_n$.

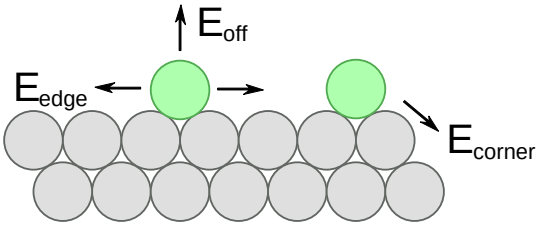


Fig. II.4: Possible moves for adatoms (green) at an island edge (top view). Characteristic energy barriers for detachment, edge- and corner diffusion are labeled $E_{\text{off}}$, $E_{\text{edge}}$ and $E_{\text{corner}}$, respectively.

On the other hand, if the atom diffuses along a step, some of the bonds to (next-)nearest neighbors will stay intact. Consequently, the energy barrier for diffusion along an edge $E_{\text{edge}}$ will in general be smaller than the barrier associated with detachment. The same is true for diffusion around corner atoms even if the lowering of the barrier is less pronounced here ($E_{\text{off}} > E_{\text{corner}} > E_{\text{edge}}$).

A more detailed discussion of ways to deal with the energetics of jumps of adatoms in the presence of neighboring atoms will be given in the next section on Monte Carlo methods.

### *II.1.4.b Schwöbel barrier*

A similar effect can be found for atoms atop a step edge. An adatom willing to step down has to break bonds in the upper layer and go through an uncomfortable position (Fig.II.5c), where it has only few neighbors. The same holds, by the way, as well for an adatom crossing the step on its way up.

This effect was first observed by Ehrlich and discussed by Schwöbel in terms of its consequences for crystal growth. In Fig.II.5a the potential as experienced by an atom at the step is shown. The additional energy an atom has

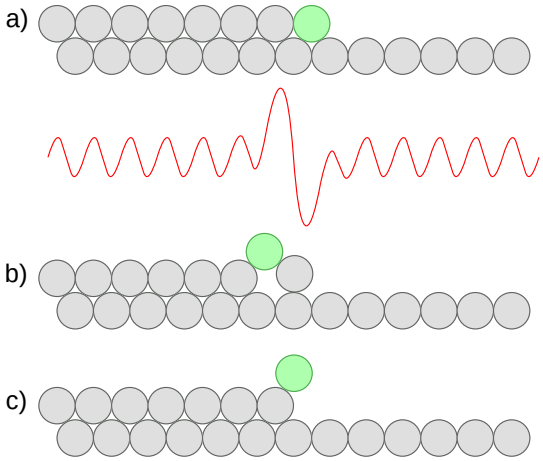


Fig. II.5: a) Adatom (green) at a step edge experiences the Schwöbel-barrier. The red line sketches the potential felt by the adatom. b) and c) show ways to overcome the edge barrier.

to gain to overcome a step is called (Ehrlich-) Schwöbel barrier.

Depending on the material there might be an energetically more favorable way to cross the step (Fig.II.5b). Here, the atom atop the step edge pushes the outermost atom of the upper step layer aside and slips down into the formed vacancy. This behaviour can ge found, for example, in $Au$-layers with $(100)$ orientation. The jump-process, on the other hand, is favored in most semiconductor materials and can also be observed in $Cu$, $Ag$ and $Ni$ [Sto94].

The Schwöbel barrier seems to be responsible for the stability of atomically sharp tips as they are used, for instance, in scanning tunneling microscopy. A stabilizing effect on certain facets of three dimensional nanostructures has been found by means of Monte Carlo simulations in [Köh00, Tür96].

In [Ter94] it is shown that the Schwöbel barrier has a major impact on the critical island size, beyond which the growth kinetics changes from two dimensional island growth to the formation of three dimensional quantum

dots.

*II.1.4.c Kick-out effect*

A similar process as the exchange mechanism in crossing the Schwöbel barrier (Fig.II.5b) is also observable during the deposition of atoms with MBE techniques. Here, the atoms arriving at the surface carry a comparatively high kinetic energy. If they happen to hit a step edge, the transfer of energy might be sufficient to break the bonds of the edge atom. As a result the arriving atom will be incorporated into the upper layer as shown in Fig.II.6.

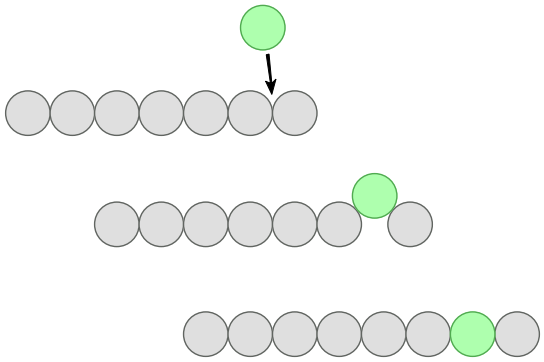

Fig. II.6: 'Kick-out'-effect at step edges during MBE deposition.

This effect is called 'kick-out' effect and is, in contrast to the Schwöbel exchange mechanism, independent of the material but only relevant in MBE.

### II.1.5 Anisotropy and surface reconstruction

So far we have assumed the surface to be homogeneous and isotropic. Unfortunately, almost all atomic surfaces exhibit features that result in an anisotropic diffusion of adatoms. In this context we have to differentiate between forms of anisotropy that affect diffusion. As far as this work is concerned, the most important forms of anisotropy are the diffusional anisotropy that arises with reconstructed surfaces and the elastic anisotropy that leads to an anisotropic extension of surface stress. Both forms of anisotropy will be discussed in the following.

Apart from these forms of anisotropy one might obsere anisotropy of sticking. Here, the nearest neighbor bonds are different in different directions. This effect is, for example, present in $Si$ on $Si(001)$. Under certain conditions one observes the formation of elongated sub-monolayer islands during MBE growth [Mo91, Mo92]. It is argued that this effect is due to the sticking anisotropy[2]. Sticking is much easier at the end of the dimers that make up the $2 \times 1$ reconstructed surface of $Si(001)$ than along a dimer side (Fig.II.7a).

If a solid is cut to obtain a surface of a certain orientation, the surface atoms lose part of their neighbor bonds. The now unsaturated bonds are called *dangling* bonds. In most cases it is energetically favorable to connect two dangling bonds. This is only possible, if the atoms at the surface change from their bulk positions to distinct places that allow for saturation of open bonds. Usually, the now reconstructed surface has a lower symmetry than a planar section of the bulk. In terms of diffusion it has to be remarked that a reconstructed surface has certain designated directions in which diffusion processes are more likely to happen than in others.

$Si(001)$, for example, has a $2 \times 1$ reconstructed surface (Fig.II.7a) where dimers form at the surface. Fig.II.7b shows a sketch of the potential landscape of the reconstructed surface. It is obvious, that diffusion along the dimer rows is energetically easier than diffusion across the rows, since the energy barriers in the trench are low. This anisotropy due to

2. Diffusional anisotropy is, however, present in $Si(001)$ as well. In fact diffusion along the dimer rows of the $2 \times 1$ reconstruction is strongly enhanced

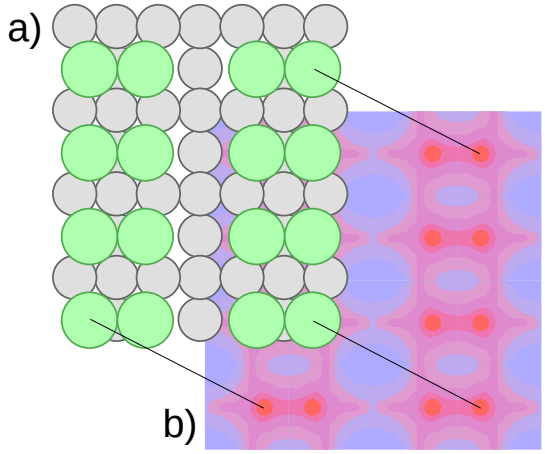


Fig. II.7: a) (2×1) surface reconstruction of $Si(001)$. Reconstructed surface dimers in green. b) Sketch of the corresponding potential landscape (blue - low, red - high potential).

the surface reconstruction is referred to as diffusional anisotropy.

Surface reconstructions can, however, be quite complex giving rise to equaly complex, anisotropic surface diffusion.

There is evidence, for example, that for phosphorous-terminated $InP(001)$ grown by MOVPE a coexistance of different surface reconstructions can be found [Vog99b, Vog99a].

For the growth of $Pb$ on $Cu(001)$, for example, islands with a structure similar to a surface reconstruction emerge. The energetic minimum favours $(\sqrt{61} \times \sqrt{61})R\tan^{-1}(5/6)$ islands before a transiton to a square phase is induced with increasing growth temperature [Li93].

### II.1.6 Elastic anisotropy

Until now the diffusion of adatoms has been discussed to some extent. This seems justified, since diffusion is one of the key ingredients towards pattern formation. The second ingredient relevant to self-organized growth is the elastic strain that is generated if materials with a different lattice parameter are connected epitaxially. The strain makes itself felt by an isotropic or anisotropic contribution to the binding energies. This contribution influences maximum island sizes and the shape of islands on a short length scale and island-island interaction that is important for spatial ordering of islands on a long-range scale [Rat94a, Rat96, Dar97, Orr92]. An experimental techniques to quantify elastic strain in quantum dot structures by means of transmission electron microscopy (TEM) is presented in [Car98].

To estimate the effect of strain on the binding energy, it is helpful to consider the interaction of a pair of atoms. For large separations the interaction is attractive but becomes repulsive for very short distances. A corresponding atomic interaction potential is shown in Fig.II.8I. For a certain distance the potential has a minimum, which defines the equilibrium distance of the pair of atoms. This distance is equivalent to the lattice constant in a relaxed crystalline solid.

If the pair of atoms is forced to leave its equilibrium positions by, for example, epitaxial growth on a substrate with a different lattice constant, the interaction between the pair of atoms will decrease and with it the binding energy. Thus, in a strained adsorbate the atoms are more loosely bound than in an equilibrium crystal. Strain also reduces diffusion barriers and allows adatoms to diffuse faster.

If growth on a strained surface is considered as is the case for growth on a wetting layer in the Stranski-Krastanov growth mode, the interatomic distance between surface atoms is already different from the equilibrium distance. Now a change in the relative distance caused by strain shifts the atoms closer to or farther from their equilibrium positions. In this case it is important to differentiate between compressive and tensile strain, since now the contribution of strain to the binding

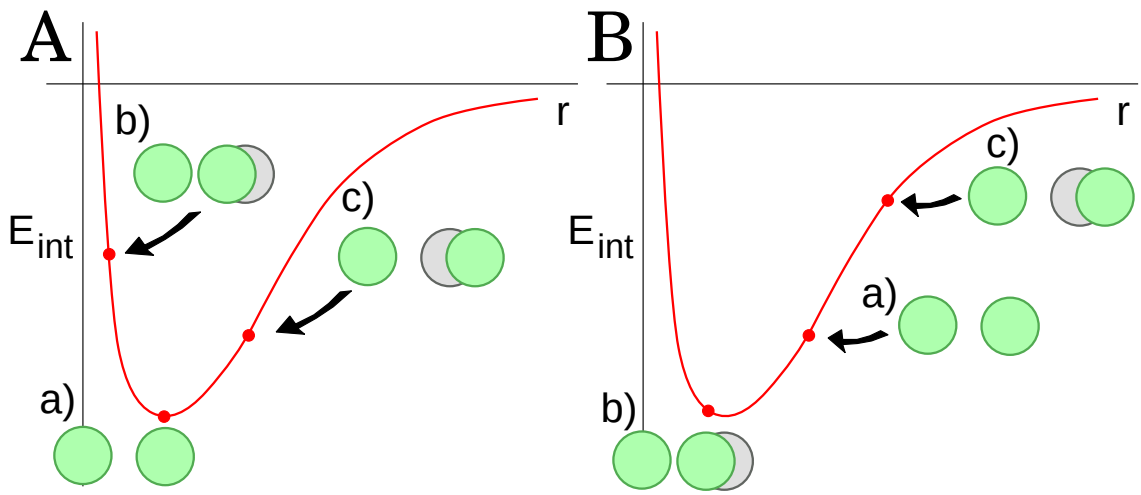


Fig. II.8: Interaction potential of a pair of atoms. A - effect of strain in a relaxed pair of atoms. a) equilibrium distance, b) compressed and c) extended pair. B - same as A for a pair of atoms under external tension.

energy has a different sign in each of the two cases. For certain surface reconstructions this effect can also be observed in unstrained surfaces, as for $In$ on $GaAs(001)$-c$(4\times4)$, where the energetic change of adsorption and transition sites increases the diffusion barrier for moderate, tensile strains.

In the next step the problem arises of how to calculate the elastic strain fields that are present in heteroepitaxy. The easiest approach is to make up a heuristic model that captures the main features of strain. Bose [Sch98d, Bos99a, Bos99b, Bos00] has explained self-organized growth of regularly arranged island arrays with a sharp size distribution by means of a purely heuristic model. Here, the strain energy correction decayed linearly with the distance $r$ from the island boundary. Its absolute value was proportional to the island size with a square symmetry of the strain field that was centered about the center of mass of the island, to relate to the geometry of a sqare lattice surface. Despite the fact that, particularly, the simple geometry of the strain field is not able to cope with unusually shaped islands, the obtained results conform to a lot of experimental findings [Nöt96, Abs96, Wan97]. Furthermore, the heuristic model has the great advantage of computational simplicity.

To find a more physical motivation to construct the strain field, one could start from an atomistic point of view and model the actual atom-atom interaction potentials. This would, unfortunately, necessitate a detailed knowledge of, for example, surface reconstructions, potential landscapes and temperature dependencies of energy barriers. Though, it would give rather precise results of elastic effects, this method would make any calculation very complicated and, thus, render it useless for long-time simulations, where several million steps of single adatom movements have to be considered.

There is, however, a trade off between precise atomistic calculations and purely heuristic models. By using elasticity theory of macroscopic solids one of course neglects the complexity of atomic interactions but is still able to catch the important features of elasticity like scaling with size, sensitivity to shape and par-

ticular material parameters and anisotropic effects [Dow97, Pry98]. Though, for very small islands elasticity theory might give results different from atomistic calculations, for larger islands both theories should converge [Ter95]. The fact that the elastic equations are rather simple to evaluate numerically and the superposition principle for contributions to the strain field makes this method of strain calculation a good candidate for a Monte Carlo simulation.

#### *II.1.6.a Isotropic elastic strain*

To calculate a strain field for the isotropic surface it is helpful to revisit the problem of the origin of strain. As has been mentioned above, strain is caused by the interaction of the surface atoms and the adsorbate atoms, which grow commensurately, that is with a non-equilibrium lattice constant. The resulting strain field is generated by forces that act all along the interface between surface and adsorbate.

By applying elasticity theory of continuum mechanics the problem can be defined somewhat easier. To obtain a homogeneous compression or dialation, it is sufficient to assume forces acting only along the border of an island that has formed commensurately on the surface or the wetting layer. The problem then simplifies to calculating the strain field for a line force acting on a given length of the boundary, say the linear extension of a lattice site, to obtain the whole strain field of the island by linear superposition of the line forces for the whole boundary (see Fig.II.9).

Now the problem at hand is to find the strain field of a force $\mathbf{F}$ acting on point $P$ in parallel with the surface[3] (see Fig.A.1 on page 99). This problem is well known in elasto mechanics [Saa74] and is called Cerruti's problem. This problem can be solved by a proper choice of a scalar Lamés strain potential and a Galerkin vector potential to obtain the displacements $\mathbf{u}(\mathbf{r})$. Differentiation with respect to the coordinates delivers the tensor components of the strain field $\varepsilon(\mathbf{r})$. For a more complete derivation see Appendix A. As a result one finds:

$$\begin{aligned}
\varepsilon_{xx} &= \frac{|\mathbf{F}|\,x}{2\,\pi\,\mu\,r^3}\left[-\frac{3}{r^2}(x^2-\nu(y^2+z^2))+\right.\\
&\qquad \frac{1-2\nu}{(r+z)^2}\left((1-3\nu)r^2-\right.\\
&\qquad \left.\left.-\frac{3r+z}{r+z}(y^2+\nu x^2)\right)\right]\\
\varepsilon_{yy} &= \frac{|\mathbf{F}|\,x}{2\,\pi\,\mu\,r^3}\left[-\frac{3}{r^2}(y^2-\nu(x^2+z^2))+\right.\\
&\qquad +\frac{1-2\nu}{(r+z)^2}\left((3-\nu)r^2-\right.\\
&\qquad \left.\left.-\frac{3r+z}{r+z}(x^2+\nu y^2)\right)\right]\\
\varepsilon_{zz} &= \frac{|\mathbf{F}|\,x}{2\,\pi\,\mu\,r^3}\left[-\frac{3}{r^2}(z^2-\nu(x^2+y^2))-\right.\\
&\qquad -\frac{\nu(1-2\nu)}{(r+z)^2}\left(4\,r^2-\right.\\
&\qquad \left.\left.-\frac{3r+z}{r+z}(x^2+y^2)\right)\right]\\
\varepsilon_{xy} &= \frac{|\mathbf{F}|(1+\nu)\,x}{2\,\pi\,\mu\,r^3}\left[-\frac{3x^2}{r^2}+\frac{\nu(1-2\nu)}{(r+z)^2}\right.\\
&\qquad \left.\left(-r^2+x^2+\frac{2\,r\,x^2}{r+z}\right)\right]\\
\varepsilon_{xz} &= \frac{3\,|\mathbf{F}|(1+\nu)\,z\,x^2}{2\,\pi\,\mu\,r^5}\\
\varepsilon_{yz} &= \frac{3\,|\mathbf{F}|(1+\nu)\,x\,y\,z}{2\,\pi\,\mu\,r^5}. \qquad \text{(II.3)}
\end{aligned}$$

Here, the Lamé coefficients $\lambda$ and $\mu$ are used. Also common in literature is the use

3. Strictly speaking, we would need to consider a line force acting on a short, straight line element. Since we assume that the line element is very short compared to the island extension, we can as well assume an equivalent point force. Under these conditions the strain field of a point and line force are only different in the immediate vicinity of the origin. One lattice constant away, the difference is already negligible.

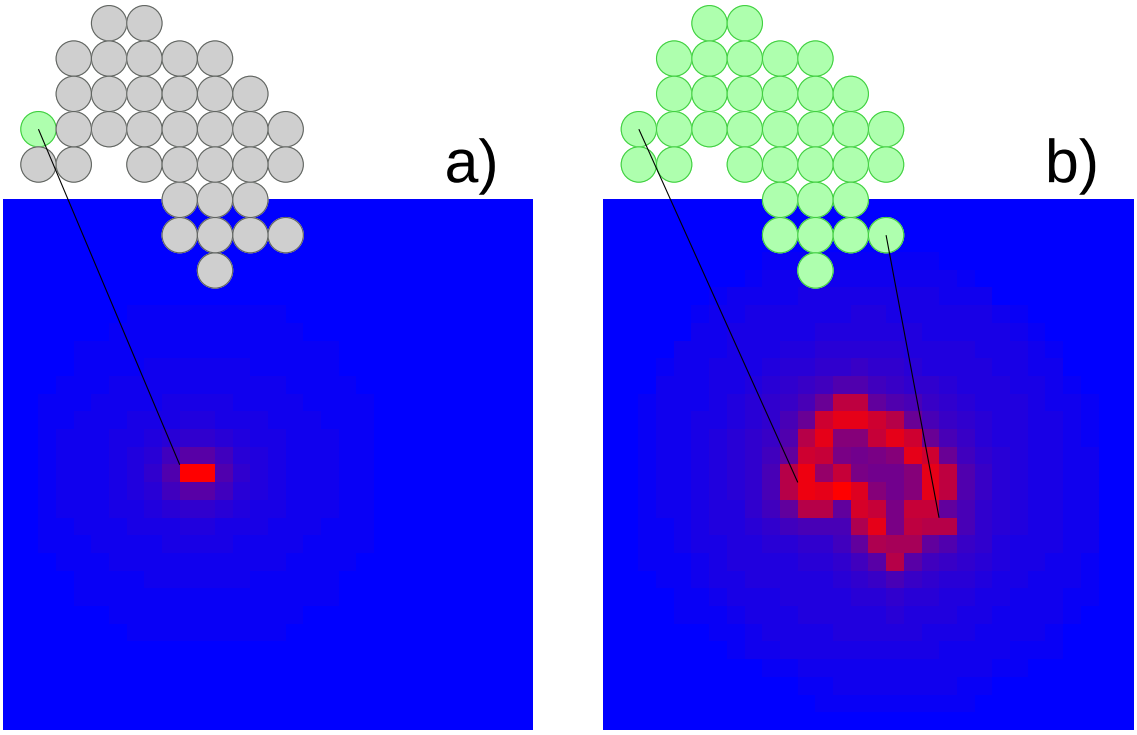


Fig. II.9: Strain fields generated by an island (grey and green circles) by superposition. in a) a single atom (green) generates a strain energy field shown in the plot below the sketch of the island. In b) the same situation is presented, if all the atoms contribute to the strain field.

of Poisson's ratio $\nu$ which is connected to the Lamé coefficients via

$$\nu = \frac{\lambda}{2(\lambda+\mu)} \tag{II.4}$$

in addition to the shear modulus $G = \mu$. Alternatively, one may use the compression modulus

$$\kappa = \lambda + \frac{2}{3}\mu \tag{II.5}$$

and $\mu$, or the elastic modulus

$$E = \frac{9\kappa\mu}{3\kappa+\mu} \tag{II.6}$$

and $\nu$ [Lan70].

The reverse relations are

$$\begin{aligned} \mu &= \frac{E}{2(1+\nu)} \\ \kappa &= \frac{E}{3(1-2\nu)}. \end{aligned} \tag{II.7}$$

The $z$-dependence in eqns.II.3 is only relevant, if the source of the strain is buried beneath the surface, as, for example, in quantum dot stacks. If $z$ is chosen equal to zero, one finds with $r = \sqrt{(x^2+y^2)}$:

$$\begin{aligned} \varepsilon_{xx} &= \frac{|\mathbf{F}|\,x}{\pi\,\mu\,r^5}\Big[-x^2(1+4\nu-6\nu^2)- \\ &\quad -y^2(1-\nu-3\nu^2)\Big] \\ \varepsilon_{yy} &= \frac{|\mathbf{F}|\,\nu\,x}{\pi\,\mu\,r^5}\Big[x^2(1+\nu)-y^2(5-4\nu)\Big] \\ \varepsilon_{zz} &= \frac{|\mathbf{F}|\,\nu\,x}{2\,\pi\,\mu\,r^5}\Big[2\,x^2(1-\nu)- \\ &\quad -y^2(1-11\nu+6\nu^2)\Big] \\ \varepsilon_{xy} &= \varepsilon_{yx} = \frac{|\mathbf{F}|\,x}{\pi\,\mu\,r^3}\left[\nu(1-\nu)\right] \\ \varepsilon_{xz} &= \varepsilon_{zx} = \varepsilon_{yz} = \varepsilon_{zy} = 0. \end{aligned} \tag{II.8}$$

Now, of course, the strain field has to be translated into an energy correction term to be used in the Monte Carlo simulation. The energy term in question is the Helmholtz free energy $F$, that is given in terms of the strain components as [Lan70]

$$\begin{aligned} F &= F_0 + \frac{\lambda}{2}\left(\sum_i \varepsilon_{ii}\right)^2 + \mu \sum_{ij} \varepsilon_{ij}^2 \qquad \text{(II.9)} \\ &= F_0 + \frac{\lambda}{2}(\varepsilon_{11}+\varepsilon_{22}+\varepsilon_{33})^2 + \\ &\quad \mu(2\varepsilon_{12}^2 + 2\varepsilon_{23}^2 + 2\varepsilon_{13}^2 + \varepsilon_{11}^2 + \varepsilon_{22}^2 + \varepsilon_{33}^2) \end{aligned}$$

This equation is valid for the isotropic case only. Unfortunately, most crystalline structures have a more or less pronounced anisotropic character and the elastic properties even for the simplest anisotropic case, the cubic crystal, are given by three material parameters $c_{11}$, $c_{12}$ and $c_{44}$ instead of the two Lamé coefficients.

As a measure of anisotropy the quantity

$$A := \frac{2c_{44}}{c_{11}-c_{12}} \qquad \text{(II.10)}$$

can be used; for almost isotropic, cubic crystals like tungsten its value is close to one. In this case the use of isotropic equations seems to be justified and average Lamé coefficients can be defined via [Hir82, Pim98]

$$\lambda = \frac{1}{5}(2c_{11}+3c_{12}-4c_{44}) \qquad \text{(II.11)}$$

$$\mu = \frac{1}{10}(8c_{44}+c_{11}-c_{12}) \qquad \text{(II.12)}$$

In the isotropic case with $A = 1$ or $c_{11} = c_{12} + 2c_{44}$ this reduces to

$$\begin{aligned} c_{11} &= \lambda + 2\mu \\ c_{12} &= \lambda \qquad \text{(II.13)} \\ c_{44} &= \mu. \end{aligned}$$

It might be instructive to have a look at the decay characteristics of the strain energy with increasing distance to the source of strain. Looking at a small island, one can assume that, for a large distance away, the island should appear as a point defect. Continuum theory of elastic media now claims [Pim98] that the elastic interaction energy of a point defect with another adatom vanishes like $r^{-3}$ with increasing $r$. For an infinitely long row of point defects the elastic interaction energy is obtained by integration over all point defects along the row and gives a dependence like $r^{-2}$ on the distance $r$.

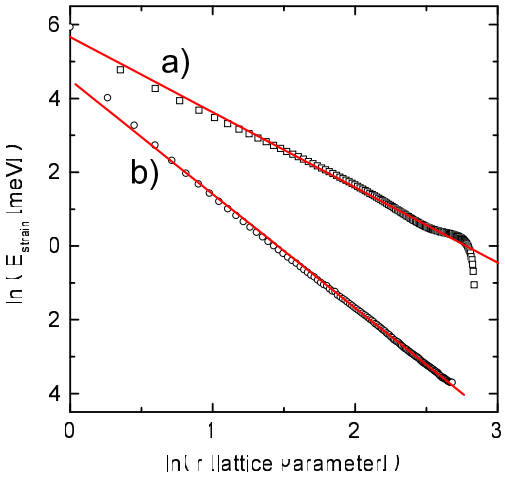


Fig. II.10: Decay of strain energy with increasing distance from the source of strain in a double-logarithmic plot for a) an infinite step edge and b) a point source. Results from the numerical routine are plotted as open circles. A linar fit ($y = y_0 + ax$) is shown as a red line. Parameters for the fit are a) $y_0 = 5.7$ and $a = -2.08$ and b) $y_0 = 4.4$ and $a = -2.96$. ($E_{\text{strain}} \sim r^{-a}$)

To check the consistency of the implementation of eqns.II.3 into the Monte Carlo program, the interaction energies of a point defect and a row of sources of strain with an adatom have been computed. The result is shown in Fig.II.10. The expected exponents of $-3$ and $-2$ for the single strain source and a row of defects, respectively, are well recovered by the numerical routine. The linear fit to the data points gives a slope of $-2.08$ for

the row and $-2.96$ for the point defect. The deviations for large distances are a numerical artefact and caused by the finite extension of the strain field.

#### *II.1.6.b Anisotropic elastic strain*

If the elastic anisotropy of the adsorbed material is considerable as, for example, in lead ($A = 3.9$) or if minor anisotropic effects seem important, one has to use an approach that allows for anisotropic contributions, explicitly. This can be done by a Green's functions approach for the cubic crystal [Por77, Shc95b]. A detailed derivation is given in Appendix B and as a result one finds expressions B.24, B.19 for

$$\begin{aligned} \varepsilon_{xx} &= \frac{\partial u_x}{\partial x} \\ \varepsilon_{yy} &= \frac{\partial u_y}{\partial y} \\ \varepsilon_{zz} &= \frac{\partial u_z}{\partial z} \\ \varepsilon_{xy} &= \frac{1}{2}\left(\frac{\partial u_x}{\partial y} + \frac{\partial u_y}{\partial x}\right) \\ \varepsilon_{xz} &= \varepsilon_{yz} = 0. \end{aligned} \tag{II.14}$$

with $u_i$ the spatially dependent displacement field from the unstrained case. For detailed information of how to calculate the anisotropic displacement field in the context of a Green's formalism, the reader is again referred to Appendix B.

The equivalence of the isotropic equations and the anisotropic extension is easy to show and given in Appendix C.

The Helmholtz free energy for anisotropic strain is given by

$$\begin{aligned} F &= F_0 + \frac{1}{2}c_{11}\sum_i \varepsilon_{ii}^2 + \\ &\quad + c_{12}\sum_{i\neq j}\varepsilon_{ii}\varepsilon_{jj} + 2c_{44}\sum_{i\neq j}\varepsilon_{ij}^2 \end{aligned} \tag{II.15}$$

which reduces to II.9 in the isotropic case $c_{11} = c_{12} + 2c_{44}$ ($\lambda = c_{12}$, $\mu = c_{44}$).

## II.2 Monte Carlo simulations

In this section a short introduction to the topic of Monte Carlo algorithms is given [New99]. The whole concept of the simulation of self-organized growth on surfaces, as it is presented in this work, crucially depends on the numerical Monte Carlo algorithm. Therefore, it seems a good assistance towards understanding the structure of the simulator to have a well defined idea of what Monte Carlo techniques can achieve (and what not).

### II.2.1 Equilibrium Monte Carlo

Statistical sampling methods have been used for a long time dating back to the beginning of the 18th century. The determination of the constant $\pi$ and later on the evaluation of integrals was a common application in those times.

The term 'Monte Carlo' was coined by Nicolas Metropolis in 1949 [Met49] and with the invention of the computer Monte Carlo methods have found a wide field of applications mainly within statistical physics.

#### *II.2.1.a General Methods*

Consider a system with a discrete set of states that exhibits some sort of dynamics. For such a system being in state $\mu$ one can define $R(\mu \to \nu)\, dt$ to be the probability to find the system in state $\nu$ after the time $dt$. Here $R(\mu \to \nu)$ is the transition rate from $\mu$ to $\nu$ and assumed to be time independent.

To characterize the system completely one has to define a set of weights $w_\mu(t)$ which represents the probability that the system will be in state $\mu$ at the time $t$. Then one can write

a master equation to describe the dynamics of the system:

$$\frac{dw_\mu}{dt} = \sum_\nu [w_\nu(t) R(\nu \to \mu) - w_\mu(t) R(\mu \to \nu)] \quad \text{(II.16)}$$

Following statistical mechanics, the expectation value of a quantity $Q$, which takes the value $Q_\mu$ in state $\mu$, is at the time t:

$$\langle Q \rangle = \sum_\mu Q_\mu w_\mu(t) \quad \text{(II.17)}$$

For equilibrium systems the values of the weights $w_\mu(t)$ are known as the equilibrium occupation probabilities $p_\mu$ which follow a Boltzmann distribution:

$$p_\mu = \lim_{t\to\infty} w_\mu(t) = \frac{1}{Z}\exp(-\beta E_\mu) \quad \text{(II.18)}$$

with $Z$ the partition function, $\beta$ the inverse product of temperature and Boltzmann constant $k$, and $E_\mu$ the energy of state $\mu$.

The expectation value of $Q$ is then

$$\langle Q \rangle = \frac{1}{Z}\sum_\mu Q_\mu \exp(-\beta E_\mu) \quad \text{(II.19)}$$

The ideal way of calculating the value $\langle Q \rangle$ would now be to average over all possible states $\mu$ weighted with their own Boltzmann probability. This of course is only possible for the very smallest of systems. Monte Carlo techniques work by choosing a subset of states at random from some probability distribution $p_\mu$ to be specified. If one chooses $M$ states $\mu_1, \ldots, \mu_M$ the best estimate of the quantity Q is:

$$Q_M = \frac{\sum_{i=1}^M Q_{\mu_i} {p_{\mu_i}}^{-1} \exp(-\beta E_{\mu_i})}{\sum_{j=1}^M {p_{\mu_j}}^{-1} \exp(-\beta E_{\mu_j})} \quad \text{(II.20)}$$

$Q_M$ is called the estimator of $Q$. Choosing the M states used for the calculation of the estimator $Q_M$ at random would in general be a rather bad choice. Most of the states would have tiny Boltzmann factors and the sums above would be dominated by only a few states making $Q_M$ a very inaccurate estimate.

If one has some information about the states which make relevant contributions to the sum one could pick the $M$ sample states just from those states and have a very good estimate of $Q$ from a relatively small number of terms.

This is indeed a key idea behind Monte Carlo simulations and the technique of choosing the appropriate states is called importance sampling.

The strategy with importance sampling is this: Instead of picking the $M$ sample states in such a way that every system state is equally probable to be chosen the states will be picked according to their Boltzmann probability $p_\mu$. Then the estimator $Q_M$ is

$$Q_M = \frac{1}{M}\sum_{i=1}^M Q_{\mu_i} \quad \text{(II.21)}$$

The only remaining question is how exactly to pick the states in order to ensure that each state appears with its correct Boltzmann probability. The standard solution in Monte Carlo simulations makes use of a Markov process (which is closely connected to the choice of the random number generator).

#### *II.2.1.b Markov-Process*

Instead of choosing states at random (which would be rejected almost all the time, since their probability is exponentially small) most Monte Carlo routines rely on a Markov process.

From a given state $\mu$ the Markov process generates a new state $\nu$ at random. The probability it generates a certain state $\nu$ out of $\mu$ is called the transition probability $P(\mu \to \nu)$ and is time independent. Note that the probability

for not changing the system ($P(\mu \to \mu)$) need not be zero.

However, a certain constraint on the Markov process has to be made considering that the process must generate *some* state $\nu$ when handed an initial state $\mu$. So the transition probabilities have to satisfy

$$\sum_{\nu} P(\mu \to \nu) \quad = \quad 1 \qquad \text{(II.22)}$$

In the Monte Carlo routine the Markov process is now repeatedly called to create a (Markov-)chain of states. With the proper choice of the Markov process the states in the chain appear with a probability given by the Boltzmann distribution, as is expected in equilibrium. To achieve this equilibration, two more constraints have to be made on the Markov process.

**Ergodicity** It is required that any possible system state can be reached by the Markov process.

**Detailed balance** This condition ensures, that we end up with the Boltzmann distribution of states rather than any other distribution. Here the crucial condition is, that the rate of all transitions into and out of any state $\mu$ must be equal

$$\begin{aligned} \sum_{\nu} p_\mu P(\mu \to \nu) &= \sum_{\nu} p_\nu P(\nu \to \mu) \\ p_\mu &= \sum_{\nu} p_\nu P(\nu \to \mu). \end{aligned} \qquad \text{(II.23)}$$

However, this balance of transition rates does not guarantee thermodynamic equilibrium, since a dynamic equilibrium, characterized by the emergence of limit cycles, might be found. To avoid this, the condition of detailed balance is imposed

$$p_\mu P(\mu \to \nu) \quad = \quad p_\nu P(\nu \to \mu) \qquad \text{(II.24)}$$

Now it is ensured that we end up with a distribution of states $\mu$ characterized by the probabilities $p_\mu$. For a Boltzmann distribution a proper choice would be one that satisfies

$$\begin{aligned} \frac{P(\mu \to \nu)}{P(\nu \to \mu)} &= \frac{p_\nu}{p_\mu} \\ &= \exp(-\beta(E_\nu - E_\mu)) \end{aligned} \qquad \text{(II.25)}$$

There are many ways in which to satisfy the above condition. One possible choice is

$$P(\mu \to \nu) \quad \sim \quad \exp(\frac{1}{2}\beta(E_\mu - E_\nu)) \qquad \text{(II.26)}$$

another one is discussed in the next chapter on the Metropolis algorithm.

### *II.2.1.c Acceptance ratio*

The construction of a Monte Carlo algorithm now looks very straightforward. Given a set of transition probabilities $P(\mu \to \nu)$ a Markov process is started that produces states with just their right Boltzmann distribution. Unfortunately in most cases it is far from obvious, how the ideal Markov process has to look like. There are, of course, many ways of generating new states $\nu$ from an old one but most of them will not satifiy eq.II.22 or have the right transition probabilities.

Luckily it turns out that it is not necessary to have the Markov process generate exactly the 'right' states. In fact it may produce states with arbitrary probability if one introduces an acceptance ratio.

As was mentioned above, it is allowed to choose the transition probability $P(\mu \to \mu)$ non zero. As far as the sum rule eq.II.22 is concerned, this allows for changes in $P(\mu \to \nu)$ simply by compensating with an opposite adjustment of $P(\mu \to \mu)$. Detailed balance

is preserved if $P(\nu \to \mu)$ is simultaneously changed.

This leads to the following, more mathematical consideration. We break down the transition probability into two parts

$$P(\mu \to \nu) \quad = \quad g(\mu \to \nu) \cdot A(\mu \to \nu) \tag{II.27}$$

The quantity $g(\mu \to \nu)$ is called the selection probability for the transition from $\mu$ to $\nu$ and is defined by the Markov process. $A(\mu \to \nu)$ is the acceptance ratio which tells us that a fraction of time $A(\mu \to \nu)$ we should indeed change the system from $\mu$ to $\nu$. The rest of the time we should just stay where we are and not change the system at all.

Since the critical constraint eq.II.24 only fixes the ratio

$$\frac{P(\mu \to \nu)}{P(\nu \to \mu)} \quad = \quad \frac{g(\mu \to \nu) \cdot A(\mu \to \nu)}{g(\nu \to \mu) \cdot A(\nu \to \mu)} \tag{II.28}$$

and the rate $A(\mu \to \nu)/A(\nu \to \mu)$ can take any positive value, we are completely free to choose $g(\mu \to \nu)$ and $g(\nu \to \mu)$; i.e. we can choose any Markov process we like.

For a decent Monte Carlo routine it is of course desirable to have the acceptance ratios as close to unity as possible. This means a clever programmer would like to put as much information about the equilibrium distribution of states as possible into the design of the state selecting Markov process to keep the acceptance ratios large.

For a perfect Markov process which creates states with their Boltzmann probability the acceptance ratios are always one.

*Continuous Time Monte Carlo* This algorithm is also called 'event based Monte Carlo' or the 'BKL algorithm' after Bortz, Kalos and Lebowitz (1975) who invented it [Bor75]. This algorithm is extremly helpful in simulating low-temperature systems.

Such a low-temperature system in equilibrium will spend a lot of time in the ground state. For each time step a common algorithm, as discussed above, chooses a new state which is then rejected since the acceptance ratio is very low. This consumes a lot of computer time doing nothing.

The basic idea behind continuous time Monte Carlo is now the following: By looking at the acceptance ratios the system is likely to spend a certain (and long) time in the ground state. Continuous time Monte Carlo now assumes that this is indeed the case, skips the time interval where nothing is happening and moves on directly to the time step where the system makes a transition.

To quantify this idea one has to evaluate the time $\Delta t$ in which the system does not leave the ground state. The probability that the system is still in the same state $\mu$ after $t$ time steps is just:

$$[P(\mu \to \mu)]^t \quad = \quad \exp(t \log(P(\mu \to \mu)) \tag{II.29}$$

The time scale $\Delta t$ is then

$$\begin{aligned} \Delta t &= -\frac{1}{\log P(\mu \to \mu)} \\ &= -\frac{1}{\log[1 - \sum_{\nu \neq \mu} P(\mu \to \nu)]} \\ &\simeq \frac{1}{\sum_{\nu \neq \mu} P(\mu \to \nu)} \end{aligned} \tag{II.30}$$

The actual algorithm now consists of three parts:

1. Calculate the probabilities $P(\mu \to \nu)$ for transitions to all states $\nu$ that can be reached from the current state $\mu$. Change the system to a state $\nu$ where the new state is chosen with a probability proportional to $P(\mu \to \nu)$.

2. By using the values for $P(\mu \to \nu)$ calculate the time $\Delta t$. Note that in general the time $\Delta t$ changes from one step to the next.

3. Increment the time $t$ by $\Delta t$ to mimic the effect of waiting $\Delta t$ time steps.

### *II.2.1.d Metropolis Algorithm*

The Metropolis algorithm was introduced by Nicolas Metropolis and co-workers in 1953 [Met53].

Let us consider a system in state $\mu$. From this state our Markov process has access to $N$ new states. The Metropolis algorithm now assigns the same selection probability to all of the $N$ states.

$$g(\mu \to \nu) = \frac{1}{N} \tag{II.31}$$

The condition of detailed balance then reads

$$\begin{aligned} \frac{P(\mu \to \nu)}{P(\nu \to \mu)} &= \frac{g(\mu \to \nu)}{g(\nu \to \mu)} \cdot \frac{A(\mu \to \nu)}{A(\nu \to \mu)} \\ &= \frac{A(\mu \to \nu)}{A(\nu \to \mu)} \\ &= \exp(-\beta(E_\nu - E_\mu)) \end{aligned} \tag{II.32}$$

One possible choice for the acceptance ratios would be

$$A(\mu \to \nu) = A_0 \cdot \exp(-\frac{1}{2}\beta(E_\nu - E_\mu)) \tag{II.33}$$

The constant $A_0$ may take any value except those which make $A(\mu \to \nu)$ greater than 1. On the other hand we wish the acceptance ratios to be as large as possible, so we choose $A_0 = \exp(-\beta E_{max})$ with $E_{max}$ being the largest energy difference possible for that particular system. We then have

$$\begin{aligned} A(\mu &\to \nu) \\ &= A_0 \cdot \exp(-\frac{1}{2}\beta(E_\nu - E_\mu + E_{max})) \end{aligned} \tag{II.34}$$

This acceptance ratio gives the right Boltzmann distribution of states but the acceptance ratios are pretty small for most values of $\Delta E = E_\nu - E_\mu$ (Fig.II.11).

Since eq.II.24 only fixes the ratio of $A(\mu \to \nu)$ and $A(\nu \to \mu)$ we are allowed to make the larger one equal to unity and have the other one satisfy eq.II.24. Then we get

$$\begin{aligned} A(\mu &\to \nu) \\ &= \begin{cases} \exp(-\beta(E_\nu - E_\mu)) & : \quad (E_\nu > E_\mu) \\ 1 & : \quad \text{otherwise} \end{cases} \end{aligned} \tag{II.35}$$

This is the Metropolis algorithm and it means that we accept every system change towards lower energies. Changes to higher energies are rejected depending on the energy difference (Fig.II.11).

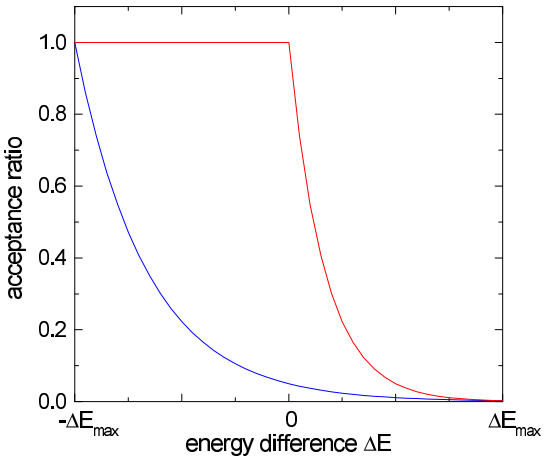


Fig. II.11: Plot of acceptance ratios for a simple Monte Carlo algorithm (solid) and the Metropolis algorithm (dashed) vs. energy difference $\Delta E$.

### *II.2.1.e Wolff Algorithm*

Simple and hence most widely used algorithms do not make complex changes to the system from one Monte Carlo step to the next. Instead they alter the system in the smallest possible steps — for example in the case of the Ising model[4] by changing the spin orientation at only one lattice site.

4. The Ising model is a simple model of a magnet and deals with interacting magnetic dipoles that are arranged along a regular lattice. At each lattice site the spin orientation may be $+1$ or $-1$.

Close to a critical temperature, however, this so called 'single spin flip' dynamics becomes very cumbersome, since typical fluctuations of the magnetization are no longer caused by turns of single spins but rather large domains changing their spin orientation.

The Wolff algorithm is similar to a Metropolis algorithm and is tailored to deal with systems where a single spin flip dynamics is not suitable [Wol89].

The basic idea of the Wolff algorithm is to connect equally aligned spins to clusters with a certain connection probability (to preserve detailed balance) and then instead of flipping single spins to change the system by flipping a whole cluster.

This type of algorithm is referred to as a 'cluster flipping' or 'cluster' algorithm.

#### *II.2.1.f Swendsen-Wang and Niedermayer's algorithm*

Two more cluster flipping algorithms are commonly used. The Swendsen-Wang algorithm [Swe87] works very much like the Wolff algorithm by dividing the lattice into clusters. But instead of flipping only one cluster all the clusters are flipped with probability $1/2$. The proof that detailed balance is preserved is, however, difficult. This algorithm works best very close to the critical temperature.

The Niedermayer's algorithm [Nie88] is a Wolff algorithm where not only equally aligned spins can form a cluster but also antiparallel spins may be connected to form a domain. The connection probability for parallel and antiparallel spins is assumed to be different. This approach is a very general one and makes this algorithm applicable to a vast range of models.

### II.2.2 Monte Carlo in Surface Science

The Ising model has another application in quite a different field of physics; in surface science. Here the Monte Carlo scheme simulates the diffusion of adatoms on a crystalline surface.

#### *II.2.2.a Dynamics of a single adatom*

The hopping rate $r_{ij}$ from lattice site $i$ to $j$ is related to the separating energy barrier $B_{ij}$ by the Arrhenius law

$$r_{ij} = \nu \exp(-\beta B_{ij}) \tag{II.36}$$

$\nu$ is the attempt frequency and sets the overall time scale for adatom movement. Since $\nu$ does not enter the exponential it is a reasonable assumption to take $\nu$ as a constant, i. e. independent of temperature. Successive hops are assumed to be uncorrelated.

A simple Monte Carlo routine to move the atom around would be to choose one direction to move in and then make the move with an acceptance ratio

$$A = \exp(-\beta(B_{ij} - B_{min})) \tag{II.37}$$

$B_{min}$ is the lowest energy barrier in the system and ensures that the largest acceptance ratio becomes equal to one. Every Monte Carlo step then corresponds to a real time interval of

$$\Delta t = \frac{\exp(\beta B_{min})}{4\nu} \tag{II.38}$$

The $4$ comes from the four possible directions in which the atom can move on a square lattice.

For a continuous time Monte Carlo scheme we have to sum the hopping rates over all accessible sites $j$ and find

$$\Delta t = \frac{1}{\sum_j r_{ij}} \tag{II.39}$$

*II.2.2.b Many adatoms*

If there are many adatoms on the surface one has to exclude hops to lattice sites already occupied by other atoms. Another difference to single adatom motion is the influence of the other adatoms on the energy barriers by the formation of bonds and strain fields.

Most Monte Carlo simulations for adatom diffusion fall into one of the following three classes

*Kawasaki-type energy barriers* The energy barriers are called Kawasaki-type because with their particular form they lead to a code that is structurally the same as for the Kawasaki algorithm [Kaw66]. This algorithm is used to simulate 'conserved order parameter' systems. If, for example, in the Ising model magnetization has to be kept constant, neither single spin flip dynamics nor simple cluster algorithms can be used since they alter magnetization.

The Kawasaki algorithm solves this problem by choosing two spins of opposite direction and exchanges their value. It does this with Metropolis-like acceptance ratios.

Structurally the conservation of magnetization in the Ising model is the same as the conservation of adatoms on the surface. If an atom leaves a lattice site to diffuse, it has to show up again somewhere.

The Kawasaki-type barrier $B_{ij}$ for hopping from $i$ to $j$ is given as (Fig.II.12):

$$B_{ij} = \begin{cases} B_{min} + E_j - E_i & : \quad (E_j < E_i) \\ B_{min} & : \quad \text{otherwise} \end{cases} \tag{II.40}$$

where $B_{min}$ is the lowest energy barrier in the system. For this type of Monte Carlo routines one step corresponds to an interval of real time of

$$\Delta t = \frac{\exp(-\beta E_{min})}{4n\nu} \tag{II.41}$$

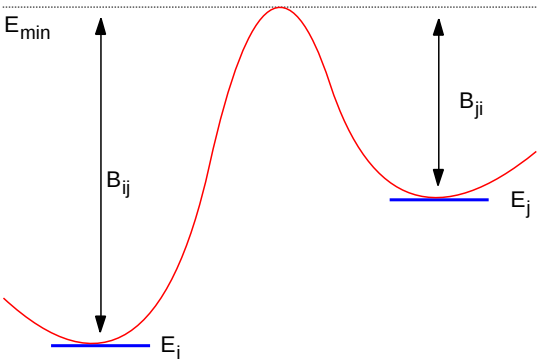


Fig. II.12: Binding energies $B_{ij/ji}$ at the adsorption sites $i$ and $j$ resp. The lowest binding energy is $E_{min}$.

with $n$ being the number of adatoms on the surface.

*Bond counting method* Here we add to the constant energy $B_{min}$ the binding energy $E_b$ to the $n$ neighbors present at lattice site $i$. Then we get for a hop from site $i$ to $j$:

$$B_{ij} = B_{min} + n_i \cdot E_b \tag{II.42}$$

For this type of routines one might include nearest and next nearest neighbors or nearest neighbors only.

*Lookup Tables* The energy barriers for moves in different directions in general depend very sensitively on the spatial configuration of the surface (neighboring atoms, surface reconstruction, etc.). If we can calculate the energy barriers for hops in different directions for all the relevant configurations[5] by certain atomic

5. For a full lookup table treatment there are ten nearest and next nearest neighbor sites on a square lattice to be considered. This amounts to $2^{10} = 1024$ different configurations!

structure methods, we can store these energies in a table to be used in a Monte Carlo simulation. For every Monte Carlo step the surrounding of the initial and final site is determined and an acceptance ratio is assigned to the move in accordance to the energy value stored in the lookup table.

## II.3 The Monte Carlo routine

By now, all the important physical concepts and numerical techniques have been introduced and the program code used for the simulations presented in this work can be discussed. First, the physics included in the program will be reviewed, the numerical details make up the second part.

### II.3.1 Physical concepts

The code is capable of simulating the deposition and diffusion of adatoms on a surface using single adatom diffusion processes[6].

The desorption of adatoms is not included neither is bulk diffusion. Consequently, as far as the kinetics is concerned, its routine is best suited to simulate MBE growth, where desorption is of little importance and the sticking coefficient $Q$ is close to unity, as in $Si$ and some metals [Zan88].

As is obvious from eq.II.2 the hopping probability $p$ depends exponentially on the energetic diffusion barriers $E_x$. For this reason the modelling of surface kinetics reduces to modelling suitable energy terms associated with the various surface processes.

The most important energy contribution in terms of the absolute value is the binding energy to the surface $E_s$. It is chosen to be $1.3$eV, which is close to values used in other Monte Carlo simulations [Cla91]. The surface binding has to be considered in every diffusion process and is related to the overall time scale. The covered time interval $\Delta t$ by a process of probability $p$ is related to the energy barrier $E_s$ as

$$\Delta t \;\sim\; \frac{1}{p} \;\sim\; \exp\left(\frac{E_s}{kT}\right) \qquad \text{(II.43)}$$

Since the surface binding energy $E_s$ is a common factor to all diffusion processes, one can define a new time scale $\Delta t'$ by changing $E_s$ by $\Delta E_s$. One finds:

$$\begin{aligned}\Delta t' &\sim \exp\left(\frac{E_s + \Delta E_s}{kT}\right) \\ &\sim \Delta t \cdot \exp\left(\frac{\Delta E_s}{kT}\right)\end{aligned} \qquad \text{(II.44)}$$

The next important energy contribution is the binding energy to the nearest and next nearest neighbors. The strength of a single nearest neighbor bond is set to $0.3$eV, and reduced by a factor of $nn = \sqrt{2}$ for next nearest neighbors. To evaluate the diffusion barrier due to the nearest neighbor interactions, the binding energy at the site $S0$, where the diffusing atom is located, is calculated to be $E_{S0} = n\,E_n + nn\,m\,E_n$ in dependence of the number of the $n$ nearest and $m$ next nearest neighbors. The same is done for the locus $S1$ where the adatom is going to diffuse to. It is $E_{S1} = c(n'\,E_n + nn\,m'\,E_n)$, where $c$ is a constant that describes the coupling between adjacent lattice sites. It is chosen to be equal to $0.2$, which corresponds to a weak coupling. The overall binding energy $E_N$ caused by neighbor interactions for a given diffusion process from site $S0$ to $S1$ is given by the difference of the binding energy at the corresponding lattice sites

$$E_N \;=\; (n - c\,n')E_n + (m - c\,m')\,nn\,E_n \qquad \text{(II.45)}$$

6. This corresponds to a single spin flip dynamics, but strictly speaking we use some sort of continuous Kawasaki algorithm since every diffusing atom disappears at one site and at the same time appears somewhere else, usually close by

For diffusion processes away from island boundaries the diffusion barrier is just $E_{S0}$. However, for diffusion along step edges or around corners the hopping probability is slightly enhanced. In the simulation this effect results in smoother island boundaries, since vacancies and gaps are efficiently filled by atoms diffusing along the perimeter of the islands.

For diffusion processes across step edges a Schwöbel energy barrier has been defined to be $E_{SW} = 0.1$eV. For atoms being deposited, the Schwöbel barrier can be surmounted by the kick-out effect with a probability proportional to the number of free nearest neighbor sites.

To account for diffusional anisotropy effects caused by a certain surface reconstruction, an extra energy term $E_{AD}$ can be assigned to a particular direction. Since the underlying lattice is of a square symmetry, diffusional anisotropy can only be included for energy differences in the two main directions of the surface.

The last important energy contribution is made up by the elastic strain energy. This energy $E_{STR}$ is calculated via the anisotropic approach (eqns.II.14) for simulations on a plain surface. In simulations of the growth of quantum dot stacks, where buried dot structures influence the strain at the surface and, additionally, the third dimension has to be considered in calculating strain fields, the isotropic formulas (eqns.II.3) are used.

It has to be mentioned that a certain difficulty in the strain calculation made it necessary to introduce two different methods of calculating the line forces, that compress or dilate the islands. Both methods have their pros and cons and their applicability depends strongly on the simulation parameters.

To change the lattice constant of a pair of atoms, the necessary force $F_0$ is assumed to be such that the binding energy between the two atoms is reduced by 10meV[7]. In a chain of $n$ atoms the force $F$ necessary to compress or extend the chain by the same amount for each pair of atoms is given by Hooke's law and consequently equal to

$$F = n F_0. \tag{II.46}$$

By applying this wisdom to the calculation of strain for an island, one is lead to solution A in Fig.II.13. Here, depending on the orientation of the boundary, the number of atoms in a horizontal or vertical direction is counted to yield the number $n$. This method has the main advantage of being completely independent of the island morphology and works well for compact islands (Fig.II.13a) as well as for fractal-like structures. This local approach has, however, an important drawback that becomes even more apparent for high temperatures or long equilibration times. The equilibrium crystal shape induced by method A is indeed not compact, as one would expect for isotropic strain. It rather favors the emergence of diagonal rows (FigII.13c), since here the thickness in the main directions is small and, consequently, the strain along the boundary as well. As a result, the strain does not inhibit the further growth of diagonal rows and thus looses its size limiting property. Of course, this effect is unphysical and can be overcome by method B.

This second method does not evaluate the extension of an island by counting atoms in a certain direction but rather by determining the distance of the boundary from the center of mass of the island (Fig.II.13b). This distance is multiplied by two to give the factor $n$ in eq.II.46. For highly symmetric, compact islands, method A and B give just the same results. But, as one can see in Fig.II.13d, the generation of diagonal structures is now suppressed, since parts of the island boundary far

7. It is very difficult to obtain absolute values for acting forces or strain fields from experiments. Though, some sparse results can be found [Pen01]

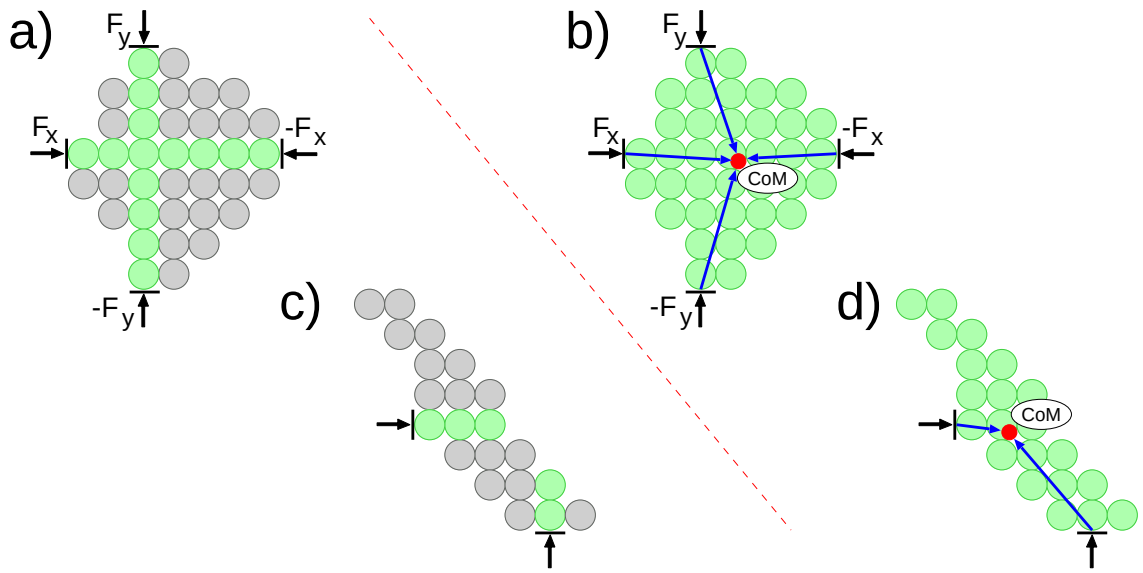


Fig. II.13: Two methods to calculate the line forces along island boundaries for strain field calculations. Method A determines the island thickness perpendicular to the boundary, method B measures the distance boundary to center of mass (CoM). a) and b) compare the two methods for compact islands and c) and d) for elongated islands.

away from the center of mass experience a stronger force than those close to it. Now, the equilibrium shape using method B is a compact island.

This would render method B the method of choice, if there were not an unphysical effect, that appears if two islands coalesce. If two islands are connected by only a single 'bridge'-atom, the strain field of the now joined islands would not be very different from the two separate islands. This is no longer true for calculating the strain via method B. Indeed, the center of mass changes position considerably if the islands merge and so does the strain field. Soon a new, compact island has formed around the new center of mass. This is an effect similar to the merging of two water droplets to one large droplet due to surface tension.

Since the effect of coalescence becomes important for high island densities, method B is unsuited for the simulation of cold systems or high coverages. However, for the sake of consistency, all simulations presented in this work have been obtained using method B, unless remarked otherwise.

Now, the physics of surface diffusion processes of adatoms can be summed up by the probability $p$ for a hop from one lattice site to a nearest or next nearest neighbor site as

$$p = \nu_0 \exp\left(\frac{-(E_S + E_N + E_{AD} - E_{STR})}{kT}\right) \tag{II.47}$$

The attempt frequency $\nu_0$ is assumed to be temperature independent and equal to $\nu_0 = 10^{13}$Hz. Similar to the surface binding energy $E_S$, $\nu_0$ influences the overall time scale. Eq.II.47 now gives the basis for the Monte Carlo simulation routine described in the next section.

### II.3.2 Numerical concepts

The simulation routine is based on a continuous time Monte Carlo scheme. A BKL

algorithm is very efficient for the problem at hand, since the independence of a particular time scale is of great advantage in simulating surface diffusion [Pre92]. A surface atom without any neighbors might diffuse by a factor of $10^3$ more rapidly than atoms bound to a step edge.

Adatom diffusion processes are simulated one by one. The principal course of a simulated diffusion process is always the same and sketched in the following. An atom is chosen by a random process and moved across the surface by hops to nearest or next nearest lattice sites. The corresponding time interval $\Delta t$ is calculated and added to the elapsed simulation time. If atoms are still deposited, according to $\Delta t$ and the flux conditions new adatoms are placed at random positions on the surface. The main difficulty lies in the assignment of a proper weight to each possible diffusion process, so that every adatom hop is executed with a likelihood according to its overall probability with respect to all other processes.

This is done (see Fig.II.14a) by evaluating the probability $p$ from eq.II.47 for every possible diffusional step of a given adatom. These eight possible transition probabilities to nearest and next nearest neighbor positions are stored and then added up to give a total probability $p_{\mathrm{Atom}}$ for the adatom to move in any direction at all. This probability is translated into an effective energy barrier $E_{\mathrm{Atom}}$ for diffusion[8]. Since the energy barriers can take on continuous values due to the strain energy correction, it is necessary to introduce energy intervals, so that all adatoms with an effective diffusion barrier $E_{\mathrm{Atom}}$ between $E_0$ and $E_0 + \Delta E$ can be grouped together in a class of adatoms with the same likeliness to move.

The grouping and building of classes is, of course, not really necessary, since every diffusional process could be handled on its own account, it just helps enormously in bookkeeping. In a given class all the probabilities are again summed up to yield the total probability $p_{\mathrm{Class}}$, that an atom from this particular class makes a move. The total probability that anything might happen at all is then given by adding up the $n$ terms $p_{\mathrm{Class}}$ to give $p_{\mathrm{Total}}$.

Now the choice of a certain diffusion process works like the assignment of a diffusion process to a certain class, just in the opposite direction (Fig.II.14b). A class is chosen at random, considering that different classes contribute differently to the overall probability $p_{\mathrm{Total}}$. Each class contains a number of atoms of which one is chosen with equal probability. Then from the eight possible diffusion processes, one is selected in accordance to its likeliness and executed. Then the simulation time is propagated by an amount of time $\Delta t$ given by

$$\Delta t = \frac{1}{p_{\mathrm{Total}}} \qquad \text{(II.48)}$$

Usually the movement of an atom also alters the diffusion barriers for the neighboring atoms in the old neighborhood as well as in the new one. So the moving atom and all atoms in its surrounding have to be assigned new classes. Strictly speaking, also the strain energy field would have to be recalculated after every step. But, since the evaluation of the strain is a lengthy procedure and the strain only changes little with the motion of a single adatom, it has turned out that it is sufficient to recalculate the strain every couple of 1000 diffusional steps. Then, of course, all atoms on the surface have to be assigned new classes. To speed up the computations even further, the

8. It is not necessary to introduce a linear energy scale and it would be possible to use just the transition probabilities $p_{\mathrm{Atom}}$. It is, however, easier to have a quantity that can be broken down into intervals equidistantly like the energy. To achieve the same with the transition probabilities one would have to use a logarithmic interval scaling. This would amount to just the same as the linear energy scale but look much less neat in the program code

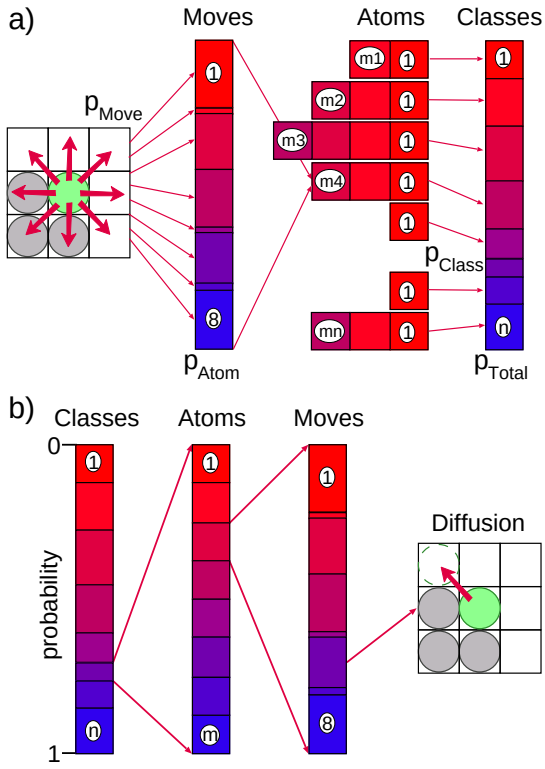


Fig. II.14: Sketch of algorithms to assign adatoms to Monte Carlo classes in dependence of their energetical situation a) and the selection process for certain diffusion processes by the simulation routine b).

strain field does not extend over the whole system but only over a circular area of a given radius $r$ around the source of the strain which is in most cases chosen to be of thirty lattice constants.

# III.

# Optimization of Growth Parameters

For most applications that include active quantum dot layers it is of key importance to have as many and as equally shaped dots as possible to obtain a well defined response to optical or electronical signals, while losses are small. To achieve high densities of dots, spatial ordering in the average distance between two neighboring dots as well as ordering along distinct directions is necessary [Muk98, Muk99].

To obtain spatial and size ordering, self-organized quantum dot growth can be used as will be shown in this chapter [Shc99a, Dar97, Ipa98]. Unfortunately, the problem of generating self-organized patterns can not be solved in a straight forward manner. Even though Stranski-Krastanov growth is known to be suitable for self-organized quantum dot growth, there are many external parameters that influence the growth result considerably. This is easy to see, if one considers the immense number and the complex interplay of parameters that control growth conditions in an actual growth reactor.

Growth control is still difficult to gain, if one restricts the set of relevant parameters to temperature $T$, flux $f$ and coverage $c$ by choosing a simple numerical model, as is done in this work. If, for example, the growth temperature is chosen too low, the deposited atoms will just stick to the surface without having enough thermal energy to diffuse. In this case, of course, no self-organization is to be expected. If, on the other hand, temperature is too high, interatomic bonds are too easily overcome and one observes an ensemble of monomers and small polymers of adatoms performing random walks over the surface. In this scenario larger islands are inherently unstable. Only for a distinct interval of temperatures self-organization is effective and accessible to production processes. Similar effects can also be seen with parameters like flux to the surface or the surface coverage.

Another important factor to influence the growth result is the time between the end of deposition and the capping of the quantum dot layer with another material, the so called growth interruption. During this growth interruption the adatoms can relax to energetically favorable positions and approach thermodynamic equilibrium. Since there is a striking difference between kinetically controlled growth and a thermodynamically dominated size distribution, as will be shown in Chap.IV, the effect of a growth interruption can be dramatic. Furthermore, the inital stages of growth of quantum dots are most important for ordering effects, since here the monolayer islands can respond more easily to energetical changes in their vicinity. The morphology and spatial arrangement of these ‘platelets’ will then determine the arrangement of the fully grown dots [Kun90, Pri95]. For this reason, a growth

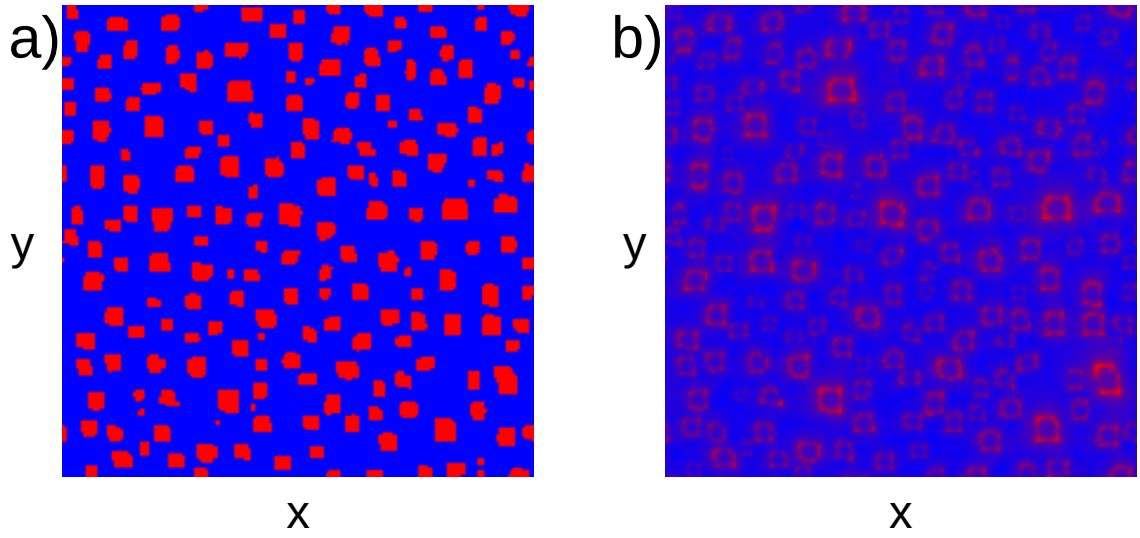


Fig. III.1: a) Spatial distribution of adatoms. Blue is the wetting layer surface and red the first growth layer. b) Plot of the strain energy generated by a). Red is high strain and blue the unstrained case. Simulation parameters are $T = 650$K, $f = 1.0$Ml/s and $c = 20\%$. Simulated time: 100.2s on a $200 \times 200$ grid.

interruption during the transition from two-dimensional to three-dimensional growth can improve the quality of the quantum dot layer considerably.

Now, the aim of this chapter will be to define optimal growth conditions with respect to size distributions and the spatial ordering of islands. Each of the above mentioned external parameters will be considered separately. Apart from assigning an optimal working range to each parameter, the effects of a poor choice of parameters will be adressed as well.

Firstly, however, a set of numerical tools will be introduced that are useful to quantify the quality of a given size distribution or the spatial ordering. With the help of these tools it will be possible to spot tiny changes in the resulting growth patterns caused by parameter variations, that would otherwise be lost to the unarmed eye.

It should be noted that for the experimentalist it is even more difficult to obtain information about island distributions. With the invention of the electron microscope and related techniques, however, the direct observation of nanoscale structures became possible and is intensively used for characterizing quantum dots ex situ.

The initial stages of $Ag/Ag(001)$ growth, for example, are investigated in [Zha97] by means of scanning tunneling microscopy (STM).

A powerful tool is, for example, the transmission electron microscope (TEM). It is reported in [Car98] that not only the shape of the quantum dots can be extracted but also the strain distributions of $InP/GaInP(001)$ quantum dots are accessible by TEM. Using the shape of the dots measured by TEM and appropriate elastic constants, good agreement is found with finite element calculations.

Experimental tomographic x-ray diffraction is done in [Keg00] to investigate nanometer-scale self-assembled $InAs/GaAs$ quantum dots. Shape, lattice constant distribution and

composition can be resolved by this advanced technique.

To monitor the growth process in situ a couple of techniques are available which allow to estimate the amount of deposited material by basically measuring the surface roughness.

A correlation between island-formation kinetics, surface roughening, and RHEED (reflection high energy electron diffraction) oscillation damping during GaAs homoepitaxy gives direct access to the deposited layer thickness [Hey97].

A similar technique can be used for in situ monitoring of 2D island growth by ion beam scattering [DeL99] or by grazing icidence x-ray scattering [Sch98c].

The Stranski-Krastanov formation of InAs quantum dots can be monitored during growth by reflectance anisotropy spectroscopy and spectroscopic ellipsometry giving information about layer thickness and composition[Ste97].

## III.1 Numerical tools

The basis for all evaluations is the spatial distribution of adatoms on the surface (Fig.III.1a). During the simulation of the growth process these distributions are saved and analyzed after a fixed number of time steps have passed. Together with the adatom distribution the strain energy field generated by the islands at the surface (Fig.III.1b) is kept, but rather for the sake of completenes since no further processing of the strain field is done.

The strain in all simulations is updated every $2500$ Monte Carlo steps. Throughout the simulations the isotropic, elastic constants are $\mu = 0.54 \cdot 10^{12}$erg/cm$^3$ and $\lambda = 0.32 \cdot 10^{12}$erg/cm$^3$, which can be obtained in isotropic approximation from the material parameters of $GaAs$ via II.11 and II.12. Other parameters are $E_s = 1.3$eV, $E_n = 0.3$eV for surface and nearest neighbor bonds, respectively. The binding energy to next nearest neighbors is reduced by a factor $nn = \sqrt{2}$ and edge diffusion is modelled by a coupling factor of $c = 0.2$. The Schwöbel barrier is chosen to be $E_{SW} = 0.1$eV.

All simulations in this chapter have been performed on a $200 \times 200$ grid with periodic boundary conditions. This system size has on one hand the advantage of being big enough not to prefer certain symmetries induced by self-interaction of islands or to produce undesired effects like noise caused by the small number of deposited adatoms[1]. On the other hand, computational effort is kept handy. The time for the pure Monte Carlo simulation increases about quadratically with the system extension due to the increasing number of possible moves. The time consumed by the statistical evaluations like the determination of island sizes and positions increases even faster than with a square law in the system size so that a run of the same simulation in a system with the double lateral extension takes longer by a factor of about six.

### III.1.1 Island size distribution

The first routine for data analysis and statistical evaluation of the growth results is the determination of the number of islands on the surface. Any cluster of a minimum number of four atoms is counted as an island. The temporal evolution of the number of islands in the simulation gives a first important information about the system itself (see Fig.III.2a). If, for example, the number of islands is growing or decreasing after the end of deposition, it is sure to assume, that the system is still evolving towards equilibrium.

More precise statements can be obtained from the second step of analysis. Here the size

1. If growth conditions induce an optimal island size of $500$ atoms in a system with $800$ deposited atoms, equilibrium can not be found

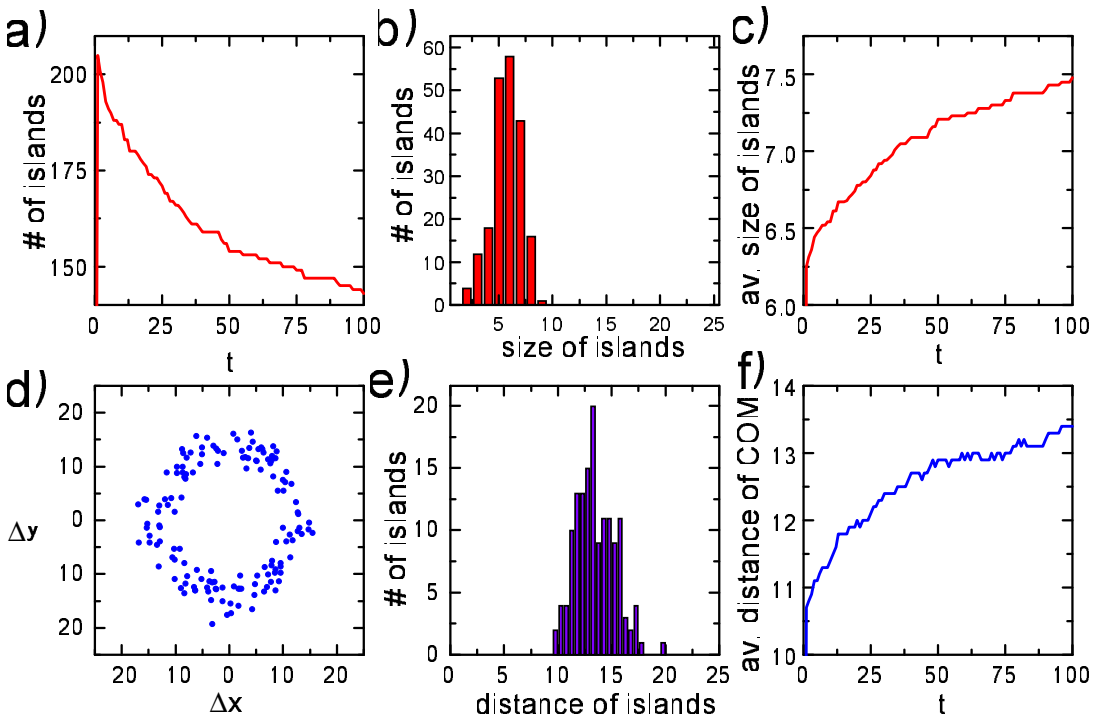


Fig. III.2: Analysis of the simulation presented in Fig.III.1. a) temporal evolution of the number of islands equal to or larger than four adatoms. b) The resulting size distribution after 100s and c) the temporal evolution of the average island size during the growth interruption of 100s. d) shows the spatial distribution of nearest neighbor distances. Measured is the distance of the centers of mass. e) is the distribution of absolute inter-island distances obtained from d). In f) the temporal evolution of the average distance of the centers of mass is given. Parameter: $T = 650$K, $f = 1.0$Ml/s and $c = 20\%$.

of each individual island is determined and stored in a histogram. The size is plotted as the square root of the number of island atoms, i.e. the mean diameter in atomic lattice units. In this histogram the total number of islands with the same diameter $d$ is stored in dependence of $d$, as in Fig.III.2b. Islands have the same integer diameter $d$, if they contain more than $d^2$ atoms but less than $(d+1)^2$ atoms. This histogram is also referred to as the size distribution of islands[2] From the size distribution an average island size can be computed as well as the standard deviation of the average size. One speakes of a narrow or sharp size distribution if the standard deviation of the average island size is small or, equivalently, if the width of the size distribution is small. The temporal evolution of the average island size is shown in Fig.III.2c.

### III.1.2 Spatial arrangement

To determine the quality of the spatial ordering of islands, first the centers of mass of all islands are computed. Then, for every island the nearest neighbor island is found by computing the distances between the corresponding centers of mass. The nearest neighbor positions are stored to give a nearest neigh-

2. Islands of size 1, wich are monomers to trimers, also enter the size distribution but are neglected in further statistical considerations.

bor distribution (Fig.III.2d). For an island distribution of perfectly equidistant islands all entries in the nearest neighbor distribution should fall onto a circle centered about the origin. If certain directions are preferred in the spatial ordering, this, as well, should show in the neighbor distribution by accumulation of points in the equivalent directions. If the distance between nearest neighbors is in a certain direction generally different from distances in other directions, i.e. the ring around the origin is distorted, this is a sign of diffusional anisotropy.

The way of evaluating the spatial ordering by means of a nearest neighbor distribution works very much like a two-dimensional Fourier transformation of the surface but has the advantage of being directly rather than inversely correlated to the surface morphology.

Very much like in the case of the size distributions, a histogram of island distances can be computed (Fig.III.2e). Here, all islands with a nearest neighbor distance between $r$ and $r+1$ fall into the same class of the histogram. Again, an average distance and a standard deviation can be assigned to the histogram of nearest neighbor distances. The temporal evolution of the average nearest neighbor distance is shown in Fig.III.2f.

## III.2 Temperature

To determine an optimal temperature for the growth of quantum dots, the parameters flux rate and coverage will be kept fixed at values $f = 0.1$Ml/s and $c = 30\%$, respectively. Then, deposition stops after 3s of simulated time. For this particular time one can evaluate the average island size in the system for various temperatures. The result of this analysis can be found in Fig.III.3a.

As is obvious from Fig.III.3a, there exists a distinct critical temperature $T_c$ beyond which the island size decreases rapidly. This effect is caused by the high thermal energy of the atoms. The process of island nucleation and growth is only possible, if the additional diffusion barriers caused by nearest neighbor bonds are high enough to keep the atoms at the island boundaries from dissociating. If the temperature is increased beyond the critical point of $T_c \sim 730$K, the atoms at the boundary of an island can easily detach and the whole island looses its stability. Later on, in Chap.IV a thermodynamical justification for this effect will be given but it can also be induced by an alloying effect between quantum dot and substrate [Ter98].

Below the critical temperature $T_c$ the average island size increases monotonically with $T$. For very low temperatures, diffusion processes have a low probability $p$ (given by eq.II.47) and hence adatoms have a small diffusion constant $D$

$$D = \frac{a^2}{2}p \qquad \text{(III.1)}$$

with $a$ the lattice constant. Furthermore, the additional energy barrier generated by nearest neighbor bonds is very unlikely to be crossed. Consequently, adatom polymers are stable and will not dissociate again for a long time. As a result each island will on average collect adatoms from a circular area of a radius of the mean free path of a single adatom. This situation leads to a rather narrow size distribution and a regular arangement of islands. The same effect has been observed for the growth of $Al$ on $Al(111)$ at low temperatures of $T = 50 \ldots 250$K [Rat97a]. This is a purely kinetic effect and the dominant self-organization process for temperatures below a threshold temperature $T_{\mathrm{th}}$.

At some point the mean free path becomes long enough to create islands that are no longer limited in their growth by the number of adatoms deposited in their vicinity but rather

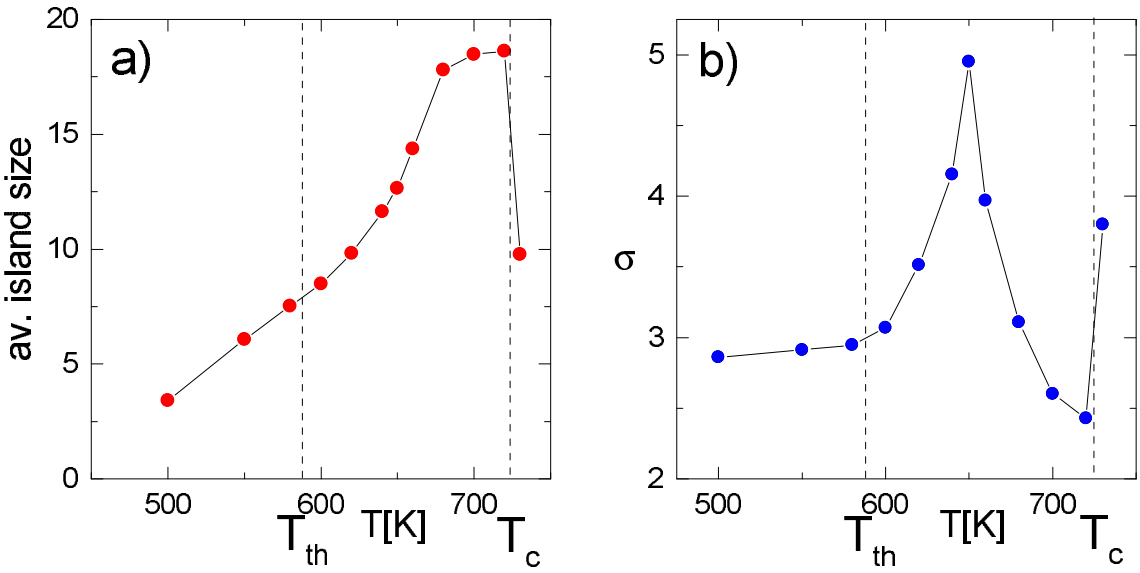


Fig. III.3: a) Temperature dependence of the average island size calculated from the size distributions. b) shows the standard deviation of the size distribution obtained from a Gaussian fit to the size distribution function. Threshold temperature $T_{\rm th}$ for beginning cooperative growth and the critical temperature for islanding $T_c$ are shown by vertical lines. Parameters: $f = 0.1$Ml/s and $c = 30\%$, simulation time: 3s.

by the increasing strain that destabilizes the island perimeter.

With increasing temperature above $T_{\rm th}$, more and more atoms will detach from existing, larger islands, thereby increasing the monomer density in the system, and thereby support island nucleation and the growth of smaller islands. Now islands grow in a cooperative growth mode where small islands grow at the expense of larger ones with less stable boundaries.

The cooperative growth is solely caused by strain. Without the strain energy correction $E_{\rm STR}$ one would expect Ostwald ripening [Zhd99] as has been shown in [Bos00].

To further classify the quality of the size distributions, one has to consider the width of the distribution that can be derived from the standard deviation of the average island size. The result is shown in Fig.III.3b.

In the purely kinetically controlled regime the deviation from the average island size is about constant. If the temperature is increased about $T_{\rm th}$ the deviation changes to considerably larger values and assumes a maximum at $T = 650$K. Here, the cooperative growth is the reason for the inhomogeneous island size distribution. A few large islands, making up the upper part of the size distribution, loose atoms that are collected by islands that are still small or have just nucleated. These small islands are growing rapidly but right after the end of deposition they broaden the size distribution noticeably.

If the temperature is increased further, the size dispersion is again decreasing since the cooperative growth proceeds fast and the exchange of material between islands is more efficient. Smaller islands are growing so fast, that at the end of deposition only few islands have not yet reached a size where attachment balances detachment.

For temperatures close to $T_c$ the deviation of average sizes is even smaller than in the kinetic

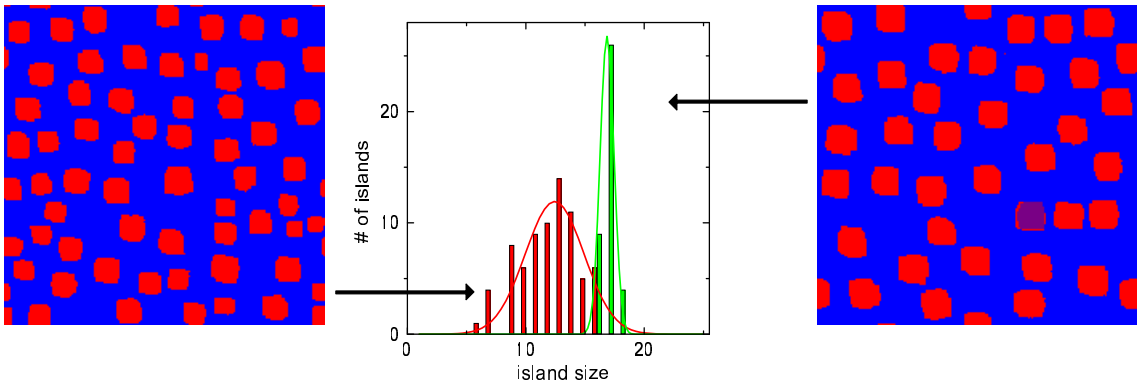


Fig. III.4: Effect of growth interruption on size ordering. Shown is in red the size distriution in a system with $T = 650$K, $f = 0.1$Ml/s and $c = 30\%$ after the end of deposition and in green after a growth interruption of 100s. Corresponding Gaussian fits as used for the determination of the standard deviation are also shown. To the left and to the right the corresponding island distributions are plotted (first layer: red, second layer: purple).

regime since the islands come ever closer to their well defined equilibrium sizes, defined in Chap.IV.

It should be noted that for certain material systems energetically favourable island sizes, so called magic island sizes exist, which have a clear impact on growth kinetics and size distribution [Sch95]. Size quantization effects can also be observed in $InAs$ self-assembled quantum dots on $GaAs$ [Sch97a].

## III.3 Growth interruption

For the case discussed so far, where the morphological evolution of the quantum dot layer is stopped after the deposition, the main influence of temperature is to suggest a preferred island size by kinetic effects for low temperatures. If the temperature is high enough to allow close to equilibrium distributions of sizes, it seems opportune to choose a temperature close to the critical point $T_c$, to take full advantage of equilibrating processes and thereby reduce effects that result in a large size dispersion.

The whole problem looks, however, different, if the system is allowed to equilibrate by the introduction of a growth interruption and it is known that a growth interruption has a smoothing effect on crystal surfaces [Kam96]. As an example of how remarkably the surface morphology can change during equilibration, in Fig.III.4 the island distributions before and after a growth interruption of 100s are plotted together with the corresponding histograms of the size distribution.

It has been argued above, that for the particular choice of parameters for this system, right after the end of deposition the size dispersion assumes a peak value. Suprisingly, after the growth interruption the system exhibits an almost perfect size ordering. In the following the effect of growth interruptions will be discussed im more detail.

After a growth interruption of 100s the average size of islands is plotted vs. temperature in Fig.III.5a. In the low temperature regime the average size of the islands has shifted towards larger islands. The shift in comparison to the plot in Fig.III.3 is the more pronounced the higher the temperature is. At the threshold temperature $T_{\rm th}$ the increase to-

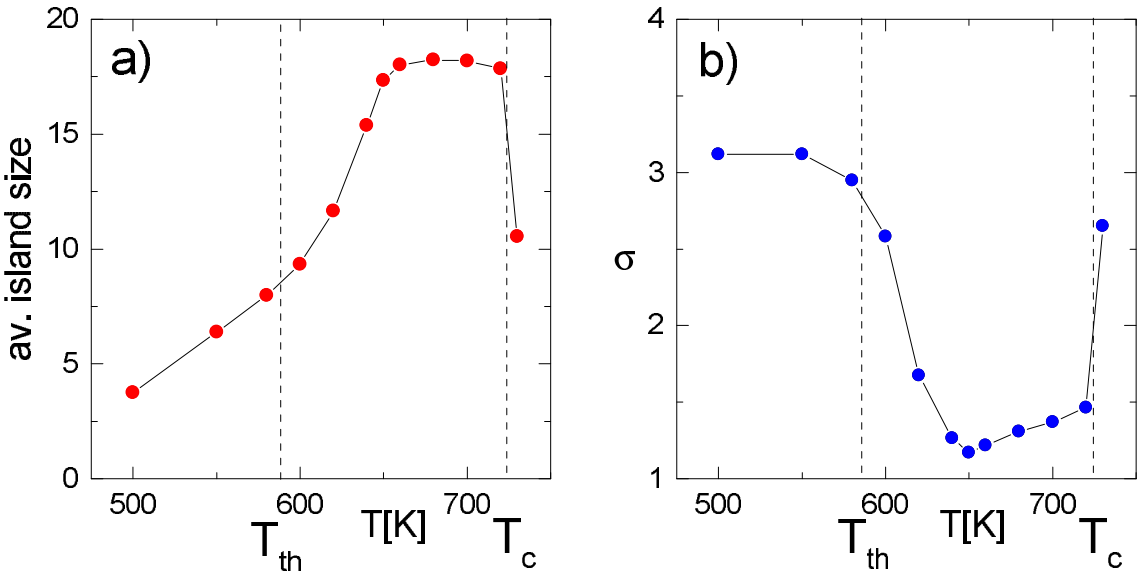


Fig. III.5: Same as in Fig.III.3 but after a growth interruption of $t_{\rm ir} = 100$s. a) Temperature dependence of average island size and b) standard deviation of size distribution. Parameters: $f = 0.1$Ml/s and $c = 30\%$.

wards equilibrium sizes is very fast. Once the optimal size is assumed, it does not change with temperature until the critical point $T_c$ is reached[3].Consequently, if a growth interruption is introduced, it is not necessary to use growth temperatures close to the critical point $T_c$ to obtain islands of equilibrium size. It is, on the contrary, a better choice to choose a lower temperature, as a look on the dependence of the size dispersion on temperature in Fig.III.5b reveales.

For the temperature $T_{\rm opt} = 650$K the size dispersion assumes a minimum while for higher temperatures the size distribution broadens again. This effect is expected for equilibrium size distributions that experience an entropic broadening with increasing temperature.

To conclude the effect of temperature on the size distribution, the whole temporal evolution of the average size for four exemplaric systems is shown in Fig.III.6.

During the first three seconds of deposition the average size of the islands increases fast. The islands grown during this time are the larger the larger the temperature is. During the following 100s of growth interruption the islands approach their equilibrium sizes. While the change in average size for the colder systems with $T = 550$K and 600K is negligible, generally the process of equilibration is again faster in hotter systems.

An interesting effect can be seen in the system of $T = 700$K (red curve in Fig.III.6). After deposition the average island size is larger than the equilibrium size and during equilibration the islands shrink. Presumably, this effect is due to oversaturation, where the existing islands due to the strain field loose atoms, which can not find an appropriate, less strained island to attach to. Consequently, the number of islands will remain constant and the average island size can only decrease if a new island nucleates. This situation will be encountered

3. In fact the equilibrium size is shrinking with temperature but in these simulations this effect is concealed by noise. However, it can be made visible by noise reduction, as it is done in Chap.IV.

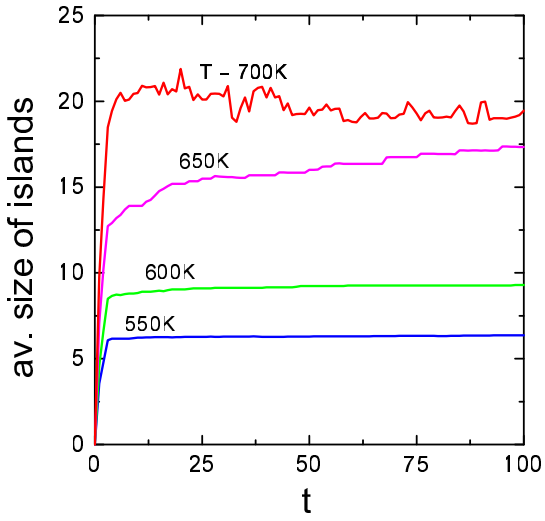


Fig. III.6: Temporal evolution of the average island sizes for temperatures between $T = 550 \ldots 700$K. Parameters: $f = 0.1$Ml/s and $c = 30\%$ as in Fig.III.5 and Fig.III.3.

again later on in the case of high coverages, when the whole surface is covered densely with islands and no suitable nucleation sites exist. Additionally, in high temperature systems the nucleation of new islands is hindered by the relative instability of dimers, since then only dimers or trimers can act as island nuclei.

This situation will be revisited in Chap.IV when the transition from kinetics to the thermodynamically controlled growth regime is considered.

## III.4 Flux rate

The flux is a measure of how fast material is deposited on the surface. It does not enter any equation concerning processes connected to self-organization, like the definition of diffusion barriers or the strain field. Thus, the flux rate influences the kinetics of growth only indirectly by determining the density of monomers on the surface and thereby the mean free path of adatoms, the nucleation rate of islands and by determining the time scale of free diffusion between two deposition events.

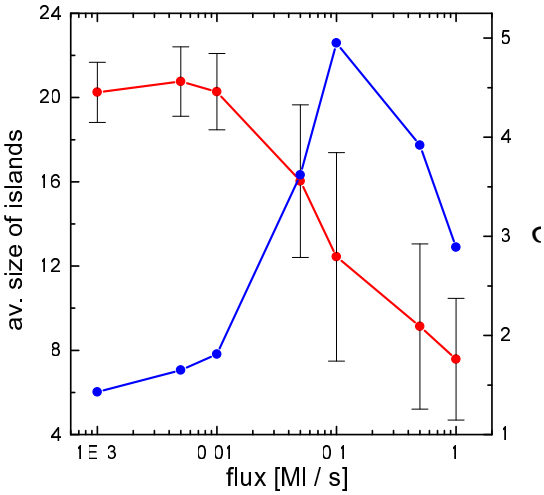


Fig. III.8: Analysis of Fig.III.7. Average size is shown in red in dependence of flux rate. The standard deviation is shown in blue and as error bars. Parameters: $T = 650$K and $c = 30\%$. Note the logarithmic scale for the flux.

Since flux is only present during the time of deposition, one might assume that it is even less important dominant during growth interruptions. At least this assumption is, to some extent, true since the same island distribution will evolve during equilibration in the same way, given the same set of parameters. In this sense, the system has no memory of the flux, that led to a particular island distribution dur-

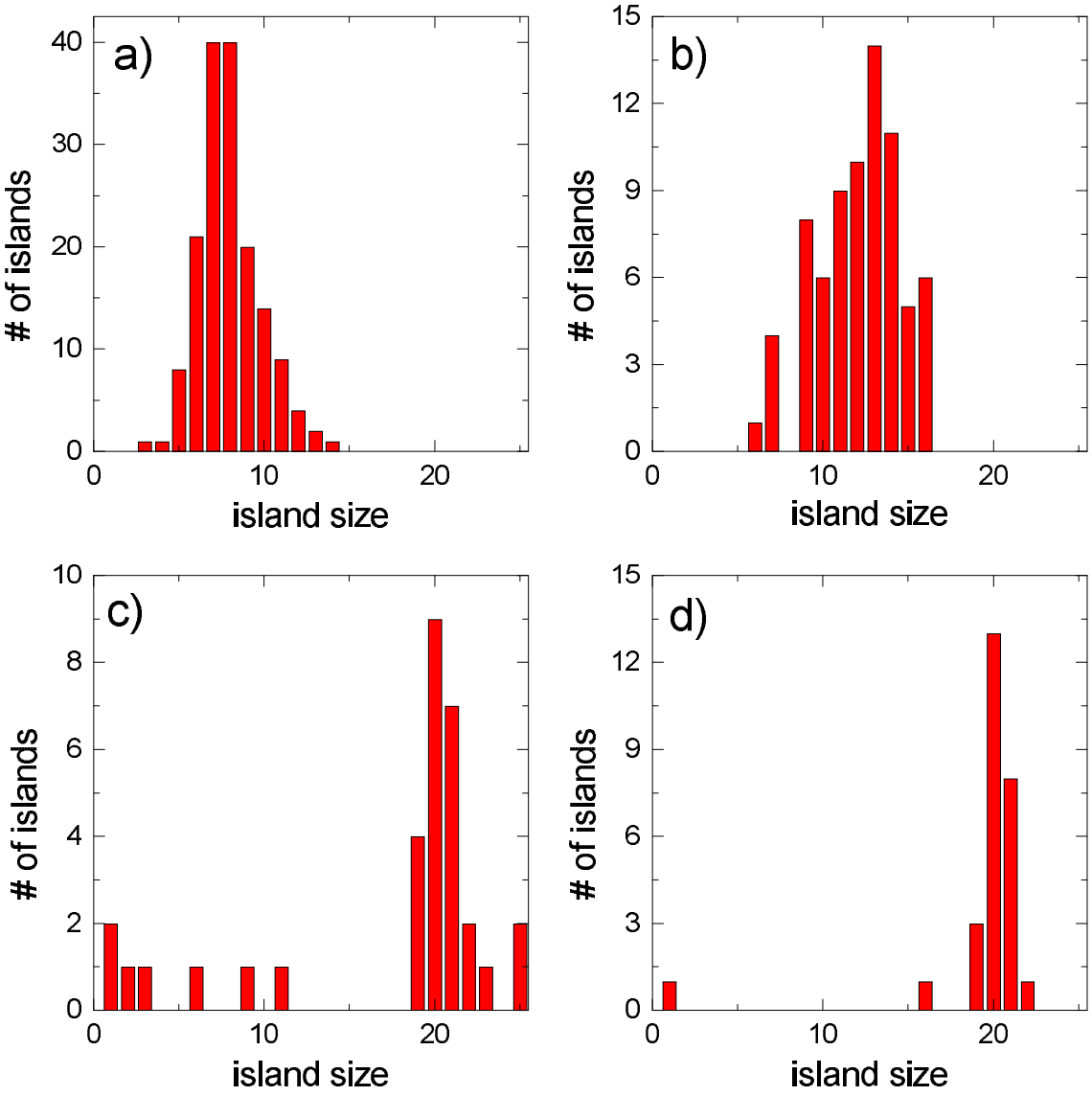


Fig. III.7: Influence of flux rate on the size ordering. The size distributions for the same system of $T = 650$K and $c = 30\%$ are shown for different fluxes. a) $f = 1.0$Ml/s, b) $f = 0.1$Ml/s, c) $f = 0.01$Ml/s and d) $f = 0.001$Ml/s. Data refer to the end of deposition after a) 0.3s, b) 3s, c) 30s and d) 300s simulation time.

ing deposition. However, different values of flux can lead to significant differences in the surface morphology after the end of deposition. In the following a system at temperature $T = 650$K and a coverage of $c = 30\%$ is considered for different fluxes. In Fig.III.7 the size distributions right after the deposition of a $30\%$ coverage are shown[4].

In Fig.III.7a many small islands have formed. Despite the comparatively high tem-

4. Note that the time for reaching the end of deposition is different in the four systems. We have 0.3s, 3s, 30s and 300s for the flux rates of 0.001Ml/s, 0.01Ml/s, 0.1Ml/s and 1Ml/s, respectively.

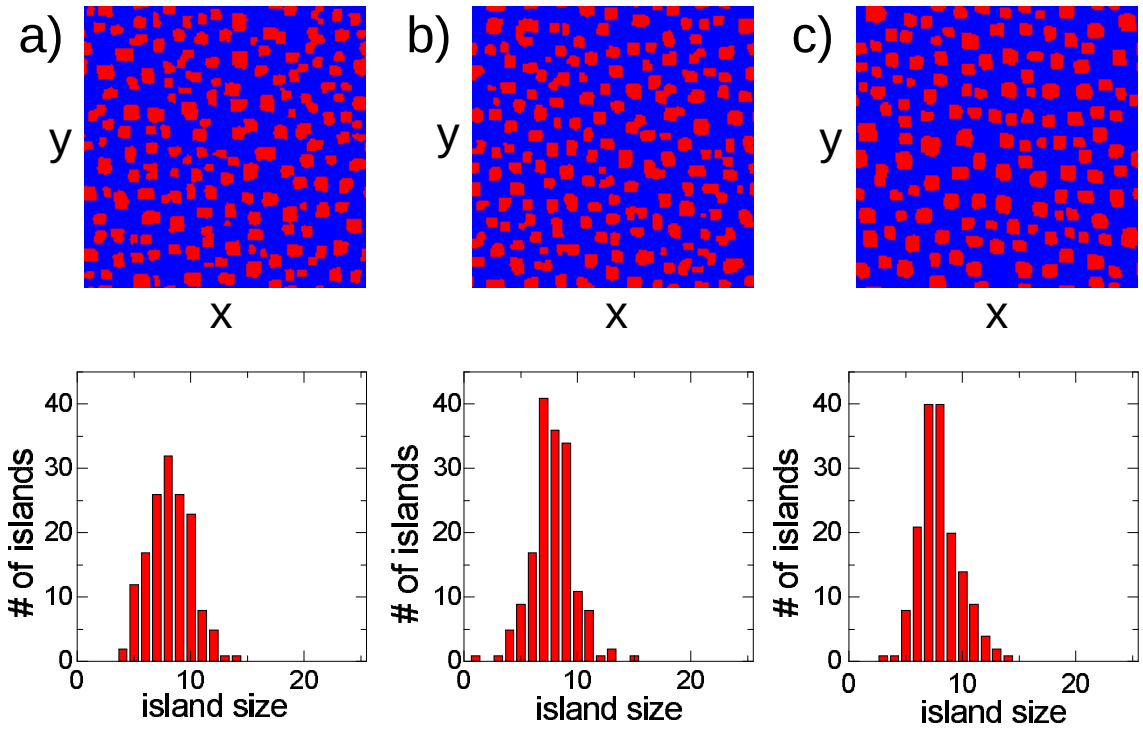


Fig. III.9: Similar size distributions for different growth parameters. The spatial distribution of islands and the corresponding size distribution are shown for the sets of parameters: a)$T = 550$K, $f = 0.01$Ml/s and $c = 30\%$, b) $T = 600$K, $f = 0.1$Ml/s and $c = 30\%$ and c) $T = 650$K, $f = 1.0$Ml/s and $c = 30\%$

perature of 650K the islands do not have enough time to assume their equilibrium size and consequently the size distribution looks like a low temperature distribution encountered in the previous section, where the growth was purely determined by kinetics. If the flux is decreased by a factor of ten Fig.III.7b, the size distribution has clearly changed. Now, the system is obviously approaching equilibrium by cooperative growth of islands characterized by a broad size distribution. By decreasing the flux rate even further, the system has enough time during the deposition process to come close to an equilibrium size distribution Fig.III.7c. The islands show a small size dispersion around the equilibrium size of about twenty atoms in diameter. The same result is obtained for a flux of 0.001Ml/s in Fig.III.7d, where the size dispersion is again slightly reduced.

To sum up the results obtained for different flux rates, the average island size and the dispersion of the size distributions is shown in Fig.III.8.

As can be seen from the results presented above the decrease in flux is in some sense comparable to an increase in temperature. Fig.III.9 shows, that quite similar surface configurations can be obtained if the effect of a higher flux is compensated by an equivalent increase in temperature. This can be understood, at least qualitatively, by the following reasoning.

If atoms with nearest neighbor bonds are assumed to be immobile, which is reasonable at least for low temperatures, the sur-

face morphology is basically determined via the interplay between nucleation events and attachment of adatoms to existing islands. The higher the monomer density on the surface is, the more important become nucleation processes. If only few single adatoms are on the surface, nucleation of islands by the accidental meeting of two monomers is much less likely. In this case most adatoms will attach to existing islands.

Consider now a situation, where a certain temperature $T_0$ and a flux $f_0$ generate a monomer density $d_0$ at a given time during the growth process. If the flux is increased to $f_1$, the monomer density will as well increase to, say, $d_1$. If now the temperature is increased to a distinct value $T_1$ the adatoms efficiently diffuse faster. Now, in the same amount of time more adatoms will make contact with an island on the surface, to which they can stick. Subsequently, the monomer density is again decreased to $d_0$.

In this simple picture, both pairs of parameters $(T_0, f_0)$ and $(T_1, f_1)$ result in the same growth kinetics and consequently in the same surface morphology. This is quantified by the scaling law which states that the configuration scales with $D/f$ where $D = D_0 \exp(-E/kT)$ with $E \approx 1$eV.

## III.5 Surface coverage

The coverage describes, how much material is deposited on the surface. It certainly has an effect on size distributions, since one can not expect islands of equilibrium size if not enough material is deposited. On the other hand, if more material is transported to the surface than necessary for optimal island sizes, small amounts may be compensated by a reduced distance of islands. At some point, however, islands will have to merge or make a transition from in-plane growth to three dimensional growth. In the following, this point will be referred to as the critical coverage denoted as $c_c$.

At least for coverages below the critical point $c_c$ and for low temperatures, where the growth is mainly kinetically controlled, the effect on the size distributions caused by a variation of coverage should not be influenced by such effects and one should expect an increase of the average island size with the coverage. Since in this regime every island collects adatoms from its immediate vicinity without any considerable exchange of material between islands, its size is directly determined by the amount of the deposited material around the island.

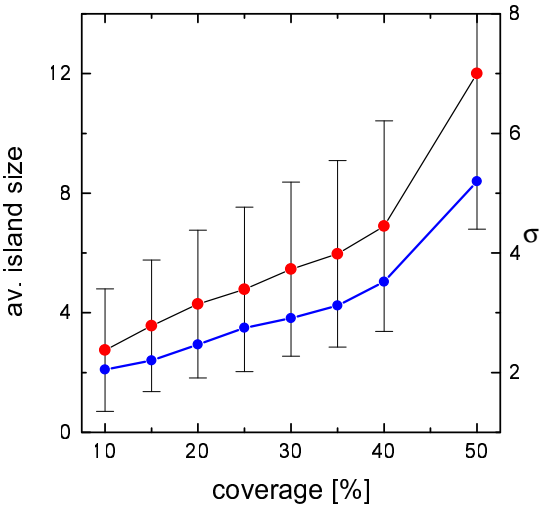


Fig. III.10: Dependence of average island size (red) on coverage after the end of deposition in a kinetically controlled system. The width of the size distribution $\sigma$ is shown as error bars and as blue dots (right scale). Parameters: $T = 550$K and $f = 0.1$Ml/s.

In Fig.III.10 the average size of islands in a system at $T = 550$K grown with a flux of $f = 0.1$Ml/s is shown for different coverages right after the stop of deposition. It is interesting to note that the increase of average island size is linear, which can only be expected

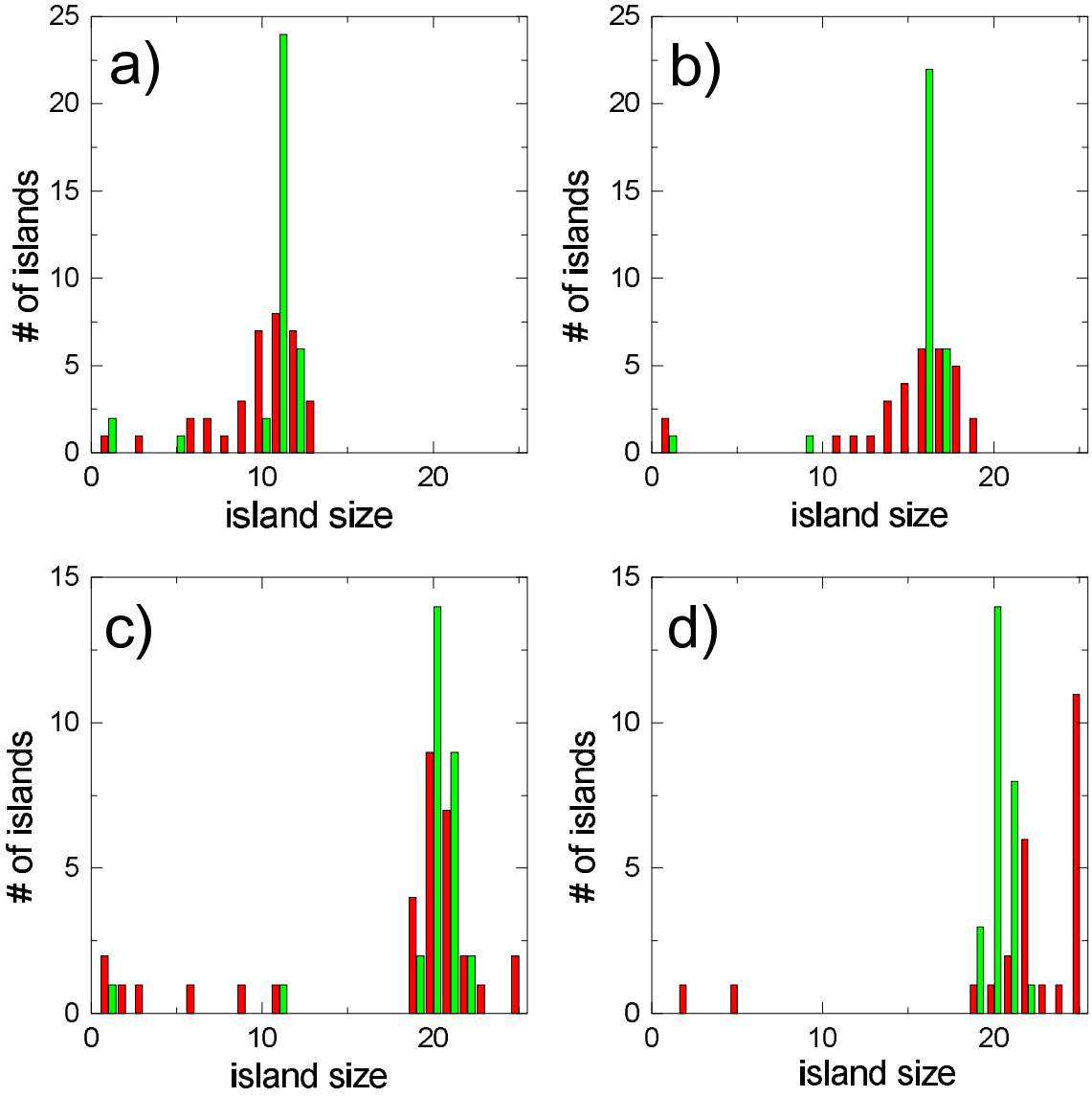


Fig. III.11: Corresponding size distributions to Fig.III.12. Size distributions found after the end of deposition are shown in red. Distributions for the relaxed systems after a growth interruption of 100s are in green color. Parameters: $T = 700$K and $f = 1$Ml/s for all plots and a) $c = 10\%$, b) $c = 20\%$, c) $c = 30\%$ and d) $c = 40\%$.

for low coverages. Nevertheless, the linear increase in the average size continues up to coverages beyond the critical point $c_c$, where coalescence of islands should influence the size distribution. Only for a coverage of $50\%$ a clear increase of the average size as well as in the size dispersion can be seen.

If the temperature is increased and the mean free path becomes longer than the average island separation, the qualitative behaviour changes. In Fig.III.11 the size distributions for a system of temperature $T = 700$K and a flux

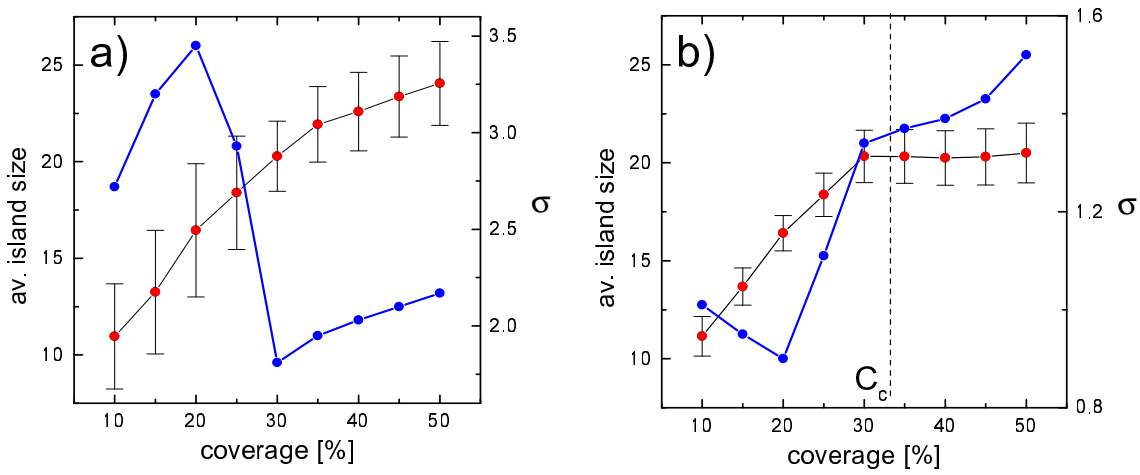


Fig. III.12: a) Dependence of average island size on coverage for cooperative growth conditions after end of deposition. The average size is shown as red circles. The corresponding width $\sigma$ of the size distribution is shown in blue and as error bars. b) The same as in a) but after a growth interruption of 100s. The critical coverage $c_c$ for beginning of three dimensional growth is denoted by a vertical line. Parameters are $T = 700$K and $f = 1$Ml/s.

rate of $f = 1$Ml/s for different coverages are shown. Red and green colums refer to size distributions before and after a growth interruption of 100s, respectively. In Fig.III.12a and b the corresponding average sizes and dispersion in dependence on coverage are presented for the unrelaxed and the relaxed case, respectively. First, the unrelaxed case will be discussed.

In Fig.III.11a and b broad size distributions can be found after the stop of deposition. Islands that have nuleated very early during deposition have more time to collect atoms and will consequently have reached a larger size at the end of deposition than islands that have nucleated later. Hence, the size distribution compared to colder systems broadens for subcritical coverages.

A considerable narrowing of the size dispersion is observed, if the coverage allows for near equilibrium size islands (Fig.III.11c). Here, the induced strain destabilizes the island boundaries and thus limiting the island size. Smaller islands grow cooperatively on the expense of larger islands.

For high coverages with $c > c_c$ coalescence of islands is observed (Fig.III.11d) and the size distribution broadens again. In Fig.III.11d the coalescence of islands creates a second peak in the size distribution at large island sizes. However, a cluster of two islands that have merged will in general not be stable and loose its surplus material to other, smaller islands.

If all the islands in the system have reached their optimal size and the lateral growth is hindered by strain, the additionally deposited material will increase the monomer density around the islands. This effect is comparable to an increase in the vapour pressure around a liquid droplet. Similar to this analogy the radius of an island increases to balance the higher rate of attachment of adatoms by an increased rate of 'evaporation' processes. Monomers can only be deducted by the nucleation of new islands or by surmounting a Schwöbel barrier and initiating three dimen-

sional growth in the next growth layer.

For the case when the growth temperature is above the threshold for cooperative growth $T_{\rm th}$, the significance of a growth interruption is considerable. For the green size distributions in Fig.III.11 the same systems as discussed above have been allowed to equilibrate for 100s. Now, the plots for all the coverages show remarkably narrow size distributions. For low coverages the average size increases (Fig.III.12) with the amount of the deposited material up to the critical coverage $c_c$. From here on the average size remains constant.

In the systems of low coverage the islands have not yet reached their equilibrium size, however, the cooperative growth has induced a narrow size distribution. This effect can not be found for temperatures below $T_{\rm th}$.

It might be suprising that even the systems with an over-critical coverage show a size distribution that is centered about the equilibrium size. One would rather expect to see larger islands since more material has been deposited. Though, in comparison to a $30\%$ coverage, which is below $c_c$, the system with a $40\%$ coverage has a slightly reduced average distance between islands. This fact can, however, not account for the whole additionally deposited material. The difference in the average distance is only of the order of one or two lattice constants, giving room for maybe two more islands. But an increase in coverage from $30\%$ to $40\%$ results in some six additional islands of diameter 20.

The solution to the problem of the missing adatoms can be found by looking at the island distributions in Fig.III.13

For a $40\%$ coverage many atoms have surmounted the Schwöbel barrier and entered the second growth layer on top of existing islands. In some cases the islands have an almost complete second layer or even partly filled higher growth layers. Once an island has nucleated on top of another island it is growing fast since it is unlikely to loose atoms which would have to cross the Schwöbel barrier again to escape.

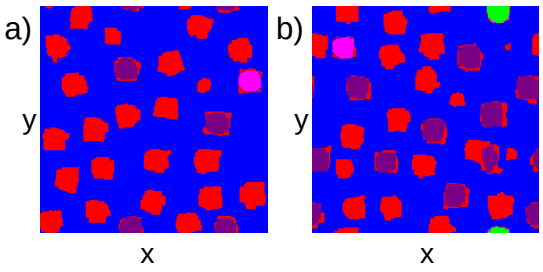


Fig. III.13: Island distributions demonstrating the transition from 2D growth to 3D growth. a) System with a coverage of $30\%$ and b) with $40\%$. First growth layer is red, second purple, third magenta and the fourth layer green. Parameters: $T = 700$K and $f = 1$Ml/s.

### III.5.1 Spatial ordering

So far, the spatial ordering has not been considered at all, and as it turns out, an appropriate coverage is crucial to observe spatial ordering effects. However, spatial correlation can also be obtained by growing quantum dots on patterned surfaces [Lee98a, Kon98a, Xie95b, CC95], which, of course, implies difficult preprocessing of the growth substrate.

While the mechanism of size ordering as far as the thermodynamically controlled growth regime between $T_{\rm th}$ and $T_c$ is concerned, is caused by the destabilizing of the island boundaries by strain and a reduced probability of attachment, spatial ordering can only be achieved, if whole sections of existing islands are rearranged.

Not only that more material has to be moved, the relevant island-island interaction is much weaker than the island self-interaction responsible for size ordering. In both cases the elastic strain energy mediates the interaction. The absolute value of strain is largest at the boundary area of an island and the size lim-

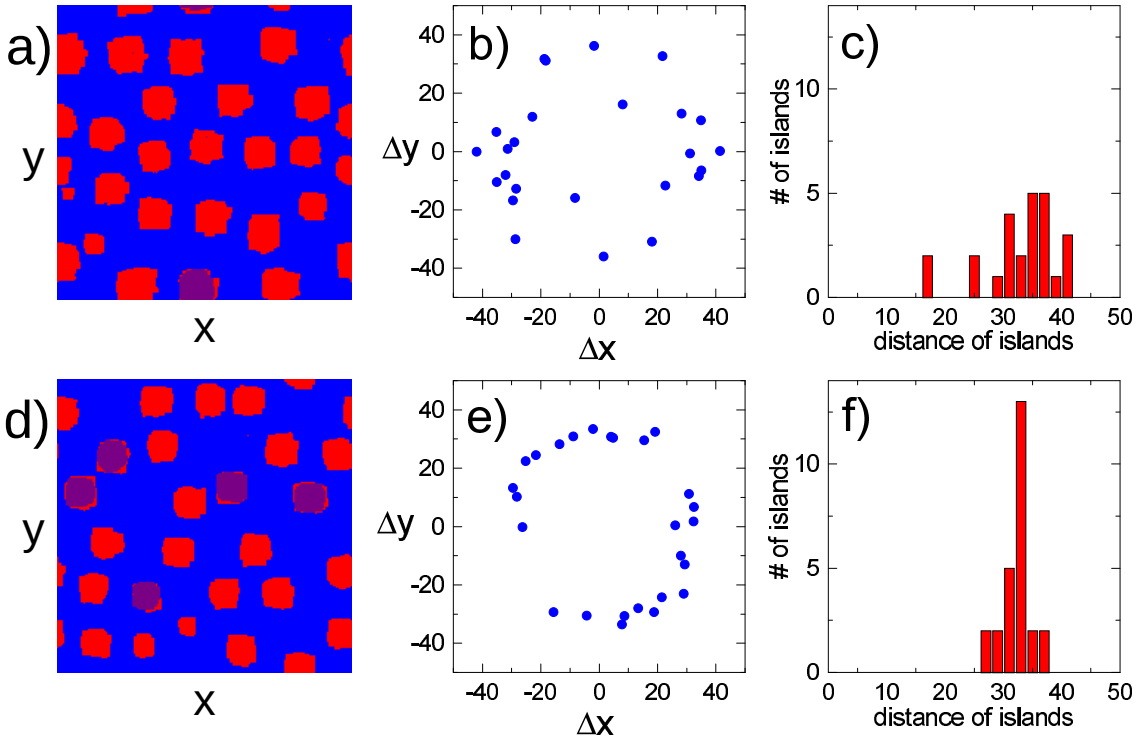


Fig. III.14: Effect of growth interruption on ordering of distances. The first row of pictures corresponds to the end of deposition, the second row to the relaxed system. a) and d) show the island distributions, b) and e) the spatial distribution of the nearest neighbor distances and c) and f) the distance distributions. Parameters: Growth interruption 100s after the end of deposition, $T = 700$K, $f = 0.001$Ml/s and $c = 30\%$.

iting effect is very efficient. With increasing distance from the island the strain energy decays like $1/r^3$ (see Fig.II.10). Thus, the interaction between two islands that induces spatial ordering, is at least by an order of magnitude weaker than for the size limiting processes.

Therefore, self-organization effects in the spatial ordering can only be expected, if the considered system is able to respond to little differences in energy barriers in a comparatively short amount of time. This is only possible for adatoms with a high mobility or, equivalently, in systems with high temperature growth conditions. Additionally, the islands have to be as close together as possible to maximize the island-island interaction. This calls for a system with a critical or even slightly above critical coverage. The third ingredient towards achieving spatial ordering is the introduction of a growth interruption since even in systems with a temperature close to $T_c$ self-organized spatial ordering is a slow effect.

By assessing the spatial ordering, one has to differentiate spatial ordering in the distance between islands from a regular arrangement of islands in a periodic array. In the latter case in addition to similar distances between the islands a preferred direction, in which the islands align, is required.

Generally, the ordering with respect to distances is more easily achieved and will be discussed first. To demonstrate the importance of a growth interruption, in Fig.III.14 the nearest neighbor distributions after end of deposition

and after 100s of relaxation are shown together with the histograms of the distances.

Despite the fact that deposition took place with an extremely low flux rate of $f = 0.001$Ml/s, at the end of deposition the ordering in the distance is poor. After the growth interruption, however, the spatial ordering has improved dramatically and the distribution around an average distance of some 31 lattice constants between the centers of mass of two neighboring islands is quite narrow.

Fig.III.15 shows an overview of the average distance between neighboring islands and the related dispersion in dependence of coverage.

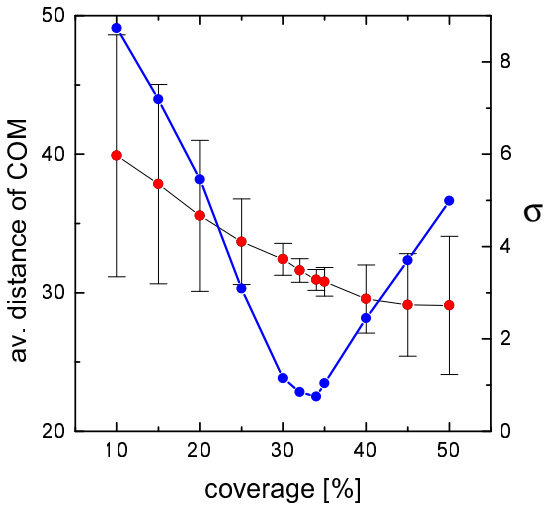


Fig. III.15: Influence of coverage on spatial ordering with respect to distances. The average distance of centers of mass is plotted vs. the coverage as red circles for systems with $T = 700$K and $f = 0.001$Ml/s. The standard deviation $\sigma$ of the average distance is plotted in blue and as error bars.

As can be seen, the ordering in distances is best for a coverage of $34\%$. For lower coverages, the effect of spatial ordering is suppressed by the larger average distance between islands. This results in a weaker island-island interaction. Additionally, for coverages below $30\%$ the average island size decreases, since the optimal, equilibrium size is not yet reached. Since smaller islands result in weaker elastic strain fields, again, the island-island interaction is reduced.

For coverages larger than $34\%$ the ordering in distances is as well less pronounced despite the further reduction of the average distance between the islands, which would suggest a stronger interaction and a better spatial ordering. Probably the reason for the increasingly bad spatial ordering for coverages above $c_c$ is the beginning of three dimensional growth. Islands that have started to develop a second growth layer cannot rearrange as easily as a monolayer island, since twice the amount of material has to be moved. This effect would account for less flexibility in the response to island-island interactions and consequently lead to a poorer distance ordering.

## III.6 Optimized set of parameters

With this information in mind, it should now be possible to define an optimal set of parameters for the growth of self-organized islands that show a good ordering in size as well as in the spatial aspects of distance and arrangement. Since the spatial ordering is the most difficult feature to obtain, parameters will basically have to provide optimal conditions for spatial ordering. However, pronounced spatial ordering is always accompanied by a narrow size distribution. This is easily understood, for the spatial equilibration induced by island-island interaction consumes considerably more time than equilibration of sizes. Thus, spatial ordering among islands always implies size ordering as an additional feature.

At this point it should also be mentioned that regular arrangement of islands can also be seen in systems that are purely kinetically driven. The example of $Al$ on $Al(111)$

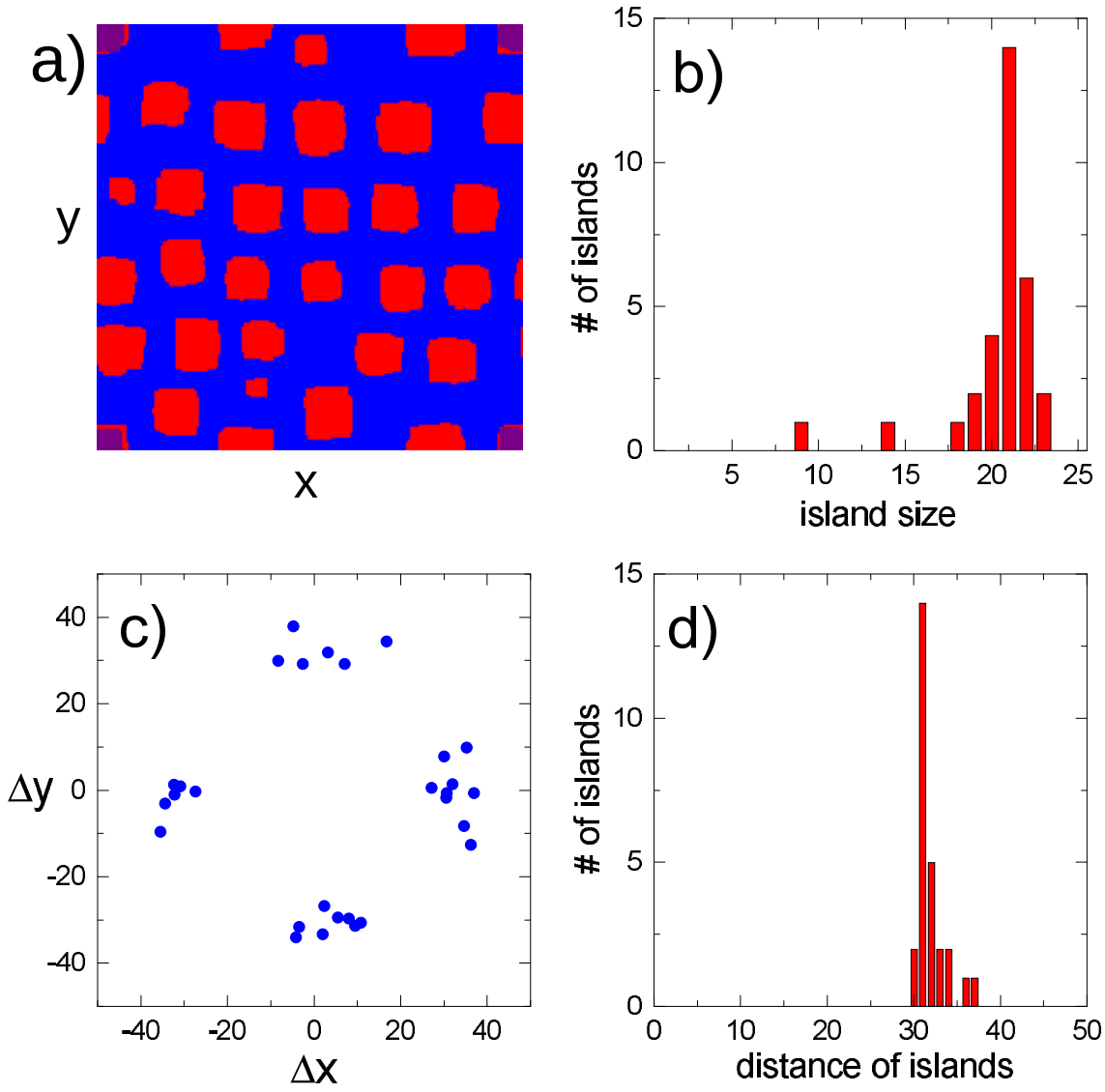


Fig. III.16: Simulation result for a set of parameters optimized towards spatial ordering. In a) the spatial island distribution and in b) the corresponding size distribution is shown. Plot c) shows the distribution of distances of the centers of mass and d) the resulting distance distribution. Parameters are $T = 700$K, $f = 0.001$Ml/s, $c = 34\%$ and a growth interruption of $t_{\mathrm{ir}} = 500$s after the end of deposition.

[Rat97a] has already been mentioned to produce a kinetically controlled and rather sharp size distribution. The same geometrical reasoning of circular areas from which the islands collect material, can be used to explain a certain spatial ordering observed in such systems, where the islands are arranged along hexagons, since this is the most effective arrangement to cover an area with circles with the least overlap.

In Fig.III.16 a simulation with optimal growth parameters for spatial ordering is shown. Already from the spatial distribution of islands (Fig.III.16a)it is obvious that here

not only ordering with respect to distances is present but also regular arrangement of the islands has been achieved. To this end it was necessary to equilibrate the system by a growth interruption of 500s. As is expected, the size ordering is very good (Fig.III.16b) as well. This should, however, not be much of a suprise, since the long growth interruption allowed the system to approach its equilibrium state with a well defined average size of islands and a preferred spatial arrangement that minimizes the island-island and island-self interaction energies [Shc00].

It should be noted that such a thermodynamical optimum is not approached in the case of ordering effects in kinetically controlled systems, hence these systems are far from their equilibrium state. Here, size ordering and spatial arrangement are pure kinetic effects that are not persistent and will decay if the system is allowed to evolve.

Though it is true that for a given set of parameters a well defined equilibrium state exists, this energetically favoured state will, especially for lower temperatures, hardly ever be reached. The process of equilibration might take a couple of hours to several days and it is very questionable if growth parameters and the absence of contaminating substances inside the growth reactor can be kept up for such a long time.

From this point of view it appears more promising to use kinetically controlled growth conditions, which are dominant during the deposition anyway, to create a proper island distribution. Subsequently this distribution can approach the desired equilibrium state during a growth interruption with different growth parameters much more efficiently.

## III.7 Other Monte Carlo simulations

Already in 1983 a very ambitious paper [Mad83] addressed the Monte Carlo method as the proper tool to handle the simulation of surface growth kinetics during MBE heteroepitaxy including deposition, desorption, diffusion and strain in the presence of crystal defects and impurities. The author also indicated a possible structure of Monte Carlo program code but did not present any simulation results.

However, the basic idea of simulating surface growth by means of the Monte Carlo method was fastly adopted by the surface science community and an impressive number of Monte Carlo simulators have evolved during the years. A considerable amount of insights into growth processes has been contributed by the use of Monte Carlo techniques and a couple of interesting, numerical investigations related to surface growth will be presented in the following.

It should be noted that in most Monte Carlo simulations the elastic strain field is not taken into account. Some exceptions are presented in III.7.3.

### III.7.1 Effects in surface growth

Already simple Monte Carlo simulations, which include only a repulsive, non-extended interaction between dimers diffusing along a crystal surface generate ordered patterns, as is reported in [RP98]. By using Coulomb interactions between surface particles, various periodic structures and surface reconstructions can be found in the homoepitaxial system $Si$ on $Si(111)$ if the particles are allowed to diffuse [Wat97].

Furthermore, high temperature Monte Carlo simulations of $Ga$ desorption during MBE deposition of $AlGaAs$ on $GaAs$ have been performed in [Mah97].

The surface reconstruction is found to have a clear impact on growth kinetics by influencing the diffusion coefficient. Surface diffusion, for example, becomes highly anisotropic for hydogen on the $(2 \times 1)$ reconstructed surface of tungsten ($H/W(001)$ [Nie98]. In this paper various surface reconstructions of tungsten and their influence on the diffusion of $H$ have been analyzed by Monte Carlo simuations. In [Gha88a] computer simulations are reported, which connect surface reconstruction, stoichiometry and strain in molecular beam epitaxial growth to defect formation in the growing adsorbate.

Ehrlich-Schwöbel barriers have an influence on growth kinetics as well. Schwöbel barriers, for instance, are investigated in one and two dimensions analytically in [Mus98] to yield effective diffusion coefficients. These are validated with Monte Carlo simulations of diffusion in the presence of Schwöbel barriers. In a three dimensional system [Köh00] time resolved in-situ STM measurements have been applied to $Fe/Fe(110)$ and $W/W(110)$ homoepitaxial islands. The results were then compared to Monte Carlo simulations. It turned out that Schwöbel barriers stabilize certain facets in both homoepitaxial systems. Similar results are reported in [Tür96]. Here, three dimensional Monte Carlo simulations of pyramidal quantum dot growth are performed including only diffusion. The presence of a Schwöbel barrier stabilizes $\{012\}$ facets.

### III.7.2 Homoepitaxial systems

If no anisotropy in diffusion induced by a certain surface reconstruction is present and diffusion processes are taking place on a lattice with high symmetry, pattern formation as the nucleation stage of quantum dot growth can nevertheless be found as in homoepitaxial systems [Sch98d].

By assuming anisotropic nearest neighbor bonds and diffusion, island nucleation on terraces is considered in [Iri96].

A Monte Carlo simulation of growth of $Si$ on $Si(001)$ including deposition and diffusion only is reported in [Lev98]. The simulations in three dimensions yield columnar structures and flakes. In a Monte Carlo simulation of the growth of $Si$ crystals from the melt stable facets are identified in [Bea00].

By accounting for both, diffusing kations and anions, in [Ish98] a two component Monte Carlo simulation of $GaAs/GaAs(001)$ homoepitaxial growth is used to reproduce RHEED intensity variations during growth on vicinal surfaces. $As$ determines the transition from 2D growth to step flow growth. Additional analysis on island shapes is given in [Ish99]. A very similar Monte Carlo study of $GaAs/GaAs(001)$ homoepitaxy finds transition between 2D growth and step-flow growth by, again, taking into account $Ga$ and $As$ as different species [Kaw99]. Here, island growth is determined by $As$ islanding. Furthermore $As$ serves as a self-surfactant in step-flow growth.

Another two-component Monte Carlo simulation of heterogrowth without the inclusion of strain efects can be found in [Gro00].

A transition from dendritic to compact islands is observed in Monte Carlo simulations of strain free island growth in two dimensions [Xia88]. First and second nearest neighbor interactions as well as anisotropic surface-attachment kinetics and surface diffusion are taken into account. Varied parameters are temperature, bond energies and supersaturation determining deposition.

In [Bal94] kinetic Monte Carlo simulations of nucleation and growth of two dimensional, unstrained islands on a square lattice are compared to mean-field rate equations. Again, a transition from ramified shape at low temperature to compact islands at high temperatures is found. Surface binding and nearest neighbor

binding is included. Attachment to islands is irreversible but diffusion along island edges is possible.

Another example of irreversible growth and nucleation of islands during submonolayer deposition on a perfect substrate with diffusive processes only is given in [Bar92, Bar95]. This Monte Carlo simulation assumes random walk diffusion and immobile islands after nucleation with no spatial expansion (point islands). An additional rate equation analysis with respect to size and separation of islands is done. The dependence on flux and diffusion constant $D$ is examined.

In [Wan00] a kinetic Monte Carlo simulation of facet growth is presented. Included effects are monomer and dimer diffusion as well as diffusion along ledges. The growth rates of facets with certain orientation is extracted.

2D island growth is studied in a Monte Carlo simulation as a function of coverage and ratio of diffusion constant to deposition rate [Rat94c]. Detachment from islands is possible at a rate determined by a pair bond energy. Diffusion is Arrhenius like with a binding energy to the surface $1.3$eV and nearest neighbor bonds $0.1$ to $0.3$eV taking place on a square lattice.

Monte Carlo simulations can also be performed on surfaces with other than a square symmetry. In [Mao99] the epitaxial growth on the hexagonal surface of $GaN$ is considered with diffusion processes only.

The growth on a surface with highly anisotropic surface reconstruction, the $Si(111)(7 \times 7)$ or so called DAS structure, is considered in [Kat99]. The Monte Carlo routine consideres diffusion processes only but is able to reproduce growth patterns observed experimentally.

### III.7.3 Heteroepitaxial systems

If heteroepitaxial systems are considered, an important additional ingredient has to be added to the simulation routines. In [Gha88b] the influence of compressive and tensile strain on the growth mode during epitaxial growth is addressed in a computer simulation study.

In [Tan97] Monte Carlo simulations of epitaxial growth on triangular $(111)$ layers are presented where the effect of a lattice mismatch is included by influencing atom-atom and atom-substrate bonds.

Deposition, diffusion and strain is included in a kinetic Monte Carlo simulation which is done in 1+1 dimensions (growth occurs orthogonal to particle diffusion) to simulate the transition from 2D to 3D growth [Kho00]. The strain is calculated via a spring model accounting for nearest and next nearest neighbors.

In [Liu01] a surfactant-mediated Monte Carlo simulation is presented which reports a strain induced transition from fractal island growth to compact growth with increasing strain field.

Strain is not only induced by heteroepitaxy. A Monte Carlo study of order-disorder transitions induced by defects on a perfect $Si(001)$ surface mediated by strain is considered in [Oka98].

A completely three dimensional Monte Carlo simulation including elastic strain but without diffusion dynamics is presented in [Rou98]. Elastic strain energy is included within the model of Valence Force Field (VFF) approximation. Strain and chemical binding energies between nearest neighbors lead to $(111)$ facets on quantum dots on zincblende substrates.

# IV.

# Kinetic vs. Equilibrium Size Distributions

In this chapter the growth dynamics of quantum dot systems with respect to their island size distributions will be scrutinized. In fact, growth kinetics during deposition of material is utterly different from equilibrium dynamics that can be observed in systems that have found their optimal, equilibrium state. The most obvious feature of these two different growth regimes is the emergence of two largely different size distribution functions that show an opposite dependence on temperature.

Under common growth conditions it is usually not clear, which process dominates and thus the relevance of kinetic size ordering or equilibrium dynamics is a matter of intense debate. In the following this very problem will be addressed by means of the Monte Carlo method. In particular, a focus will be put on the crossover from kinetic island formation to thermodynamically controlled size distributions, since it turns out that here both regimes of growth dynamics are relevant. Consequently, both forms of growth, kinetics and thermodynamics, have to be considered in quantum dot growth at different stages of growth [Mei01c].

## IV.1 Theory

Quantum dots have attracted considerable interest in recent years since they represent artificial atoms with unique, controllable optoelectronic properties. They provide the basis for constructing a novel generation of semiconductor devices [Bim99, Lor00]. To obtain highly efficient quantum dot layers for optical or electronical purposes it is not only of importance to grow dislocation-free quantum dots with a high spatial density, but it is also desirable to obtain a narrow size distribution that guarantees a large number of active dots for a specific voltage or optical wavelength.

A promising way of fabricating such structures is the self-organized formation of coherent quantum dots in the Stranski-Krastanov or Vollmer-Weber growth mode [Dar98, Shc98a]. In such heteroepitaxial systems the strain prevents Ostwald ripening, which is the dominant effect in homoepitaxy, and narrow size distributions of quantum dots are formed [Ng95, Bar97a, Wan99, Ram98, Sch98b].

### IV.1.1 Thermodynamical regime

If the quantum dot array is allowed to equilibrate, the average size of the dots follows from thermodynamic considerations

[Shc95b]. Since the entropic contribution plays a vital role, the average dot size decreases with increasing temperature down to single adatoms at very high temperatures. The quantum dot size distribution is thermodynamically controlled.

It should be noted that the statements met by thermodynamical equilibrium considerations presented in the following, as well as the Monte Carlo simulations apply only to two dimensional arrays of islands that emerge in heteroepitaxy at sub-monolayer coverage [Str98, Ale88]. It is assumed that these 2D-islands do not change much in size, shape or position during the 2D/3D transition and act as the basis for quantum dots [Pri95]. Consequently, morphological contributions [Mol98] to the considered energies can be neglected. Furthermore, arrays of highly dilute arrays are considered to exclude elastic island-island interactions. This assumption corresponds to low coverages well below ten percent.

For such systems the equilibrium concentration per unit atomic site of islands consisting of $N$ atoms $P(N)$ is given by the Boltzmann distribution

$$P(N) \sim \exp(-\varepsilon(N)N/kT) \qquad \text{(IV.1)}$$

where $\varepsilon(N)$ is the island energy per atom

$$\varepsilon(N) = -E_s + \frac{c_1}{\sqrt{N}} - \frac{c_2 \ln\sqrt{N}}{\sqrt{N}} \qquad \text{(IV.2)}$$

Here the first term $E_s$ denotes the binding energy to the surface, which is chosen to be $0.9$eV in the following simulations. The second term is the binding energy of the island boundary and the third term describes the elastic relaxation energy caused by the surface stress discontinuity at the island boundaries. The constants $c_1$ and $c_2$ can be calculated from the elastic constants of the considered material system. $c_1$ is proportional to the energy of a pair bond $E_b$. The constant $c_2$ can be obtained experimentally by calculating the strain field at the island boundaries or from elasticity theory following [Lan70][1]. The function $\varepsilon(N)$ is plotted in Fig.IV.1.

For zero temperature the size distribution is infinitely sharp with a preferred island size $N_0 = \exp(2(c_1/c_2 + 1))$ such that the elastic strain energy is minimized. This island size corresponds to the minimum of $\varepsilon(N)$ given by eq.IV.2 (see Fig.IV.1).

For finite temperatures, one has to consider the Helmholtz free energy with an entropic contribution and, following [Shc00], finds that the optimum size of an island is given by

$$N_{\text{opt}}(T) = N_0 - \frac{2\sqrt{N_0}}{c_2} kT \ln\left(\frac{8\pi kT N_0^{7/2}}{c_2 q^2}\right) \qquad \text{(IV.3)}$$

where $q$ is the total coverage. With increasing temperature the maximum of the size distribution given by eq.(IV.3) moves towards smaller islands. As an additional effect of the entropic contribution we find that the size distribution is broadened and a second maximum emerges at small island sizes due to the generation of individual atoms.

### IV.1.2 Kinetically controlled regime

On the other hand, often a contradictory effect to the thermodynamically controlled temporal evolution of island size distributions can be found experimentally, particularly if the system is cooled down or capped immediately after the formation of the dot layer. Here the average dot size increases with increasing temperature as has been observed, for example, for $Si/Si(100)$[Mo91]

1. One finds: $c_2 \approx 0.1$eV for both numerical and theoretical calculations. Note that for very large islands the numerical value of $c_2$ deviates from the theoretical one since the strain at an island boundary is limited by our code to one pair bond ($0.3$eV)

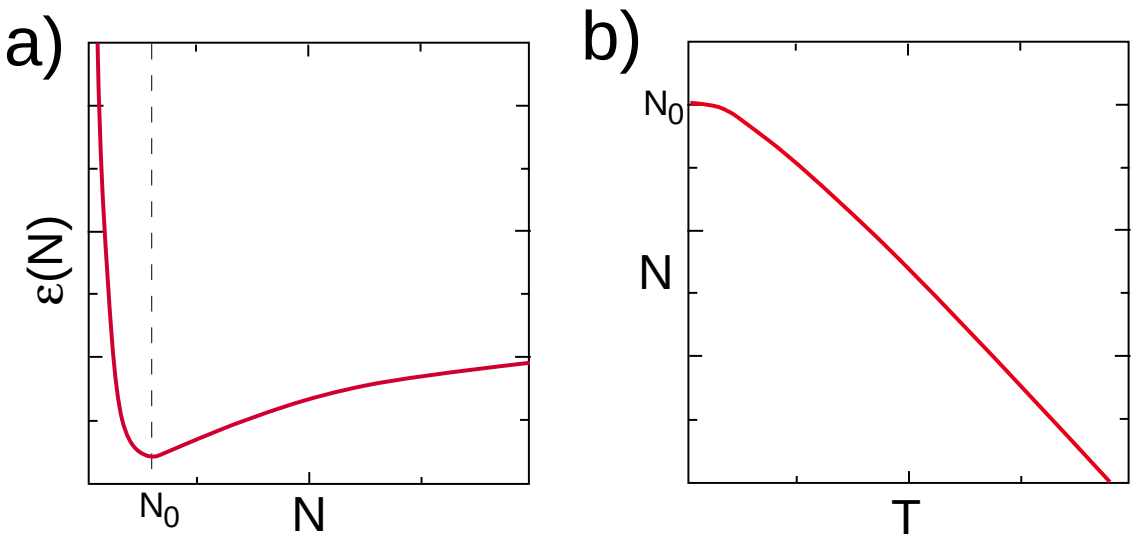


Fig. IV.1: a) Dependence of energy per atom in an island consisting of $N$ atoms given by eq.IV.2. b) Optimal island size in dependence of temperature given by eq.IV.3 for thermodynamically controlled island growth.

or $Au/Ru(0001)$[Wan91]. Due to the higher mobility of adatoms at higher temperatures the attachment to existing islands is more favourable than the nucleation of new islands. Thus for low temperatures many small islands are formed, whereas for high temperatures few large islands are observed. The size distribution is dominated by kinetic effects. For the same reason in homoepitaxy Ostwald ripening may be suppressed, and quantum dot arrays with a rather sharp size distribution may be grown [Zha98, Mo92].

For the case of kinetically controlled growth the interplay of diffusion and deposition is crucial. Diffusion is characterized by the diffusion constant $D$ given by

$$D = D_0 e^{-E/kT} \qquad \text{(IV.4)}$$

with $D_0 = \frac{1}{4} a_0^2 \nu$ a constant depending on the lattice constant $a_0$ of the crystal surface and $\nu$ the attempt frequency. The justification of eq.IV.4 and, especially, the independence of the factor $D_0$ of temperature is actually extremly difficult. Attempts to give a basis to eq.IV.4 have been done in form of the transition state theory [Gla41, Vin57].

For the case of irreversible island nucleation it is clear that the island density $n$ decreases with an increase of the ratio of diffusion to deposition rate. If $D$ increases, deposited atoms can – on average – travel farther between deposition events and aggregation to existing islands becomes more likely than nucleation processes, since nucleation necessitates the accidental clustering of two single adatoms[2] to build a stable nucleus for island growth. Hence, one expects a scaling relation of the form

$$n \sim D^{-\gamma}. \qquad \text{(IV.5)}$$

A mean-field approach to describe quantum dot formation is presented in [Dob97].

2. Depending on parameters like temperature, strength of nearest neighbor bonds and deposition rate the number of atoms to form a critical nucleus might be two or larger.

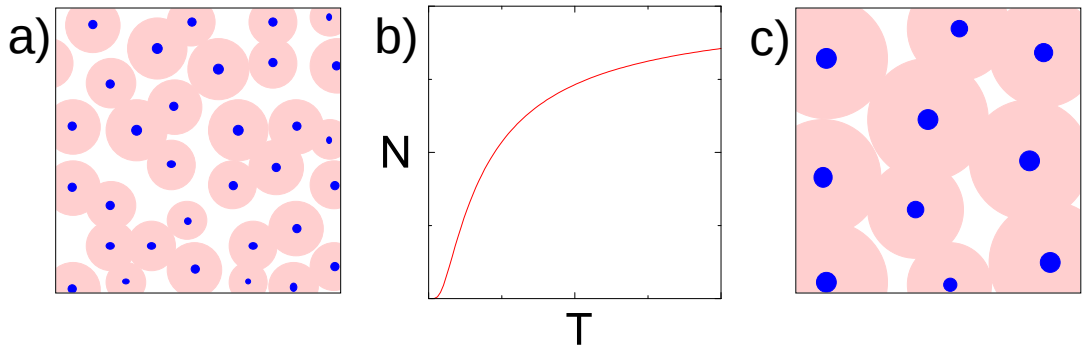


Fig. IV.2: Schematic island size distributions in the kinetically controlled regime for a) low and c) high temperatures. Islands are drawn in blue and pools of attraction in pink. b) shows the corresponding temperature dependence of the average island size $N$ for the kinetic regime (eq.IV.6)

In [Bar92] an equation for the dependence of the island density on temperature is derived

$$\begin{aligned} n &\sim \left(\frac{c}{D}\right)^{1/4} \\ &\sim \left(\frac{c}{D_0}e^{E/kT}\right)^{1/4} \end{aligned} \qquad \text{(IV.6)}$$

with $c$ the relative surface coverage. The same exponent $\gamma = 1/4$ has been recovered by [Jen94] in a deposition-diffusion-aggregation model. Growth exponents for a one dimensional system have been obtained by means of rate equations in [Lai91].

Furthermore, in the kinetically controlled regime during deposition a characteristic diffusion length $l$ can be defined as the average distance between nucleation sites. It is [Ven84, Sch95]

$$l \sim \left(\frac{D}{f}\right)^{\gamma} \qquad \text{(IV.7)}$$

with $f$ the flux rate to the surface. The same result has been obtained by means of Monte Carlo simulations in [Gha92].

This leads to the following situation depicted in Fig.IV.2. Fig.IV.2a) and c) show the schematic island distributions at low and high temperatures, respectively. The characteristic diffusion length $l$ for low temperatures is short. So is the average distance an adatom can travel before meeting another adatom. Consequently, the radius of the area, an existing island can draw adatoms from (pink circles in Fig.IV.2a) and c)) is small and more islands will nucleate. This results in a high island density $n$ of comparatively small islands. For higher temperatures, few large islands emerge due to the large diffusion length $l$ and a low island density $n$.

The average island size $N(T)$ is now inversely proportional to the square root of the island density $n$, and one finds:

$$\begin{aligned} N(T) &\sim n^{-1/2} \\ &\sim \left(\frac{c}{D_0}e^{E/kT}\right)^{-1/8} \end{aligned} \qquad \text{(IV.8)}$$

A schematic plot of $N(T)$ is shown in Fig.IV.2b).

As a remarkable result one finds that the dependence of average island size on temperature for the thermodynamic regime (Fig.IV.1b) and the kinetic regime (Fig.IV.2b) are of rather opposed character.

## IV.2 Evolution of average size

For the Monte Carlo simulations presented in this chapter the isotropic strain field as described in Appendix A has been used, since the anisotropic contributions to the surface strain seem of little importance in the context of size ordering. Indeed, on the highly anisotropic surface of $Si(001)$ very similar results for the size ordering have been obtained as compared to isotropic surfaces [Mo91, Bar92].

The strain energy is consequently calculated from the strain tensor components by II.9

$$E_{str} = \frac{\lambda}{2}(\varepsilon_{11}+\varepsilon_{22}+\varepsilon_{33})^2 + \mu(2(\varepsilon_{12}^2+\varepsilon_{23}^2+\varepsilon_{13}^2)+\varepsilon_{11}^2+\varepsilon_{22}^2+\varepsilon_{33}^2)$$

with elastic constants $\mu = 0.54 \cdot 10^{12}\text{erg/cm}^3$ and $\lambda = 0.32 \cdot 10^{12}\text{erg/cm}^3$.

Since dilute arrays of islands are considered, island-island interaction can be neglected. Hence, it is assumed that the strain field extends only five lattice constants away from the island boundaries to speed up computations. This implies a varying lower energy cut-off for islands of different size. However, due to the steep falloff of the strain energy with increasing distance from the island boundary, still about $85$ percent of the total energy are captured even for the largest islands.

All simulations have been performed on a 250x250 atomic sites lattice. As an initial step a coverage of $4\%$ was deposited randomly on the surface at a flux of 1Ml/s. Every $0.01$s a histogram of the island size distribution was recorded. Especially for higher temperatures the fluctuations in the size distributions are considerable. To reduce the noise, ten simulations with different initial conditions but the same set of parameters were used to calculate an average. The effect of averaging is displayed in Fig.IV.3, where the typical histograms of a single run and the averaged result over ten simulations at a temperature of $T = 725$K is shown.

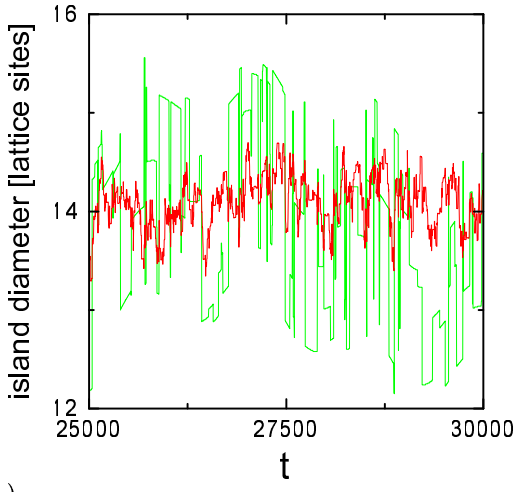


Fig. IV.3: Comparison between the temporal evolution of the average island size in a single system at temperature $T = 725$K (green) and an averaged result over ten realisations of the same system with same parameters in red.

To display the temporal evolution of the average island size, the average diameter $\langle\sqrt{N}\rangle$ of the islands was calculated from the histograms. Islands with a size below four atoms were not considered in the averaging. In Fig.IV.4 the simulation results for temperatures of $T = 675K \ldots 750K$ are displayed.

### IV.2.1 Kinetic results

From Fig.IV.4 it is evident that in the initial stages of island growth the size distribution is clearly kinetically controlled. At lower temperatures many small islands have formed whereas at higher temperatures fewer and larger islands emerge.

At lower temperature the nucleation of islands is the dominant process. Since the mobility of adatoms is low the density of single adatoms increases fast during the deposition and pairs of atoms are formed randomly.

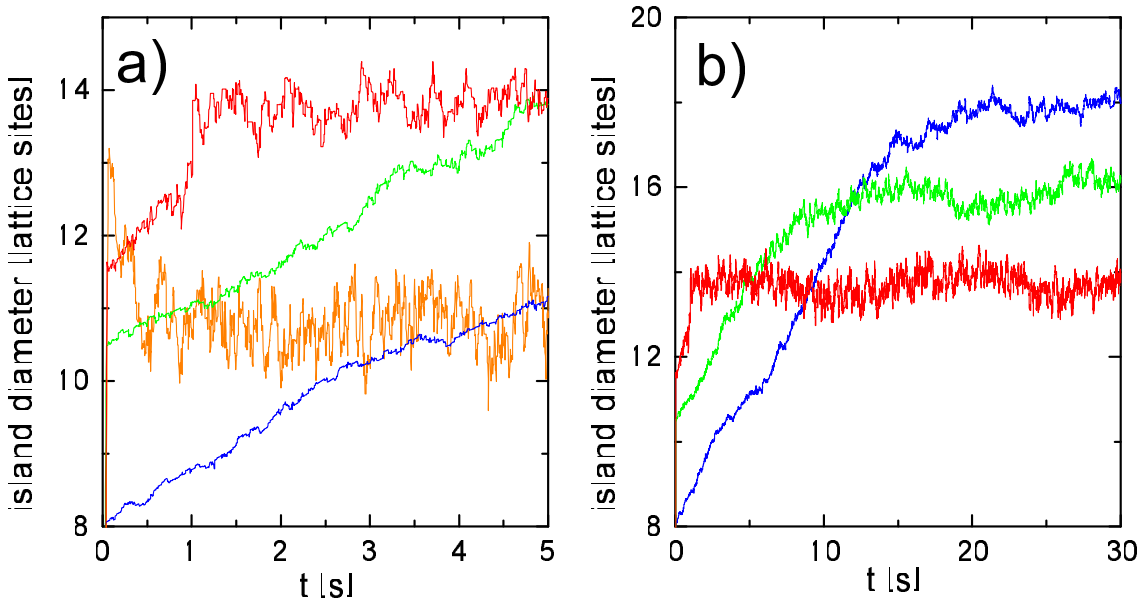


Fig. IV.4: a) Temporal evolution of the average island size for $T = 675$K (blue), $T = 700$K (green) and $T = 725K$ (red). Simulations have been performed on a 250x250 grid and averaged over ten runs with the same set of parameters. a) First five seconds of b) enlarged. Additionally, the temporal evolution of the average island size for $T = 750$K (orange) is shown in a).

Those act as nuclei for islands. Consequently, one observes many small islands for low temperatures.

With increasing temperature the adatoms become more and more mobile. A single adatom in a hot system can travel a long distance until it finds an existing island to which it will attach. The adatom density therefore decreases and nucleation of new islands is suppressed. The final spatial configuration in the kinetically controlled regime exhibits few and large islands.

### IV.2.2 Crossover

Would there be no elastic strain in the system the growth of islands would continue even beyond deposition, though at a reduced speed. The largest islands would capture most of the diffusing adatoms and grow on the expense of smaller islands until, eventually, only one single island is left in the system. One would, in other words, observe Ostwald ripening.

In the presence of strain the system behaves different from Ostwald ripening. On short time scales of a few seconds right after deposition (Fig.IV.4b) the islands do not grow by a considerable amount or even appear to have stopped growing. The scaling of the island size with temperature seems to be kinetically controlled, still.

An impatient experimentalist dealing with short time scales only might be led to the assumption that the average island sizes do not change perceptably in time and call the kinetically controlled state a stable configuration. This conclusion suggests itself especially for low temperatures since here the temporal evolution towards equilibrium becomes exponetially slow.

Right after the end of deposition, however,

the islands begin to equilibrate. The system is now in an intermediate state between kinetic island growth and thermodynamically controlled growth conditions. Characteristic for this regime is the slow increase of island sizes and a crossover of the average island size for systems of different temperatures.

During this intermediate state, elastic strain is of the essence since it drives the system towards equilibrium, though it is a comparatively slow process.

The strain destabilizes the island boundaries proportional to their size. Depending on the external parameters temperature and coverage, the strain sets an explicit upper limit to the increase in island size through Ostwald ripening.

Once an island has reached its critical size given by eq.IV.3 it stops growing. At this particular point the attachment rate of adatoms to the island driven by its size just equalizes the detachment rate generated by the boundary destabilization due to elastic strain. Since the equilibration process has to be conveyed by the kinetic effect of diffusive material transport, its effectiveness depends sensitively on temperature.

For low temperatures the growth process is the slowest and the higher the temperature becomes the faster the islands approach their average equilibrium size.

Once the equilibrium size distribution is reached, the average island diameter remains indeed constant as can be seen in Fig.IV.4b. In the course of equilibration the islands in the low temperature systems continue to grow until they reach their equilibrium size at an average diameter above that of the islands of the hotter systems, as is expected for islands grown under equilibrium conditions. Thus it comes to a crossover of size distributions that can be called a key feature of the equilibration process.

In [Sar92] the idea of crossover effects due to processes with different time scales is generalized. Here MBE-growth is described as a system of self-organized criticality. Growth processes are dominated by crossover effects accociated with different time scales or kinetic rates like Arrhenius hopping, deposition etc. The authors emphasize that the proposed concept of generic scale invariance is valid only asymptotically. Experiments on shorter time scales are very likely dominated by crossover effects as various kinetic rates are tuned as external parameters change.

### IV.2.3 Thermodynamic regime

Fig.IV.5 shows the histograms of the size distributions taken at a time $t = 35$s which is well beyond kinetics and inside the thermodynamically controlled regime. The solid curves are Gaussian fits to the data, omitting the tail of small islands.

Here, all the important features of thermodynamically controlled island growth can be recovered. For low temperatures, the size distribution has a well pronounced maximum. Mostly large islands are present and only very few individual adatoms or small groups can be found. With increasing temperature the size distribution broadens and the number of single adatoms increases due to the entropic contribution to the free energy. The maximum of the distribution shifts towards smaller islands. For the highest temperature $T = 750$K a distinct maximum of the size distribution is hardly visible and the tail of single adatoms and polymers becomes dominant. For even higher temperatures the maximum of large islands disappears and only single atoms or small groups can be found.

For the highest temperature $T = 750$K, equilibration is very fast and the equilibrium size distribution is reached almost directly after the end of deposition. Looking on a shorter time scale (Fig.IV.4b), one notices that for this particularly high temperature the average is-

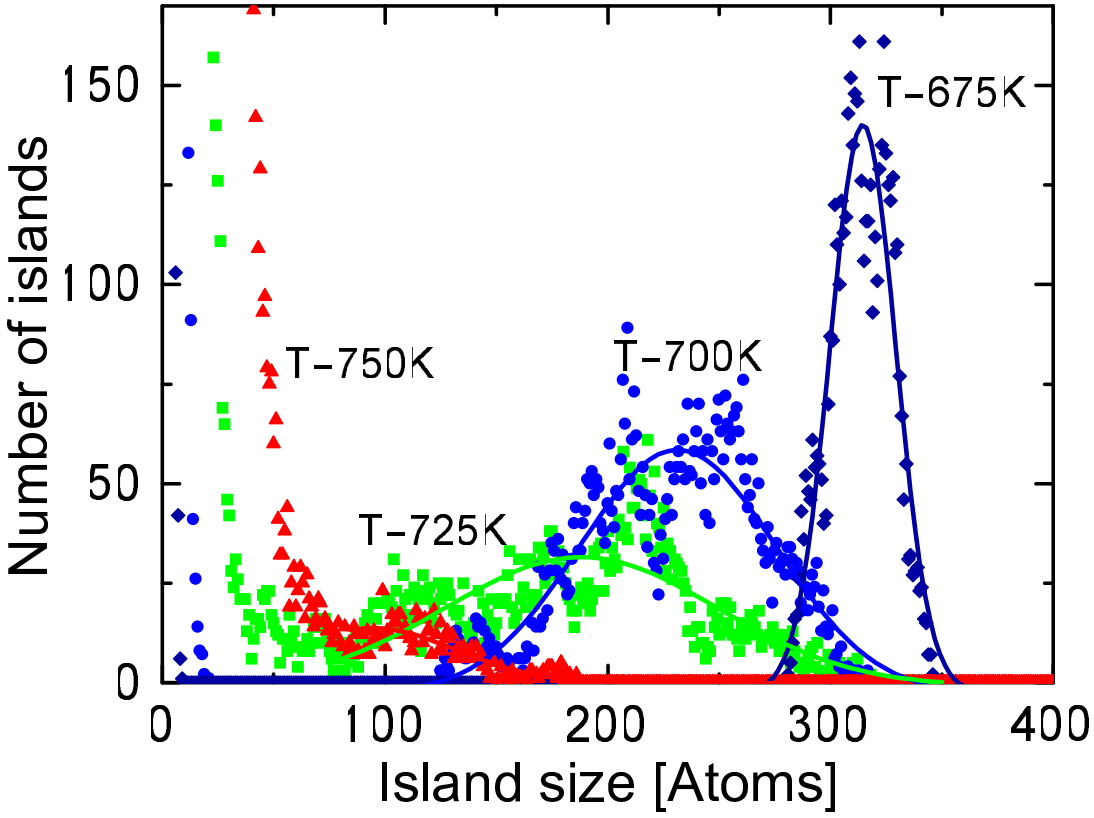


Fig. IV.5: Equilibrium size distributions for temperatures $T = 675$K (diamonds), $T = 700$K (circles), $T = 725$K (squares) and $T = 750$K (triangles) taken at $t = 35s$. The solid lines are numerical fits to the data. The tail of single atoms and small islands has not been included into the fit. The simulations have been averaged over ten different realisations to reduce noise.

land size is indeed larger in the kinetically controlled regime and islands have to shrink to reach their equilibrium size distribution. This effect might be caused by oversaturation where the attachment of adatoms to existing islands is strongly favored as opposed to nucleation of new islands. Only if enough island nuclei have been generated the excess atoms of large islands can be drawn off. Here, it seems important to note that the size limiting effect of elastic strain that should prevent islands from becoming too large, is a comparatively slow process and can to some extent be overcome by fast aggregation of adatoms at higher temperatures.

As an important conclusion from this observation one can expect that there exists a distinct temperature at which the equilibrium distribution is approached immediately.

### IV.2.4 Various simulation models in the kinetic regime

To elucidate the influence of various simulation models on the evolution of the average island sizes in the kinetically controlled regime, Monte Carlo simulations in the time during deposition and shortly after have

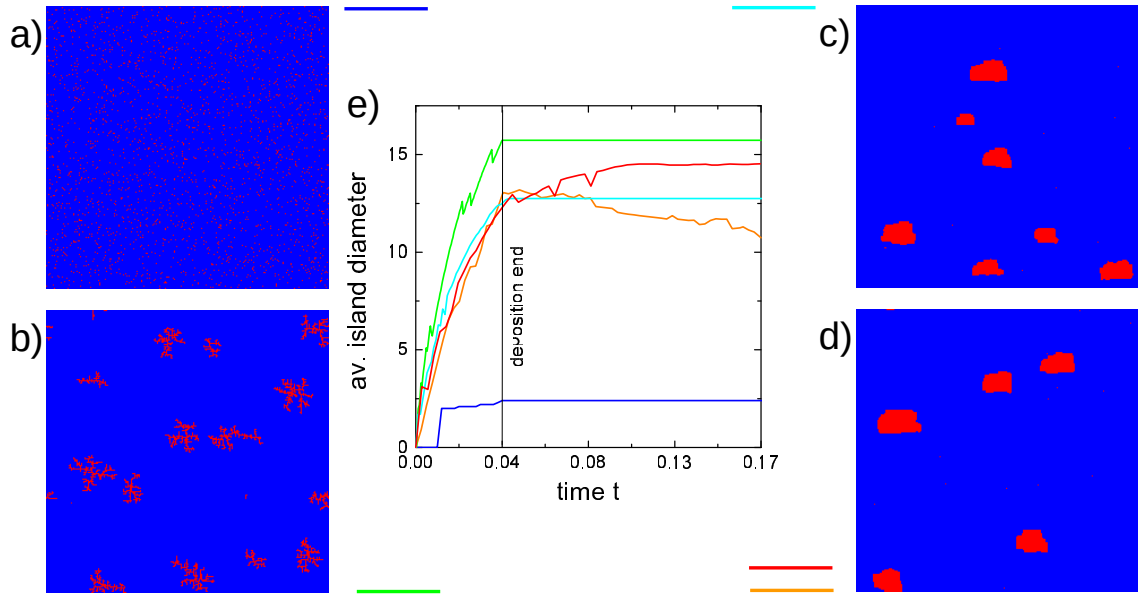


Fig. IV.6: The evolution of average island sizes and corresponding spatial island distributions (a) to d)) during deposition for various simulation models is shown in e). In a) (blue line) only deposition is considered. Diffusion and strain effects are neglected. b) shows simulation results for a model including diffusion (green line). Atoms are assumed to be immobile after attachment to an island. c) (cyan line) depicts a model with complete diffusion, but atoms cannot disconnect from islands. In d) (red line) full diffuson with attachment and detachment processes is used. The orange line shows the equivalent island size evolution with an additional strain field around islands. (Coverage $c = 4\%$, Flux $f = 1$Ml/s, Temperature $T = 750$K, Simulation time in a) to d): $0.17$s).

been performed using different levels of model complexity.

The simplest model possible consists of random deposition of adatoms only. Diffusion is excluded as well as elastic strain. The spatial distribution of adatoms depicted in Fig.IV.6a) shows a noise-like pattern. Islands can only form by accidental deposition of adatoms at adjacent places. Since only islands consisting of at least four atoms are counted as islands, for about $0.02$s no islands are detected at all. Then the average island diameter increases very slowly until the end of deposition (blue line in Fig.IV.6e). Due to the absence of diffusion the end of deposition also marks the end of the temporal evolution of island sizes.

As a next step one might now include surface diffusion. The islands in Fig.IV.6b) are obtained by allowing for diffusive steps for single adatoms which become immobile as soon as they attach to another adatom. This simulation scheme generates fractal islands which grow very fast due to their comparatively large perimeter (green line). Since atoms cannot move after attachment the end of deposition also stops island growth.

In the simulation model used for Fig.IV.6c) diffusion along island edges is allowed. Adatoms can, however, not detach from islands. The islands formed now are of compact shape and compared to the fractal islands have a smaller perimeter. Consequently more islands nucleate and the average diameter is reduced (cyan line).

If one now additionally allows atoms to detach from islands no prominent difference in

spatial island distribution or average island diameter can be observed during the time of deposition (Fig.IV.6d) and red line). But now the end of deposition no longer sets an end to island growth and the average island diameter increases still at times beyond deposition end. This efect can be understood as Ostwald ripening.

The orange line in Fig.IV.6e) shows the temporal evolution of the average island diameter for the complete growth model including strain, as it has been used in the previous sections. Again, during deposition the evolution of island sizes does not differ from the ones generated by models c) and d).Since the parameters for the simulation are chosen as in the Monte Carlo simulations in the previous sections, with the end of deposition the islands have reached an average size above their thermodynamically favoured one.

Though the spatial distribution of islands is indistinguishable from the simulation results in d), the strain drives the system away from pure Ostwald ripening. Instead the islands are reduced in size by the nucleation of new ones. These freshly nucleated isalnds grow cooperatively with the larger islands until equilibrium is reached.In the above example this equilibration process is by an order of magnitude slower compared to the kinetic effect of deposition and takes about one second of time to reach equilibrium.

Note that this effect would not be visible for a significantly slower deposition rate since the destabilizing effect of strain on island boundaries is always present and can only be overcome by the introduction by a much shorter time scale of kinetically driven island growth by using a high flux of material to the surface.

### IV.2.5 Comparison of simulation and thermodynamic equilibrium theory

By means of eq.(IV.3) one can calculate the temperature dependence of the average island size in equilibrium and compare to the results of the kinetic MC simulation (Fig.IV.5). With $c_1 = 0.3$eV and $c_2 = 0.107$eV one finds an optimum island size for $T = 0$K: $N_0 = 2000$. With increasing temperature the optimum island size shrinks almost linearly and suggests a critical temperature at $T_c = 775$K, where an optimum island size ceases to exist. The average island sizes extracted from the Gaussian fit to the kinetic MC results in Fig.IV.5 are in good quantitative agreement with this predicted thermodynamic behavior. Beyond $750$K the definition of a preferred island size by means of numerical analysis is indeed almos impossible.

Furthermore we can extract the dispersion of the average island size as the width of the size distribution (Fig.IV.7). The thermodynamic theory predicts an almost constant dispersion that increases significantly only close to the critical temperature $T_c$. In fact, in our kinetic MC simulations, which are close to $T_c$, a distinct increase of the size dispersion can be observed, albeit within a large error bar.

To investigate the temperature dependence of the size dispersion in a larger temperature range, where the MC kinetics becomes extremely slow, substantially higher computational efforts would be needed.

## IV.3 Conclusion

In conclusion, it has been shown by means of a Monte Carlo simulation that right after the deposition the island size distribution is kinetically controlled. For low temperatures one observes many small islands while islands become larger for higher temperature systems.

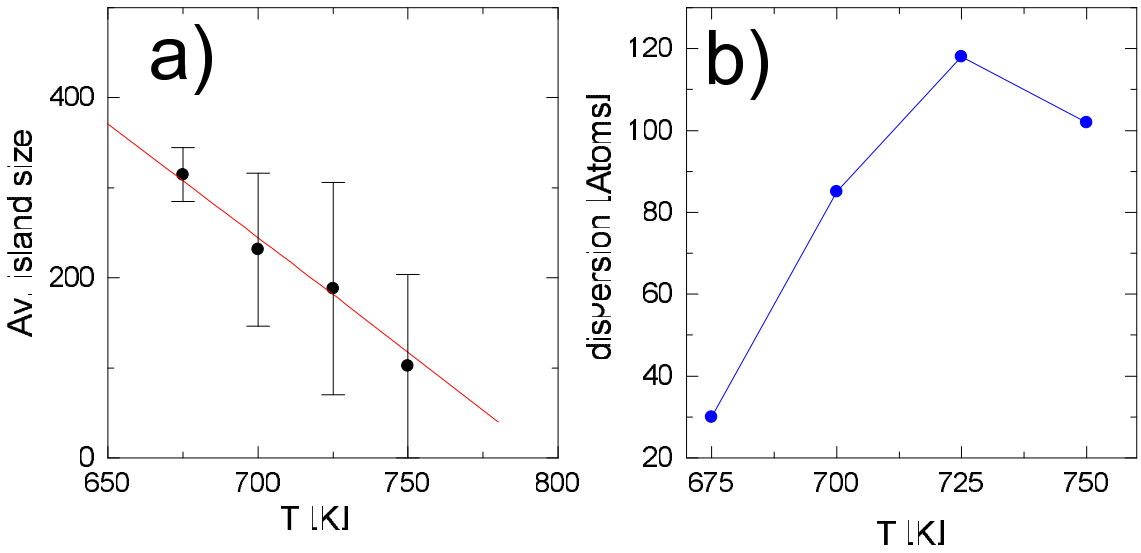


Fig. IV.7: a) shows the dependence of average island size on temperature. The theoretical prediction (red line) and the numerical results (circles) are plotted. Error bars are taken from the gaussian fits to the size distributions in Fig.IV.5 as FWHM/2, which is plotted in b).

During equilibration a crossover takes place where the islands in hot systems approach their equilibrium distribution faster than the islands in cold systems. Here the islands continue to grow until they reach their equilibrium size that exceeds the size of the hot system islands. The size distribution now is in agreement with thermodynamic equilibrium.

For the equilibrium regime it has been shown that the presented numerical Monte Carlo results are in good agreement with the thermodynamical findings as far as the optimal size distribution at equilibrium is concerned.

Similar work has been done on the dependence of the size distribution on strain [Rat94b], limited, however, to near equilibrium systems and a spatially non extended strain field.

# V.

# Elastic Anisotropy

As has been shown in Chap.III and Chap.IV, strain gives rise to self-limited growth of island sizes and spatial ordering processes. Though strain is quite effective in limiting the spatial extension of islands and generates narrow size distributions in reasonable amounts of time, the spatial arrangement of islands induced by isotropic strain is not as easily obtained.

It will be shown in this chapter how anisotropic contributions to the elastic strain fields generated by epitaxially grown islands can enhance the formation of spatially correlated island distribution.

The results obtained numerically by Monte Carlo simulation will be compared to experimantal findings gained by liquid phase epitaxy (LPE) experiments of $Si_{1-x}Ge_x$ on $Si(001)$ done by M. Schmidbauer et.al. [Sch98b]. Good agreement between experimental data and simulations is found [Mei01b].

## V.1 Introduction

It has been argued in the previous chapter that, compared to kinetic effects, the transition from a given spatial distribution of islands towards the equilibrium state is slow. This is even more true if the focus is not on size ordering but rather on spatial arrangement of the islands. Depending on initial conditions generated by 'unordered' kinetic effects as random deposition and surface diffusion, it might necessitate a considerable amount of material transport to reach the energetically most favourable systems state.

In any case self-organisation processes that lead to either size ordering or spatial correlation of islands do rely on an interplay between kinetic effects which are intertwined with material transport, and the strain field that 'defines' equilibrium by introducing long range interactions.

Though most of the early theoretical work on spatially correlated growth of quantum dots is based on energy considerations, the influence of kinetic effects during growth has turned out to be crucial. Recent studies have shown, for example, that a kinetic energy barrier for growth on island facets can lead to self-limiting growth [Jes98, Käs99] where quantum dots with a surface facetted in certain directions are particualrly stable and hence do not grow fast assuming a surface with a different orientation. Those kinetic limitations play a central role for a detailed understanding of island growth and they strongly depend on growth conditions.

The aim of this chapter is to improve the understanding of self-organized quantum dot growth by compairing experimental results obtained in LPE grown $Si_{0.75}Ge_{0.25}/Si$ islands with kinetic Monte Carlo simulations. In particular it will be shown that the interaction

of an anisotropic strain field with kinetic diffusion processes might promote the effect of spatial ordering by defining not only preferred distances, as isotropic strain does, but additionally introducing preferred directions so that spatial correlation of islands is more readily obtained.

## V.2 Theory

### V.2.1 Close to equilibrium Monte Carlo

To obtain Monte Carlo simulation results that are comparable to experimental findings two points are of particular importance. First, the anisotropy of the $SiGe$-compound has to be considered in the calculation of strain fields and secondly simulations have to be performed as close to equilibrium as possible.

Generally the second part can be tackled by choosing a low deposition rate of $0.01$ monolayers per second at reasonably high temperatures[1]. Thus it is ensured that single adatoms have a long mean free path in comparison to typical island sizes, and island nucleation takes place at energetically favorable positions rather than by accidental dimer formation caused by a large numer of diffusing adatoms.

A sufficiently long mean free path of diffusing atoms is most important as far as the compatibility of experiment and simulation is concerned since the Monte Carlo simulation is not designed to handle dissolution of atoms from the substrate as an additional way of material transport. In LPE, on the other hand, the transport through the melt is a very efficient way of moving atoms around as compared to pure surface diffusion.

Fortunately, the emerging structures in equilibrium systems do not depend on the particular transport mechanism which led the system to equilibrium.

Ihe inclusion of anisotropic strain can easily be done by using the Green's function approach to strain calculation discussed at length in Appendix B. Here, the elastic displacements $u_i$ are calculated by means of the elastic Green's tensor of elasticity theory $G_{ij}(r,r')$

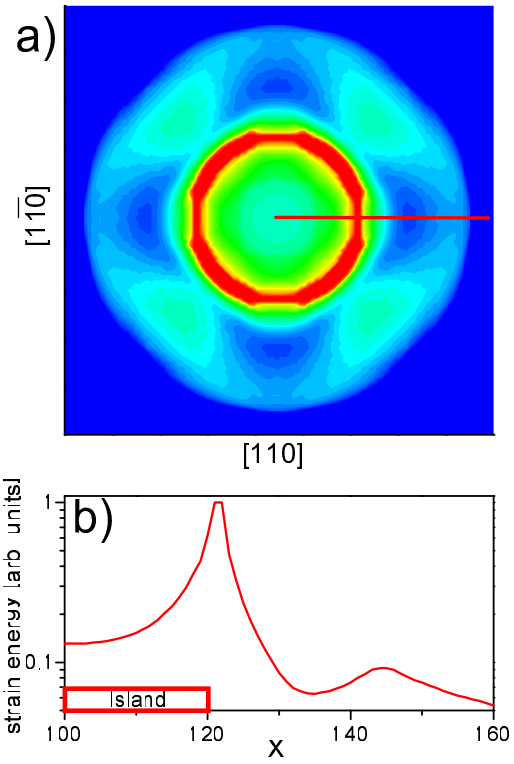


Fig. V.1: Contour plot of the anisotropic strain energy of a circular island in the $\{001\}$-plane for the system $Si_{0.75}Ge_{0.25}/Si$ with elastic moduli $c_{11} = 1.58 \cdot 10^{12}$erg/cm$^3$, $c_{12} = 0.60 \cdot 10^{12}$erg/cm$^3$ and $c_{44} = 0.77 \cdot 10^{12}$erg/cm$^3$. b) shows the strain profile for a cut along the red line in a).

$$u_i(r) = -\oint_S d^2r' G_{ij}(r,r') P_j(r') \qquad \text{(V.1)}$$

The integration is carried out along all island boundaries where the line forces $P_j$ act as the sources of the strain. The strain field $\varepsilon_{ij}$

1. Of course, the effect of temperature is closely related to the surface binding energy. For the simulations presented in the following, surface and nearest neighbor bonds are $E_s = 1.3$eV and $E_b = 0.3$eV, respectively. With those parameters reasonably high temperatures should not be lower than $650$K.

itself is then given by the partial derivatives of the displacements

$$\varepsilon_{ij} = \frac{1}{2}\left(\frac{\partial u_i}{\partial x_j} + \frac{\partial u_j}{\partial x_i}\right) \quad \text{(V.2)}$$

Since the Green's tensor contains the elastic constants of the considered material the elastic anisotropy is fully taken into account.

Finally, to calculate the modification of the diffusion barriers caused by the strain, the local elastic strain energies are evaluated by

$$E_{str} = \frac{c_{11}}{2}\left(\varepsilon_{11}^2 + \varepsilon_{22}^2\right) + \\ + c_{12}\varepsilon_{11}\varepsilon_{22} + 2c_{44}\varepsilon_{12}^2 \quad \text{(V.3)}$$

where $c_{11}$, $c_{12}$ and $c_{44}$ are the elastic constants of a cubic crystal in Voigt notation. In the inset of Fig.V.1 a strain energy profile of a step is shown. The quadratic decay of the elastic energy with increasing distance from the step is in agreement with theoretical predictions.

For the system $Si_{0.75}Ge_{0.25}/Si$ the elastic constants of the binary compound have been calculated in linear approximation from the bulk values of $Si$ and $Ge$. The numerical values are shown in Table V.1.

The nearest neighbors for group IV semiconductors are in the $[111]$-direction. Consequently this is the elastically hard direction whereas the $[001]$-direction is elastically soft, as can be seen in Fig.V.1.

### V.2.2 Liquid phase epitaxy

In contrast to isotropic strain, where spatial ordering has only be obtained for a very narrow parameter window after long equilibration times (see Chap.IV), in the system presented below anisotropic strain allows for spatial ordering for a comparatively huge parameter window making this method of growing ordered arrays of islands less feeble towards changes of external parameters during the growth process.

It should be noted, however, that the spatially ordered state is still a state close to equilibrium which is thus only reached under suitable conditions and after an appropriate (and usually long) period of time.

Hence, the experimental results have been obtained by means of LPE of $SiGe/Si(001)$, where for sufficiently high coverage a high degree of positional correlation has been observed.

As compared to well known growth techniques such as molecular beam epitaxy or metal organic chemical vapor deposition, LPE is carried out rather close to thermodynamic equilibrium[Bau85]. A metal melt (e.g. $Bi$ or $In$) containing e.g. $Si$ and/or $Ge$ is put onto a $Si$ substrate and cooled down such that epitaxial growth occurs via oversaturation of the melt. A more detailed description of the growth procedurecan be found in [Sch98b]. As a consequence of conditions close to equilibrium, highly regular, facetted, coherent $Si_{1-x}Ge_x$ truncated pyramids with a narrow size distribution are grown on $Si(001)$.

For this material system it has been shown that the island size is independent of the growth rate and growth temperature but is given by a simple scaling behavior between the island base width and the $Ge$ concentration, which corresponds to the lattice mismatch. By varying layer composition and thus the elastic strain island sizes can be adjusted from $nm$- to $\mu m$-range[Dor98b].

By adapting the Monte Carlo method described in the previous chapters to the close-to-equilibrium growth conditions of LPE an explanation of the emergence of ordered island chains can be given in terms of an interplay of kinetic effects and the anisotropic strain fields generated by the islands on the $Si(001)$ surface.

At this point it has to be noted that a direct kinetic Monte Carlo growth simulation is not yet feasible in case of liquid phase epi-

| | $c_{11}$ [$10^{11}$erg/cm$^3$] | $c_{12}$ [$10^{11}$erg/cm$^3$] | $c_{44}$ [$10^{11}$erg/cm$^3$] |
|---|---|---|---|
| $Si$ | 16.57 | 6.39 | 7.96 |
| $Ge$ | 12.89 | 4.83 | 6.71 |
| $Si_{0.75}Ge_{0.25}$ | 15.79 | 6.00 | 7.65 |

Table V.1: Elastic constants for $Si$ and $Ge$ in Voigt notation [Hel82]. The elastic constants for the compound $Si_{0.75}Ge_{0.25}$ are obtained in linear approximation from the bulk values of $Si$ and $Ge$.

taxy. Even for the comparatively simple case of molecualr beam epitaxy a Monte Carlo simulation cannot treat the three dimensional growth of arrays of fully developed islands.

However, with appropriately chosen growth parameters and a self-consistently included strain field, a kinetic Monte Carlo routine can simulate the initial stages of epitaxial growth processes close to equilibrium conditions until platelets of islands arise[Sch98d, Bos99a, Pri95].

In Chap.IV it has been shown that for sufficiently long simulation times from an initial, kinetically controlled regime thermodynamically limited close-to-equilibrium conditions can be reached. Therefore it is appropriate to compare LPE experiments to Monte Carlo simulations performed with an anisotropic strain field using the elastic constants of $Si$ and $Ge$.

## V.3 Experimental and numerical results

In LPE experiments [Sch98b] the formation of island polymers that is groups of two or more islands equidistantly arranged along a line in the $\langle 100 \rangle$ direction, can be observed for low coverages (Fig.V.2b), evolving into extended island chains for increasing coverages (Fig.V.3b). This obviously implies an anisotropic (inhomogeneous) probability of island formation around an already existing island.

Performing Monte Carlo simulations considering anisotropic strain and considering restrictions with respect to thermodynamic equilibrium, linearly ordered chains of islands can be found in a temperature regime of $620$K to $700$K. For low and high coverages of 5% (Fig.V.2a) and 20% (Fig.V.3a), respectively, island distributions are found that agree well with LPE experiments. The presented simulations have been performed on a $400 \times 400$ grid.

For a temperature window of $620$K to $700$K we find island chains oriented along $[100]$ that compare well to the experimental findings (Fig.V.2).

For low coverage most chains consist of two islands but island polymers containing three or four islands can be found as well. The orientation in the $[100]$- or $[010]$-direction is choosen at random.

Over the whole temperature regime, where polymers are found, the islands tend to have a preferred distance from each other while the distance between different chains is larger, exactly as observed in the LPE experiments. The centers of mass of two islands in a chain are on average fourteen lattice constants apart. The average island size for a temperature of $650$K is eight lattice constants in diameter. However, the average island size increases with temperature so that for temperatures beyond $700$K islands in the chains begin to cluster.

For very low temperatures the nucleation processes are dominated by random dimer formation and the self-organisation of island chains is largely suppressed. Furthermore, for

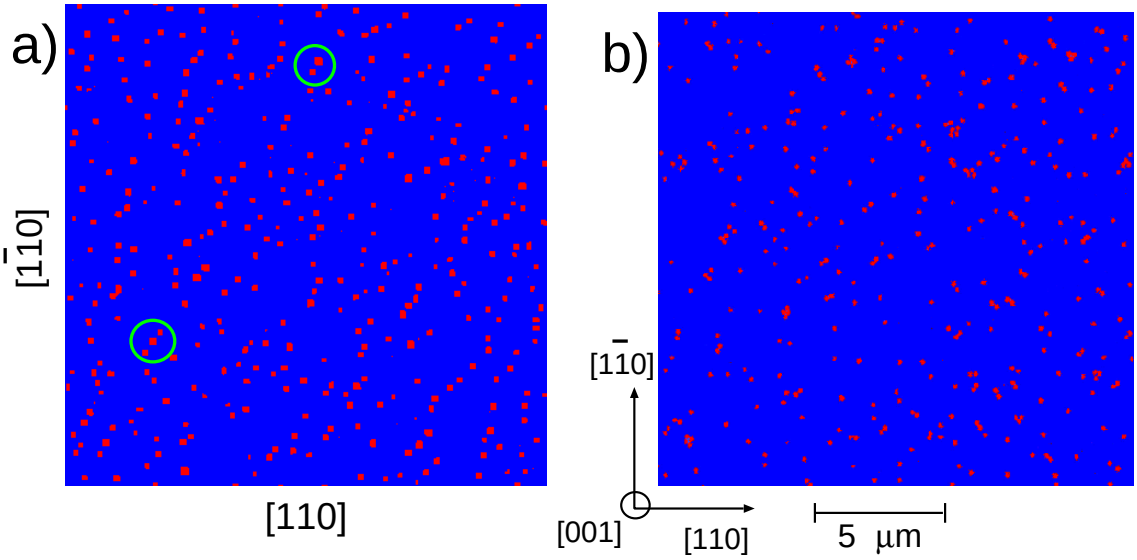


Fig. V.2: Results of the kinetic Monte Carlo simulation ($T = 650$K, growth rate $0.01$Ml/s, coverage $c = 0.05$, after $200$s growth interruption. A high percentage of islands is arranged in dimers and trimers along $\langle 100 \rangle$ (e.g. marked by circles). b) Atomic force micrographs picture of LPE grown $Si_{0.75}Ge_{0.25}/Si(001)$ islands at low coverage ($c = 0.02$) [Mei01b].

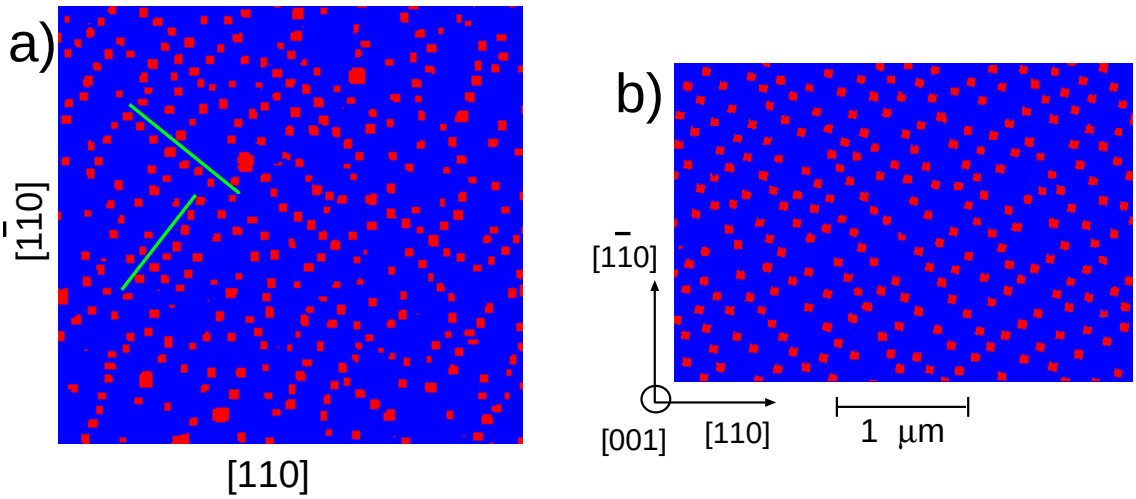


Fig. V.3: Same as Fig.V.2 for a coverage of $20\%$. a) Results of the kinetic Monte Carlo simulation for $T = 650$K, flux $F = 0.01$Ml/s after $200$s growth interruption. b) Linear island chains along $\langle 100 \rangle$ at a coverage of $c = 0.16$ (Scanning electron micrograph). Islands are arranged in extended chains in a preferred direction, as is marked with lines [Mei01b].

low temperatures the average island size is small resulting in comparatively weak strain fields. Since the spatial ordering is to the larger part conveyed by the strain, only little effects can be expected.

## V.4 Discussion

The emergence of ordered chains of islands in LPE at sufficiently high island densities have been attributed to an underlying ripple pattern due to a kinetic surface instability of the plane layer which is aligned along $\langle 100 \rangle$[Dor98a]. This effect was first observed by [Ale88], who found that for surface reconstructions with broken symmetry and an anisotropic strain field, the surface is unstable towards the formation of elastic stress domains. In the case of $Si(001)$ stipes are formed from steps of monoatomic height. This ripple pattern, at later stages of growth, transforms into three dimensional islands. The corresponding distances between islands are, therefore, determined by the wavelength of the underlying ripple pattern. Such a pattern is only observed for low $Ge$ content ($x < 0.15$). Positional correlation is observed, however, also in the case of an absent ripple pattern for $x > 0.15$.

Furthermore, the equidistant arrangement of islands as polymers or chains cannot be attributed to a ripple pattern alone. Instead, the positional correlation is significantly influenced by anisotropic strain effects.

Diffusion processes on strained surfaces lead in general to an enhanced mobility of the adatoms caused by the lower binding energy in the strained areas and, as a result, a net current of atoms from the strained regions to the unstrained ones can be observed. Applying these considerations to the material system at hand one would expect a higher island nucleation rate in the elastically hard directions ($\langle 110 \rangle$) as seen from the island since in those directions the strain decays more rapidly than in the soft directions ($\langle 100 \rangle$), where the strained region extends further away from the island boundary. On the other hand in the experiment as well as in the computer simulation the island chains are oriented along the soft direction which seems to disprove the above reasoning.

As can be seen in Fig.V.1 the elastic anisotropy of the $SiGe/Si$-system generates a monotonically decaying strain field in the soft $\langle 100 \rangle$-direction. In the elastically harder $\langle 110 \rangle$-direction the strain does at first indeed decay faster. There is, however, a local maximum of the strain some distance away from the island boundary that leads to an average flux of adatoms to the areas in the soft direction, where island nucleation is consequently enhanced.

For islands of a size of eight atoms in diameter the local strain maximum in the hard direction is ten lattice constants away from the island boundary. This value agrees well with an average island separation of fourteen lattice constants, as can be seen in Fig.V.4.

One further point calls for clarification. In the LPE experiments the nominal coverage of the surface is considerably lower than in the corresponding Monte Carlo simulations. Still, the experiment and the simulations seem to have yielded islands of the same size. Though the simulation does not treat diffusing kations and anions separately and is rather dealing with the diffusion of effective atoms, this simplification in the simulation routine cannot account for the surplus of material at the surface as it is observed in the experimental samples.

The additional material is rather added by exchange processes of the growing islands with the wetting layer. Such an active wetting layer has been observed experimentally in a transmission electron microscopy study by [Lia99]. Here, $Ge$ dots on $Si(001)$ relax strain

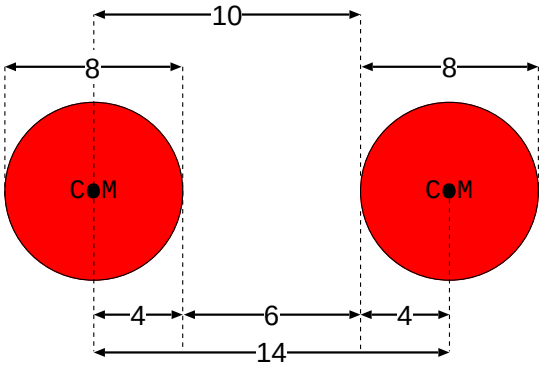


Fig. V.4: An island dimer in an equilibrium distance defined by anisotropic strain. All measures are taken in units of the lattice constant. Distances are measured from the center of mass (CoM) or the boundary of the island.

by an alloying process. Trenches are formed around the islands and the island/substrate interface moves towards the substrate. By this process, the island morphology changes considerably and in the LPE grown samples the islands appear larger than in the simulations, where an active wetting layer is not included.

## V.5 Conclusion

It has been shown that under the assumption of an anisotropic strain field calculated for the $SiGe/Si$-system the experimentally observed formation of island polymers along the elastically soft $\langle 100 \rangle$-direction can be explained. A local maximum of the strain field in the elastically hard direction provides a flux of adatoms to enhance island nucleation in the elastically soft directions.

Good agreement between experiment and numerical simulation has been found and a satisfactory understanding of the processes of the self-organized island chain formation during liquid phase epitaxy has been obtained by the kinetic Monte Carlo simulations presented above.

Even though this scheme was originally designed for the simulation of MBE growth it should be noted that under growth conditions close to thermodynamic equilibrium the large number of individual hopping events simulates well the exchange processes with the liquid phase.

# VI.

# Stacks of Quantum Dots

## VI.1 Introduction

For most electro-optical applications for quantum dot layers as active media it is generally most favorable to have access to as many dots as possible per unit area. All of these dots should be of about the same size to ensure similar electro-optical properties.

As has been shown in the previous chapters, the self-organized growth of quantum dots with a narrow size distribution is readily obtained by choosing appropriate growth conditions. All dots with the same size exhibit the same electronical structure and can thus be excited simultaneously with the same signal. To further improve response, one has to increase the filling factor which is defined as the area occupied by dots per unit area divided by the unit area. For purely two-dimensional island growth the filling factor is equivalent to the surface coverage. By increasing the filling factor the density of dots addressed with a signal is increased and thus device performance is enhanced [Bim96, Hei97, Max98].

To increase the density of quantum dots distributed randomly over the surface, they have to be grown in ordered patterns. Unfortunately, the ordering in spatial dimensions is not as easily obtained as a narrow size distribution. In Chap.III it has been shown that spatial ordering can only be observed for a comparatively tiny parameter window after long equilibration times. In contrast to size ordering, which can be readily obtained under kinetically controlled growth conditions (see Chap.IV), spatial ordering is induced by island-island interactions which are acting on an altogether different time scale. Hence, the approach of a spatially ordered, equilibrium state is time consuming at best. In systems, which allow low growth temperatures only, equilibrium might practically never be reached since reasonable equilibration times would have to be measured in weeks or even months.

In Chap.V a diversion has been presented by the introduction of anisotropic strain to obtain laterally correlated arrangements of islands if not much faster but at least for a considerably larger parameter window than for isotropic strain.

Anisotropy in the surface strain field can be observed, more or less pronounced, in all crystals. For appropriate systems it creates a directional variation in strain strong enough to enhance nucleation of islands in certain directions and to reduce nucleation in others. By this effect the path towards equilibrium is cut short. Nevertheless, equilibrium has still to be approached via long equilibration times.

Now there is evidence [Spr00] that ordered quantum dot layers can be grown without necessitating time consuming equilibration processes. A clever method obtains spatial order-

ing by depositing a larger number of quantum dot layers on top of each other with thin buffer layers of substrate material in between.

For those quantum dot stacks spatial ordering is increasing in parallel with the number of deposited layers. Here, the spatial correlation emerges in a system with no or only short periods of equilibration, the kinetic processes of deposition and diffusion being the only relevant transport mechanisms. Not only the spatial arrangement is enhanced. It has been shown in [Ter96, Spr98, Liu99b, Pin99] that apart from the spatial arrangement also the uniformity of size, shape and spacing of the dots can be improved by growing quantum dot superlattices.

The strain field at the surface generated by the buried layers of quantum dots is held responsible for the spatial ordering effect [Xie94]. In the following, Monte Carlo simulations will be presented which aim at the growth of self-organized quantum dot stacks. The important difference to the previous chapters is basically the extension of the self-consistently calculated strain field into the third dimension – which is the direction of growth – so that the strain generated by the buried layers can induce spatial correlations between islands at the surface.

## VI.2 Theory

### VI.2.1 Experimental footing

The emergence of ordering effects in quantum dot stacks has been observed experimentally by cross-sectional scanning electron microscopy studies[Xie95c, Eis99] or photoluminescence spectroscopy[Hei97, Hei98]. Novel electronic devices can be produced by using very thin spacer layers [Mil99]. Vertically correlated quantum dot layer grown by this method exhibit a strong electronic coupling with unique properties [Fle99, Hei98] and the resulting structure is referred to as a quantum dot superlattice [Xie95c, Sol96, Bar97b, Sch98a, Hei97].

Vertical alignment of quantum dots has been observed experimentally in various material systems. In [Xie95c, Sol96] evidence for vertically aligned columns of quantum dots in $InAs/GaAs$ superlattices is given and in [Sch98a] the growth of $SiGe/Si$ superlattices is reported. Vertical quantum dot superlattices of $PbSe$ have also been grown on $Pb_{1-x}Eu_xTe$ [Spr00]. Here, lateral and vertical correlations can be tuned by variation of spacer layer thickness. Furthermore, a different evolution of dot sizes and shapes is observed for different spacer layer thicknesses [Xie95a].

#### *VI.2.1.a Correlation*

Experimental results on the influence of strain on vertical correlations can be found in [Xie95c]. For thin buffer layers correlated growth can be observed. In Fig.VI.1a the qualitative behavior of the pairing probability in dependence of the spacer layer thickness as presented in [Xie95c] is given. The pairing probability is defined as the fraction of dots in the surface layer which have nucleated directly above another dot in the buried layer beneath. For thin spacer layers the pairing probability is high and the dots are correlated. With increasing buffer layer thickness the correlation effect decays and beyond 100 monolayers uncorrelated growth with a pairing probability of $0.5$ is observed.

#### *VI.2.1.b Anti-correlation*

The problem of how strain influences the equilibrium properties of stacked quantum dots has been treated theoretically by [Shc98b].

This work also tries to explain the experimentally observed effect of anticorrelation.

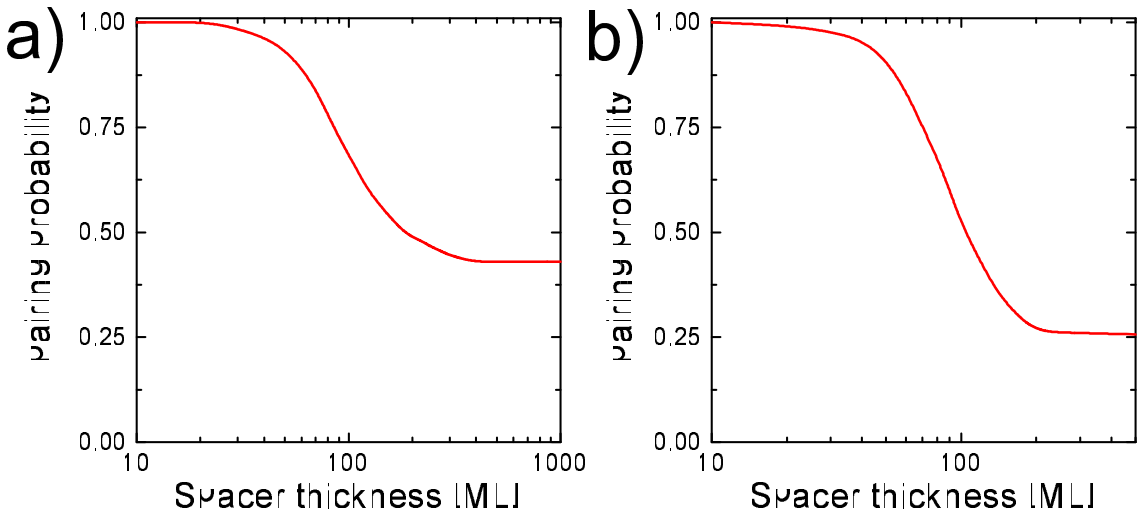


Fig. VI.1: a) Schematic dependence of the pairing probability $P_p$ on spacer thickness in monolayers after [Xie95c] and b) transition from correlation to anticorrelation of $P_p$ after [Shc98b].

Here quantum dots in different layers do not grow on top of each other (correlated) but rather on positions most distant from the dot positions in the buried layer (anticorrelated).

It should be noted that anti-correlated growth can occur in more complex stacking sequences as well. In [Spr98] a triagonal dot lattices with $fcc$-stacking can be obtained by simulations for $IV$-$VI$ superlattices.

The qualitative pairing probability function after [Shc98b] in dependence of buffer layer thickness is shown in Fig.VI.1b. For thin spacers the dots grow in a correlated way with a pairing probability of above $50\%$. For increasing buffer layer thickness the pairing probability drops below $50\%$ indicating anticorrelated growth.

### VI.2.2 Numerical modelling

#### *VI.2.2.a Simulated quantum dot stacks*

The simulation routine is based on the Monte Carlo code presented in the previous chapters. To extend the calculation of the strain field into three dimensions the isotropic strain ansatz in Appendix A is used.

The simulation scheme goes well beyond the simulations of [Ter96], where the growth of quantum dot superlattices was simulated and vertical alignment was observed that lead to progressively increasing island sizes and spatial ordering. In contrast to the routine applied here, the results were obtained from simple strain calculations treating the buried islands as point like strain sources and a nucleation model that places islands at strain energy minima but did not include diffusion processes.

Nevertheless, the limitation to buried point sources of strain gives results, which compare well with experimental findings. In [Hol99] various alignment patterns for superlattices of quantum dots can be explained by assuming anisotropic strain to model the elastic islans-island interactions. Different material systems have been elucidated in this paper.

The schematic procedure for a numerical growth simulation of a quantum dot stack used in this work is depicted in Fig.VI.2. The growth of the first layer starts with a per-

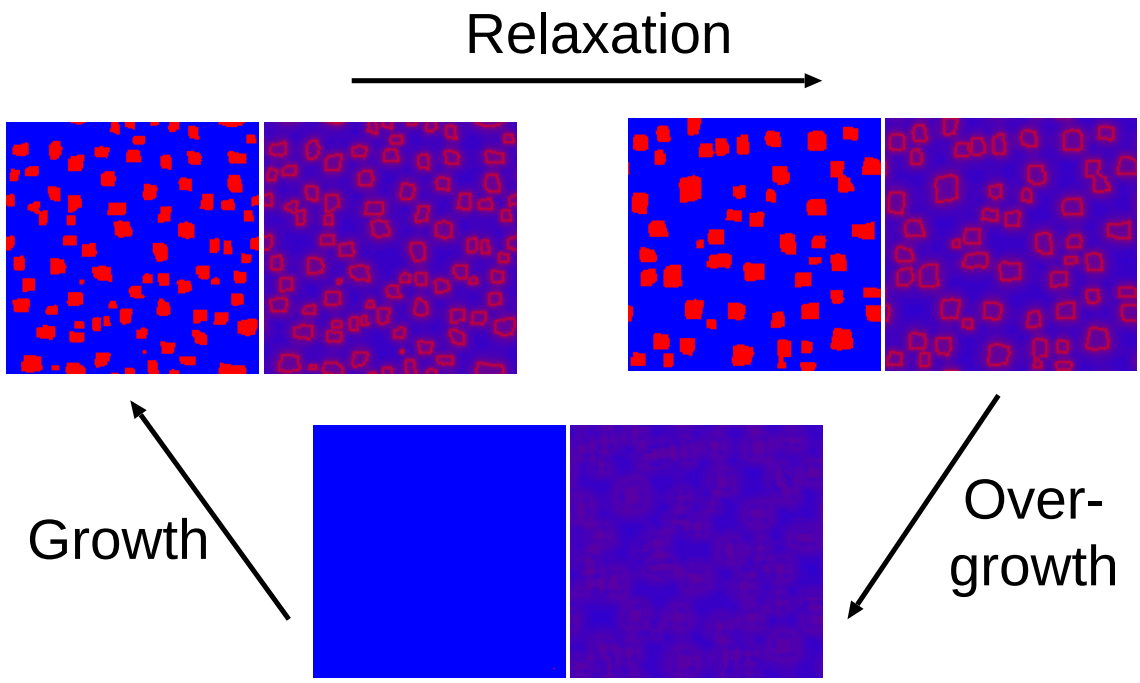


Fig. VI.2: Algorithm for simulating the growth of quantum dot stacks. Growth begins with deposition (Growth) of material on a plain surface (a). After deposition (b) the system relaxes (Relaxation(c)) and is subsequently overgrown with substrate material (Overgrowth) and the cycle is closed.

fect surface with a locally homogeneous strain field (a). Then material is deposited and in the course of growth islands form in a self-organized way and induce strain in the substrate (b). After the end of deposition the ensemble is allowed to equilibrate (c) before the islands are buried beneath a buffer layer of variable thickness.

The process of capping the islands with substrate material freezes the strain field and all diffusion processes are stopped. After the process of capping the surface is again assumed to be flat but now the buried islands generate a non-homogeneous strain field along the substrate surface. The actual strength of strain is calculated self-consistently from elasticity theory with the buried islands as the sources of strain. It depends in amplitude and shape on the thickness of the spacer layer (d). Then another deposition process is started and a new layer of islands grows, now subjected to two sources of strain, the buried islands and the islands on the surface layer.

Of course, the strain at the surface of a stack of quantum dots is not only determined by the topmost buried layer but all the buried layers contribute to the surface strain, albeit with decreasing relevance with increasing distance from the surface. For all presented simulations in the following, the strain induced by the top five layers has been considered for the surface strain calculation.

However, for very thin spacer layers of, say, five monolayers the lowest considered layer is separated by only 25 lattice constants from the surface. The following few layers down to a distance of about 50 lattice constants are still in a distance where interaction with the growing surface layer could be expected, since in [Spr00] it has been shown that variations in

strain energy by the order of 1meV might be sufficient to induce ordering effects.

It is, however, assumed that the upper buried layers have a much stronger impact on island growth by exerting much higher strain so that minor contributions from lower layers to the total strain can be neglected.

This assumption is supported by [Dar99a], where molecular dynamics simulations are used to dertermine the stress distribution in an ordered quantum dot superlattice. It is found that embedded islands generate a stress field at the surface, which is in good agreement with analytical expressons based on point like force dipoles. Consequently, the stress field decays rapidly and only the topmost buried layers are of importance.

#### *VI.2.2.b Simplifications of the growth model*

Some important differences between the model used for simulating the growth of quantum dot stacks and the actual growth processes have to be mentioned.

In the simulation the buffer layer surface defines the surface for growth of new islands. In reality before the emergence of quantum dots a wetting layer would form coherently upon the substrate. Thus the buffer layer thickness used in the simulation is a relative value describing the added thicknesses of spacer and wetting layer.

The missing wetting layer also gives rise to another important difference between model and experiment. For very thin buffer layers the quantum dots are not fully covered by substrate material and in the further growth process material from the half-buried dots is transferred to the substrate surface to contribute to the wetting layer. This form of interaction between buried layer and surface is not possible in the simulation since three dimensional growth of dots is not considered and only two dimensional monolayer islands are used to mimic the buried quantum dots beneath the buffer layer.

Additionally, in the growth simulation an increase in nucleation rate at certain places is conveyed by a locally modulated diffusion constant due to surface strain alone. However, the interplay between buried dots and the substrate-to-wetting-layer interface leads in general to dislocations and surface defects above buried dots for sufficiently thin spacer layers. These strain induced surface discontinuities increase the probability for island nucleation at these places, and hence an enhanced correlation in vertical alignment can be expected in experiments.

Even for thick spacer layers the model clearly deviates from the natural growth process, since no simulation of three dimensional island growth is performed and structural changes in the shape and size of quantum dots during the process of overgrowth are not considered. Shape transitions between surface dots and dots embedded in the bulk are a common phenomenon and caused by differences in the way of strain relaxation which imply different geometries for the lowest energy state for free and embedded dots.

A change in the induced surface strain is connected, of course, with a change in the dot shape . This effect cannot be taken into account by the simulation model. It is, however, assumed that the main contribution to the surface strain field does not originate from morphological details but is rather given by the position and lateral size of the islands. These quantities can be handled well by the numerical algorithm and a sufficient generality of the simulation results with respect to experimentally observed growth processes can be expected.

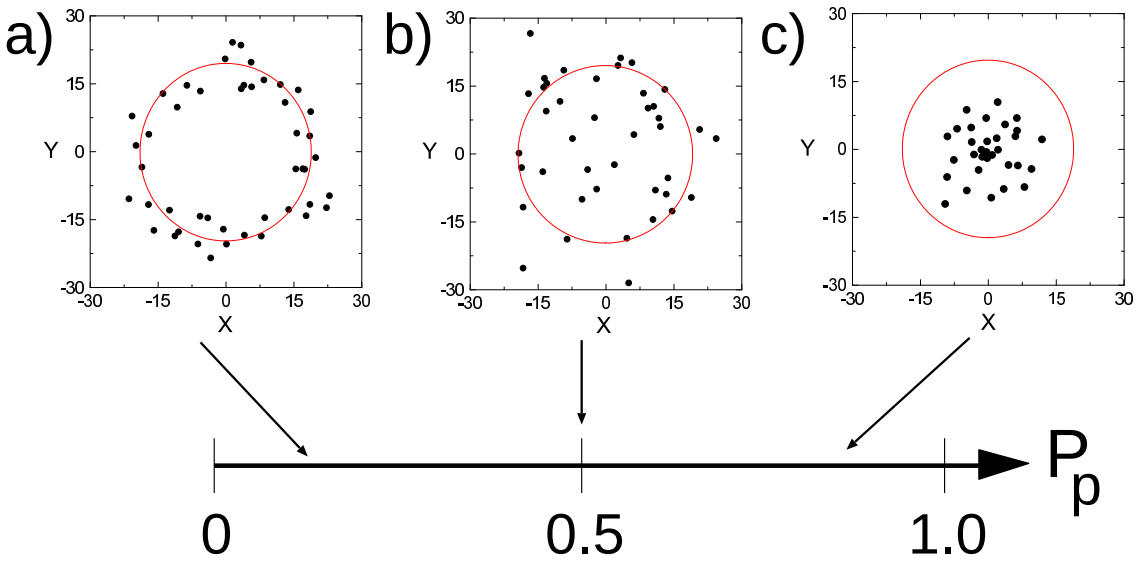


Fig. VI.3: Nearest neighbor distribution from surface layer to the topmost buried layer for a) anticorrelated, b) uncorrelated and c) correlated growth. The corresponding values of the pairing probability $P_p$ is indicated with arrows. Red circles in distance distributions denote the average distance of islands in the growing layer. ($T = 700$K, $f = 0.02$Ml/s, $c = 35\%$, spacer thickness a) 40Ml, b) 25Ml and c) 5Ml)

### *VI.2.2.c Pairing propability*

A good measure for correlated or anticorrelated growth in stacked quantum dot layers is the pairing probability, which indicates the ratio of islands that have grown directly above another island. A pairing probability of '1' denotes perfect correlation and the value '0' is associated with fully anticorrelated growth. If the stack of quantum dots is growing uncorrelated, the pairing probability is equal to 0.5.

To characterize the growth mode, the simulation routine calculates a quantity equivalent to the pairing probability each time before overgrowing a completed layer of islands. To this end the centers of mass of the surface islands and of the islands of the topmost buried layer are determined. Then, for each surface island the distance to the lateral position of the nearest island in the buried layer $d'_{nn}$ is calculated. Vertical distances are neglected. For correlated growth all islands are supposed to grow on top of each other resulting in comparatively small distances $d'_{nn}$. From all the distances $d'_{nn}$ an average distance $\overline{d'_{nn}}$ is calculated and normalized by the maximum average distance possible for islands on a square lattice: $\overline{d_{nn}}/\sqrt{2}$, where $\overline{d_{nn}}$ is the average distance between islands in the surface layer. Thus a pairing probability is defined via:

$$P_p \quad := \quad 1 - \sqrt{2}\frac{\overline{d'_{nn}}}{\overline{d_{nn}}} \qquad \text{(VI.1)}$$

Examples of the pairing probability $P_p$ for the various cases of correlated growth, uncorrelated and anticorrelated growth are shown in Fig.VI.3a, b and c, respectively, together with the corresponding distance distributions. The average distance of surface islands $\overline{d_{nn}}$ is given as the full circle around the origin in the distance distribution plots. A variance $\sigma$ of the pairing probability can be introduced as the variance in the distances to the nearest neighbors $\sigma(P_p) = \sigma(d'_{nn}) = \sqrt{\langle \Delta {d'}^2_{nn} \rangle}$.

## VI.3 Simulation results

The key ingredient for vertical correlation of quantum dot layers is the strain field at the surface of the stack produced by the buried islands. The non-homogeneous strain increases the probability of island nucleation at certain positions. To allow for nucleation to take place at these distinguished places, the flux rate to the surface during deposition should not be chosen too high so that nucleation is driven rather by aggregation of adatoms at energetically favoured places than by accidental nucleation processes due to a high overall monomer density. For all the following simulations, the flux to the surface has been chosen to be $0.02$ monolayers per second. Generally, a surface coverage of $35\%$ is used. After deposition the island configuration was given $20$ seconds of time to equilibrate before overgrowing the island layer and thus freezing the strain field which is calculated self-consistently from the three dimensional extension of isotropic, elastic strain eqns.A.11.

All simulations are performed on a $250 \times 250$ grid. Binding energies are chosen as in Chap.V to be $E_s = 1.3$eV for surface bonds and $E_b = 0.3$ for the bonding between nearest neighbors. The elastic constants for the isotropic strain calculation are $\lambda = 0.32 \cdot 10^{12}$erg/cm$^3$ and $\mu = 0.54 \cdot 10^{12}$erg/cm$^3$, similar to the choices in Chap.IV. With $700$K as the temperature used in all simulations an enhanced adatom mobility is ensured.

### VI.3.1 Correlated growth vs. deposited layers

To show the increase in spatial ordering with the increase of deposited layers, a stack of islands consisting of 150 single layers was simulated. After each deposited layer of islands having a coverage of $35\%$ each, the pairing probability $P_p$ was calculated. The

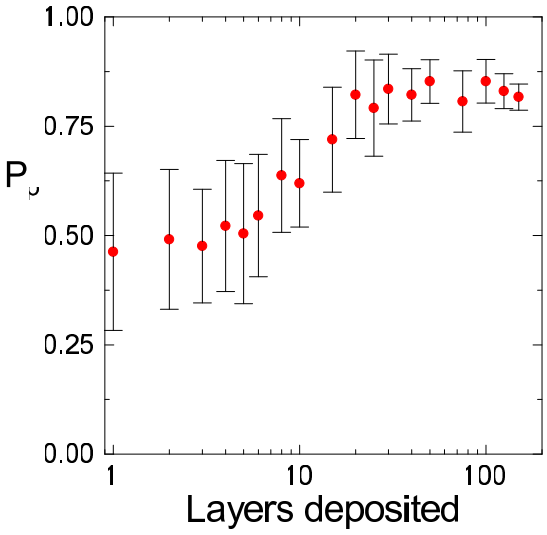


Fig. VI.4: Evolution of the pairing probability $P_p$ in dependence of the number of deposited layers consisting of island layer and capping layer. The error bars denote the variance $\sigma = \sqrt{\langle \Delta d'^{\,2}_{nn} \rangle}$ of the pairing probability. ($T = 700$K, $f = 0.02$Ml/s, $c = 35\%$, buffer layer thickness $15$Ml, simulation time $37.5$s/layer)

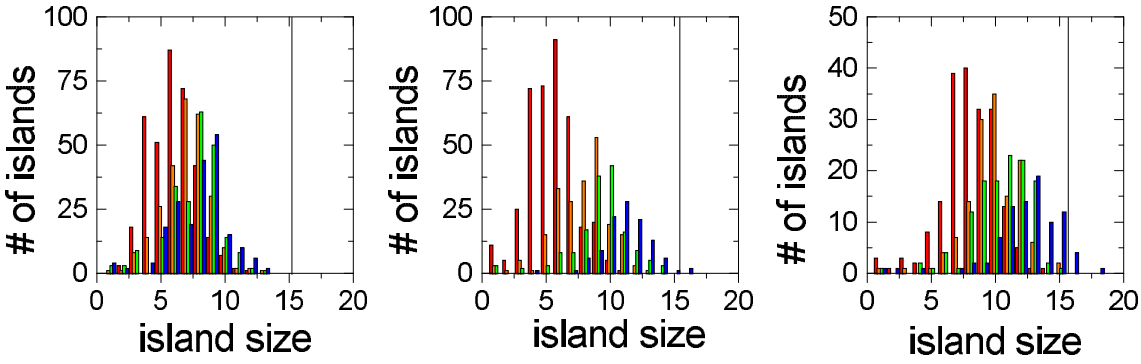


Fig. VI.5: Size distributions for buffer layer thicknesses of a) thirty, b) fifteen and c) five monolayers. The different colors denote the size distribution after 5 (red), 10 (orange), 15 (green) and 20 (blue) grown island layers. The vertical line marks the optimal island size for equilibrium conditions (after eq.IV.3). ($T = 700$K, $f = 0.02$Ml/s, $c = 35\%$, simulation time $37.5$s/layer)

spacer thickness was chosen to be $15$ monolayers. The resulting dependence of $P_p$ on the number of deposited layers is shown in Fig.VI.4.

For the first few layers the pairing probability is close to $0.5$ indicating uncorrelated growth. From the fifth layer on the pairing probability clearly tends towards larger values witch is a sign of correlated island growth. After the deposition of $20$ layers the pairing probability reaches a value of $0.8$ and increases only very slowly beyond this point.

For all further simulations a stack height of twenty layers has been assumed to be sufficient to characterize the growth mode.

### VI.3.2 Size ordering vs. deposited layers

For the above simulation with a buffer layer thickness of fifteen monolayers as well as for two equivalent simulations with five and thirty monolayers spacer thickness, respectively, the size distribution functions have been calculated after every five deposited island layers. The results are shown in Fig.VI.5.a to c.

It can be seen that with increasing number of deposited layers the size distribution shifts towards larger island sizes. This effect is most pronounced for thin buffer layers (Fig.VI.5.c).

The shift in the average island size can be understood as the approach of the equilibrium state, as it has been discussed in Chap.V. The additional strain from the buried layers enhances the mobility of the diffusing adatoms which is comparable to an increase in temperature. A higher growth temperature, on the other hand, means a faster evolution towards equilibrium. Additionally, the inhomogeneous strain field creates preferred nucleation sites for islanding at places of reduced strain. This effect induces a spatial correlation between the growing layer and the buried layers again promoting equilibration of the islands.

In Fig.VI.5a to c the average island size for equilibrium islands calculated after eq.IV.3 has been marked as a green, vertical line. The effect of strain is reduced for thick buffer layers, hence the acceleration in the equilibration process is less pronounced for spacer thicknesses of fifteen and thirty in Fig.VI.5.a and b, respectively.

### VI.3.3 Correlated growth vs. coverage

The dependence of the pairing probability on the total coverage of the island layerhas

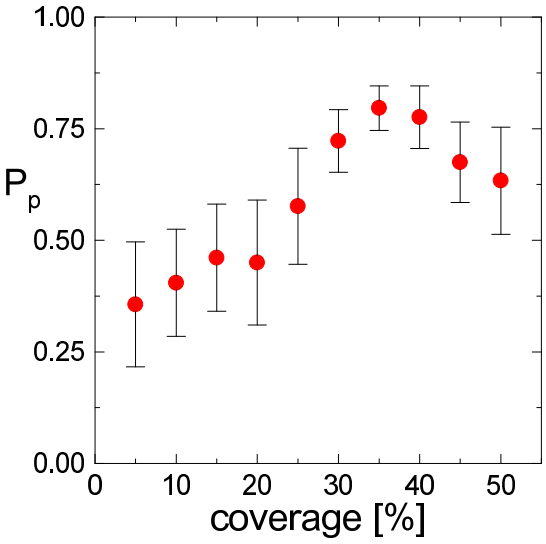


Fig. VI.6: Dependence of the pairing probability on the surface coverage. Error bars denote the variation $\sigma$ in the pairing probability. ($T = 700$K, $f = 0.02$Ml/s, spacer thickness 10Ml, relaxation time 20s/layer)

been studied by computing the pairing probability after the growth of twenty stacked island layers with varying coverage and a constant buffer layer thickness of ten monolayers. The result can be seen in Fig.VI.6.

For very low coverages below 10% the pairing probability indicates anticorrelated growth. As a result of the low coverage, the distance between islands is comparatively large and hence the areas of strain induced by the buried islands do not overlap (Fig.VI.7.a). Thus, adatoms are driven away from areas atop buried islands and nucleation takes place favorably in between buried islands, where the strain field is lowest. This consequently leads to anticorrelated growth.

For a coverage of about 10% the growth proceeds uncorrelated. For coverages well above 10% the growth mode changes to correlated growth. Here, the strain between the islands is strong due to a deceasing island separation with increasing coverage. Now the nucleation on top of buried islands becomes more favorable since here the surface is only weakly strained. This can be understood by looking at the strain generated at the island boundaries. The strain discontinuity along the boundary of large islands induces a constant strain at the island center which is usually weaker than the strain in between islands if the coverage is high enough (Fig.VI.7.b).

The pairing probability function in Fig.VI.6 has a maximum at a coverage of $c = 35\%$. Further increase of the coverage leads to clustering of islands and the correlation effect is reduced again.

For the following simulations the peak coverage of $35\%$ has been chosen in order to obtain the maximum correlation effect.

It has to be mentioned that in experiments the effect of anticorrelation for low coverages has not been observed. In this context it seems important to recall that the simulation is limited to strain effects that are purely energetical in nature. Dislocations, lattice defects or surface reactions caused by strain, which could well serve as island nuclei, are not included in the numerical routine. These phenomena do, however, influence the island nucleation considerably in growth experiments [Kun00].

### VI.3.4 Correlation and Anticorrealtion

In the last part of this chapter the dependence of the pairing probability on the buffer layer thickness is scrutinized. Simulations with parameters optimized for correlated growth have been done with varying spacer thicknesses. For a coverage of $35\%$ the pairing probability after the twentieth deposited island layer has been calulated to give a dependence of the pairing probability on spacer thickness shown in Fig.VI.8.

For a spacer thickness of less than $15$ monolayers the growth is correlated. For increasing buffer layer thicknesses the correlation de-

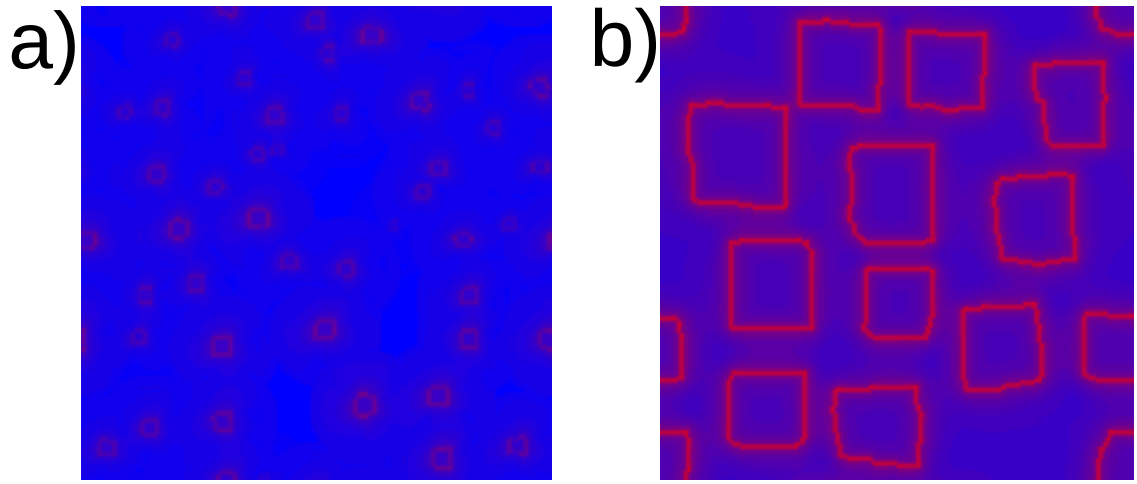


Fig. VI.7: Spatial distribution of strain fields for the case of a) low coverage with $c = 5\%$ and for b) high coverage with $c = 35\%$. Areas of low strain appear blue. Highly strained regions are colored red. Island layers are capped with a spacer of two monolayers thickness. ($T = 700$K, $f = 0.02$Ml/s, spacer thickness 2Ml, relaxation time 20s/layer)

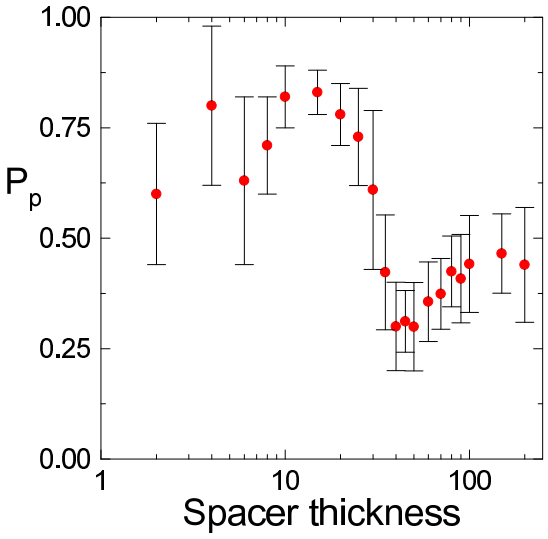


Fig. VI.8: Simulation results for the dependece of the pairing probability on the spacer thickness. Error bars represent the variation $\sigma$ of the pairing probability. ($T = 700$K, $f = 0.02$Ml/s, $c = 35\%$, simulation time 37.5s/layer, stack height 20 island layers)

cays and gives uncorrelated growth for a buffer thickness of about 25 monolayers. For even thicker spacer layers the growth becomes anti-correlated and assumes a minimum for a buffer thickness of forty monolayers. From here with increasing buffer thickness any correlation effect between sheets of islands decays again and uncorrelated growth is observed for spacers thicker than some 50 monolayers.

#### *VI.3.4.a Correlated regime*

The correlated growth regime can be found for thin spacer thicknesses. Here, as has been argued above, the least strained regions are areas above centers of buried islands (see Fig.VI.7.b). The effect of lower strain above island centers is solely induced by the island morphology, especially its size, and vanishes fast with increasing spacer thickness since for the isotropic strain model, the strain profile of a buried island becomes more and more spherical with increasing distance from the island. In the limit of large distances, the buried is-

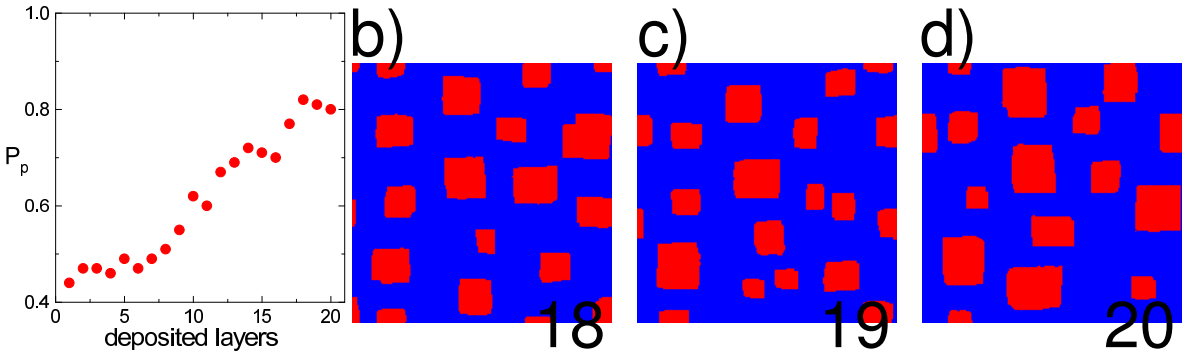


Fig. VI.9: Evolution of pairing probability depending on deposited layers for the case of correlated growth. The three topmost island distributions are shown in b), c) and d). Coverage $c = 35\%$, spacer thickness is $5$ monolayers, $T = 700$K, Flux $f = 0.01$Ml/s, simulation time $37.5$s/layer, stack height is $20$ layers.

land can be treated as a point source of strain with a spherical strain field.

It is thus important to note that the extent of correlated growth does not only depend on the spacer thickness but rather on the combined effect of the average island size and the buffer layer thickness. This observation is in clear contrast to anticorrelated growth, as will be shown below.

As a consequence, correlated growth can be observed for thin buffer layers and large islands. In Fig.VI.9.a the evolution of the pairing probability in dependence of the number of grown layers is shown. The buffer layer thickness for this simulation was chosen as five monolayers.

For the first few layers the growth occurs uncorrelated and then becomes increasingly correlated up to the 16th layer, where the pairing probability reaches saturation and remains almost constant at a value of $P_p = 0.8$. In Fig.VI.9.b to d the island distributions of the topmost three island layers are shown to demonstrate the spatial correlation in the vertical direction.

The interplay of spacer thickness and island size might also explain why correlated growth is not instantly observed. For the first few island layers the growth occurs uncorrelated but the size distribution shifts considerably towards larger islands (see Fig.VI.5) finally giving rise to correlated growth as seen in Fig.VI.9.a.

### *VI.3.4.b Anticorrelated regime*

As has been seen in the previous section, for large buffer layer thicknesses the buried islands appear as point sources of strain and the strain field at the surface has a circular symmetry around the island with a maximum value vertically above the island center. Nucleation of islands at the surface is consequently enhanced between the islands and anticorrelated growth is observed.

Since this growth mode does not depend on the lateral extension of the buried islands as sensitively as the correlated growth does, the onset of anticorrelated growth is already visible for the first few grown island layers in Fig.VI.10. After ten deposited island layers the pairing probability reaches saturation at a value of $0.26$. Fig.VI.10.b to d show the last three island layers of the stack consisting of $20$ layers in total. The island distributions clearly show vertically anticorrelated growth.

If the buffer layer becomes thicker than a critical thickness of some $50$ monolayers the

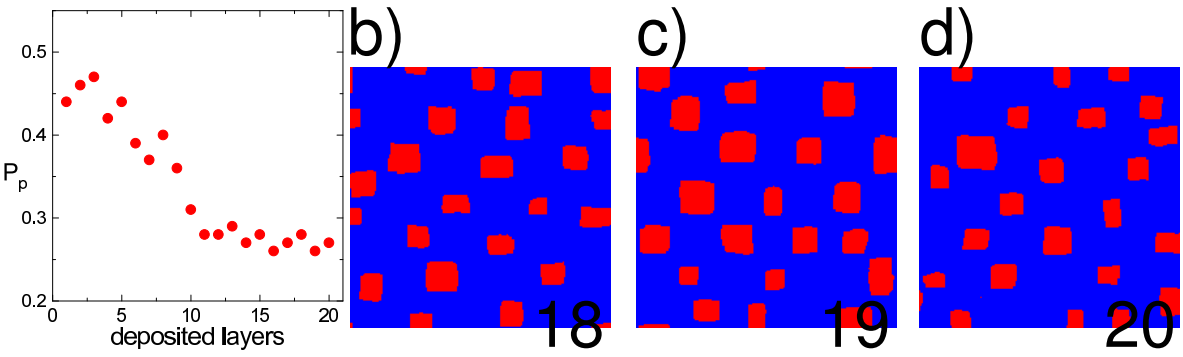


Fig. VI.10: Evolution of pairing probability depending on deposited layers for the case of anticorrelated growth. The three topmost island distributions are shown in b), c) and d). Coverage $c = 35\%$, spacer thickness is 40 monolayers, $T = 700$K, Flux $f = 0.01$Ml/s, simulation time 37.5s/layer, stack height is 20 layers.

increasing distance to the strain sources results in strain fields too weak to influence the surface kinetics of diffusing adatoms significantly and the growth occurs uncorrelated.

## VI.4 Conclusion

It has been shown in this chapter that successive overgrowth of island layers with substrate material under the assumption of an extended, three-dimensional strain field leads to an improvement of the self-organized size ordering and spatial arrangement of the islands. Thermodynamical equilibrium can be approached by kinetic deposition and diffusion processes alone without equilibrating the system for long periods of time.

For thin buffer layers, correlated growth can be found. Apart from the spacer thickness, correlated growth depends on the average size of the buried islands which also increases during the stacking process. Thus, the self-organized increase in average island size induces an additional aid in growing correlated island stacks.

For large spacer layers anticorrelated growth can be observed and for buffer layer thicknesses beyond growth proceeds uncorrelated.

These observations are in qualitative agreement with various experimental findings.

# VII.

# Conclusion

In all the previous chapters the effect of self-organization did have a major impact on the dynamics of island growth. For the particular system of heteroepitaxially growing quantum dots on a semiconductor surface it has been shown that the elastic strain generated by the lattice mismatch of substrate and adsorbate is intimately connected to the self-organizing processes by providing a means of long range interaction between the growing dots.

All simulations presented in this work were limited to the initial, two dimensional phase of growth, where the first monolayer is formed. These islands determine during the further steps of three dimensional growth the size and location of the fully grown quantum dots. The Monte Carlo simulation routine described in chapter II, which was used for all presented simulation runs included atom interactions elementary for surface kinetics and used a self-consistently calculated, extended strain field generated by the growing islands. Details on interaction terms and the simulation routine have been given in chapter II.

•

Though short ranged interactions like the nearest neighbor binding energy might be sufficient to induce ordering effects with respect to shape by preferring compact islands, neither size nor spatial ordering can be observed in the absence of elastic strain. It has been shown in chapter III that for islands with increasing size also the contribution of strain along the island boundary increases. Consequently the growth of islands is hindered by a destabilizing effect of strain and size ordering is induced. The average island size assumed in an ensemble of islands increases with increasing temperature up to a critical point, where the islands begin to dissociate. Is the system allowed to equilibrate for a certain time, a temperature regime can be found, where the size distribution becomes narrow, i.e. most islands are of the same size. By increasing the surface coverage the average island size increases as well up to the point of about $35\%$ where coalescence of islands or the transition from two-dimensional to three-dimensional island growth becomes relevant. Note, however, that this result has been obtained for systems with no or only short equilibration times. Hence the temperature dependence of the average island size given in chapter III is valid only for kinetically controlled systems. In those systems the flux of atoms to the surface during deposition has a pronounced effect on the island density on the surface, which increases with increasing flux.

The strain field does not only induce size ordering effects but is related to spatial ordering as well. Since the elastic strain extends along the substrate over distances of the order of typical island separations, it generates an island-island interaction. This interaction defines an optimal separation of islands or cre-

ates preferred nucleation sites. As a result, islands grow in ordered patterns. This interaction, however, has been found to be weak and spatial ordering has been observed for a narrow parameter window of high temperatures and long equilibration times only. Additionally, a proper coverage of about $35\%$ has to be chosen to minimize island separation.

An optimized set of parameters to achieve good spatial ordering and a narrow size distribution has been identified as high temperature $T = 700K$, low deposition flux $f = 0.001$Ml/s, a high coverage of $34\%$ and a long equilibration time of $T = 500s$.

•

As has been seen in chapter III the relaxation time clearly affects the average island sizes as well as the spread in the size distribution. Actually, there is a fundamental difference between kinetically controlled systems, which have had no or only little time for equilibration, and systems, which are close to the thermodynamic equilibrium, as was shown in chapter IV.

In the kinetically controlled regime the average island size increases with the systems temperature and small islands are expected for low temperatures, large islands for high temperatures. This behaviour has been verified experimentally as well as in theory. Thermodynamic equilibrium theory, however, predicts a different temperature dependence of the island sizes, where the average size decreases with increasing temperature.

Long time Monte Carlo simulations for different temperatures presented in chapter IV have shown, that the average island size during or shortly after deposition indeed follows a distribution as is expected for kinetically controlled systems. In the course of equilibration the average island sizes slowly approach their equilibrium values and a cross over from kinetically controlled size distributions towards equilibrium size distributions can be observed in the Monte Carlo simulations.

In the kinetically controlled regime the average island size is determined by the island density, which varies with deposition rate, and the strain, which limits the island size. For the thermodynamically controlled case strain alone sets the limit to the island sizes and the final self-organized systems state is completely independent of the deposition procedure.

•

By introducing anisotropic strain into the simulation routine it has been shown in chapter V that certain ordering effects in heteroepitaxial material systems can be explained by the elastic anisotropy of the growing compound.

It has been shown by [Sch98b] that in the material system $Si_{0.75}Ge_{0.25}/Si$ spatial self-organisation of islands along $Si(100)$ direction can be observed in LPE grown samples. By including the anisotropic bulk elastic moduli for $Si_{0.75}Ge_{0.25}$ into the strain calculation, a local minimum of the elastic strain energy has been identified. This minimum enhances the nucleation probability in the $(100)$ direction and thus generates spatial ordering in a preferred direction. Qualitatively a good agreement between the simulation results and the experiment has been found.

For low coverages of about $4\%$ mainly island polymers consisting of two or three islands form. For increasing coverages of $10\%$ long island chains can be found, resulting in a rather regular pattern at the surface.

However, it has to be mentioned that the simulation routine is not able to capture all relevant processes for LPE growth by design and agreement between simulation and experiment can only be expected asymptotically, i.e. close to thermodynamic equilibrium.

Though it would be a major task to adapt the program code to simulating LPE growth it would certainly be interesting to include an active wetting layer as it is observed in ex-

periment. An active wetting layer would contribute material to the growing islands in dependence on the local strain and significantly different growth dynamics could be expected.

•

In chapter VI the self-organisation processes in quantum dot superlattices have been investigated. It has been shown that the repeated growth of quantum dot layers in a vertical direction, separated only by a thin buffer layer, is a potent way to introduce spatial ordering. Again, the elastic strain is held responsible for the emergence of self-organized spatial correlation, since after overgrowth the strain of the buried islands creates preferred nucleation sites on the crystal surface.

After a certain number of deposited layers, depending on the thickness of the buffer layer, spatial correlation can be found for sufficiently large islands. Additionally, the average island size increases with the number of deposited layers. Again, this effect is more pronounced for thin buffer layers.

If the average island size becomes too small or the separating buffer layer too thick, anti-correlated growth can be observed. Here, the islands in the topmost layer grow in between buried islands. In the Monte Carlo simulations the transition from correlated growth to anti-correlated growth with increasing spacer thickness or decreasing surface coverage has been found and is in good agreement with experimental observations.

Optimal parameter sets have been identified for correlated and anti-correlated growth as $T = 700$K, $f = 0.01$Ml/s, $c = 35\%$ and a spacer thickness of $5$ and $30$ monolayers, respectively. These parameters lead to well pronounced correlated/anti-correlated growth conditions after the deposition of twenty monolayers.

As a future task one might add the possibility to compute a three dimensional strain field, which includes cubic anisotropy. It is likely that correlation and anti-correlation effects are related to elastic anisotropy. For certain parameter windows the self organization with respect to size ordering and spatial arrangement of islands might be further improved by the introduction of spacer layers with high elastic anisotropy.

•

The calculation of anisotropic strain as it was presented in this work is limited to cubic crystals. Further interesting results on growth dynamics might, however, be obtained by introducing a program code which is able to deal with fully anisotropic crystals and is not restricted to a certain symmetry. This extension would allow for a general approach to material specific simulations, which have been performed for the cubic $SiGe/Si$ system in chapterV with great success. Also additional ordering effects might be obtained for different symmetries in the elastic anisotropy.

Another valuable extension of the simulation routine would be the option to include the transition from two dimensional growth of islands to three dimensional growth of quantum dots in a self consistent way. This, again, would necessitate to expand the strain calculation into the third dimension to calculate a strain field in dependence of the exact shape of the dots. By this improvement statements about the critical layer thickness for the transition from 2D to 3D growth could be gained or even estimates about kinetically controlled quantum dot shapes extracted.

Also, the full three-dimensional shape of the quantum dots may influence the correlation and anti-correlation effects in quantum dot stacks.

# A.

# Appendix – Isotropic strain

For isotropic media the displacement field $\mathbf{u}(\mathbf{r})$ generated by the forces $\mathbf{F}$ satisfies the inhomogeneous, differential equation [Lan70]

$$\mathbf{F} = \frac{E}{2(1+\mu)}\left(\Delta\mathbf{u} + \frac{1}{1-2\mu}\nabla(\nabla\cdot\mathbf{u})\right) \tag{A.1}$$

This equation looks like Poisson's equation in electrostatics and can be solved similarly. The homogeneous form of eq.A.1 is also called Navier's equation.

A solution to this equation is to be found for the special case known as Cerruti's problem (see Fig.A.1) of a tangential force acting on the boundary of a semi-infinite solid. For the solution two potentials have to be defined: the Lamés strain potential and the Galerkin vector potential. Each of the both potentials is a solution to eq.A.1.

According to Helmholtz's theorem, any vector function $\mathbf{u}$ can be written as a sum of terms

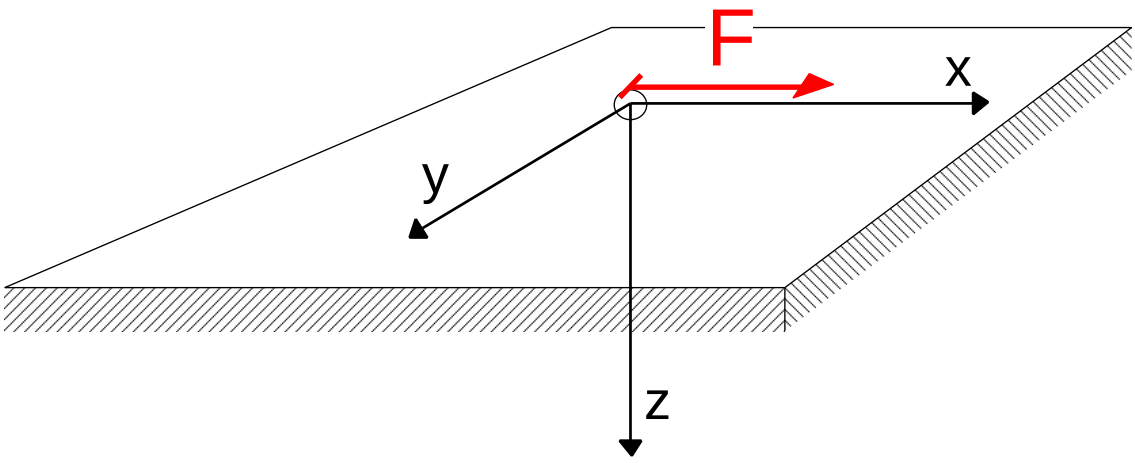


Fig. A.1: Cerruti's problem of a tangential force $F$ acting on the boundary of an semi-infinite plane along the $x$ direction.

resulting from a scalar and a vector potential $\Phi$ and $\mathbf{\Psi}$, respectively.

$$\mathbf{u} \;=\; \nabla\Phi + \nabla\times\mathbf{\Psi}, \qquad \text{with} \qquad \nabla\cdot\mathbf{\Psi} \;=\; 0. \tag{A.2}$$

If one chooses $\Delta\Phi = \text{const.}$ and $\mathbf{\Psi}= 0$, the scalar function $\Phi$ is called Lamé strain potential and it is easy to show that any harmonic function $\Phi$ can be used to satisfy Naviers eq.A.1 with

$$\mathbf{u} \;=\; \frac{1}{2\mu}\nabla\Phi, \qquad (\mu = \text{const.}). \tag{A.3}$$

Furthermore one can define a vector potential $\mathbf{V}$, that is connected to the displacement field by

$$2\mu\,\mathbf{u} \;=\; 2(1-\nu)\Delta\mathbf{V} - \nabla(\nabla\cdot\mathbf{V}). \tag{A.4}$$

This, again, is a general solution to the homogeneous Navier's eq.A.1, if the Galerkin vector $\mathbf{V}$ is a biharmonic function, since the substitution of eq.A.4 in eq.A.1 gives $\Delta(\Delta\mathbf{V}) = 0$.

To solve Cerruti's problem, a special choice for $\Phi$ and $\mathbf{V}$ is made

$$\Phi \;=\; \frac{C\,x}{r+z}, \qquad \mathbf{V} \;=\; \begin{pmatrix} A\,r \\ 0 \\ B\,x\,\ln(r+z) \end{pmatrix}, \tag{A.5}$$

and eq.A.3 and eq.A.4 superponed as

$$2\mu\,\mathbf{u} \;=\; \nabla\Phi + 2(1-\nu)\Delta\mathbf{V} - \nabla(\nabla\cdot\mathbf{V}). \tag{A.6}$$

to give the solution of the homogeneous eq.A.1.

By using the generalized Hooke's law, which relates the displacement field $\mathbf{u}$ defined by the strain tensor components $\varepsilon_{ij}$ to the stess tensor components $\sigma_{ij}$ the constants $A$, $B$ and $C$ can be determined by the conditions of vanishing stress at the surface for $\sigma_{zz}$ and $\sigma_{yz}$, while on any horizontal plane at depth $z$ from the surface the sum of all forces along the $x$-axis must balance $\mathbf{F}$, i. e.:

$$\int_{-\infty}^{\infty}\int_{-\infty}^{\infty} \sigma_{xz}\; dy\, dx \;=\; 0. \tag{A.7}$$

One finds for the constants $A$, $B$ and $C$:

$$A \;=\; \frac{|\mathbf{F}|}{4\pi(1-\nu)}, \qquad B \;=\; \frac{|\mathbf{F}|(1-2\nu)}{4\pi(1-\nu)}, \qquad C \;=\; \frac{|\mathbf{F}|(1-2\nu)}{2\pi}. \tag{A.8}$$

Now, the displacements can be calculated:

$$\begin{aligned} u_x &= \frac{|\mathbf{F}|}{4\,\pi\,\mu\,r}\left[1 + \frac{x^2}{r^2} + (1-2\nu)\left(\frac{r}{r+z} - \frac{x^2}{(r+z)^2}\right)\right] \\ u_y &= \frac{|\mathbf{F}|}{4\,\pi\,\mu\,r}\left[\frac{xy}{r^2} - \frac{xy(1-2\nu)}{(r+z)^2}\right] \\ u_z &= \frac{|\mathbf{F}|}{4\,\pi\,\mu\,r}\left[\frac{xz}{r^2} + \frac{x(1-2\nu)}{r+z}\right]. \end{aligned} \tag{A.9}$$

The components of the strain can be calculated using the strain-displacement relations

$$\varepsilon_{ij} = \frac{1}{2}\left(\frac{\partial u_i}{\partial x_j} + \frac{\partial u_j}{\partial x_i}\right) \tag{A.10}$$

to yield

$$\begin{aligned}
\varepsilon_{xx} &= \frac{|\mathbf{F}|\,x}{2\,\pi\,\mu\,r^3}\left[-\frac{3}{r^2}(x^2-\nu(y^2+z^2)) + \frac{1-2\nu}{(r+z)^2}\left((1-3\nu)r^2 - \frac{3r+z}{r+z}(y^2+\nu x^2)\right)\right] \\
\varepsilon_{yy} &= \frac{|\mathbf{F}|\,x}{2\,\pi\,\mu\,r^3}\left[-\frac{3}{r^2}(y^2-\nu(x^2+z^2)) + \frac{1-2\nu}{(r+z)^2}\left((3-\nu)r^2 - \frac{3r+z}{r+z}(x^2+\nu y^2)\right)\right] \\
\varepsilon_{zz} &= \frac{|\mathbf{F}|\,x}{2\,\pi\,\mu\,r^3}\left[-\frac{3}{r^2}(z^2-\nu(x^2+y^2)) - \frac{\nu(1-2\nu)}{(r+z)^2}\left(4\,r^2 - \frac{3r+z}{r+z}(x^2+y^2)\right)\right] \\
\varepsilon_{xy} &= \varepsilon_{yx} = \frac{|\mathbf{F}|(1+\nu)\,x}{2\,\pi\,\mu\,r^3}\left[-\frac{3x^2}{r^2} + \frac{\nu(1-2\nu)}{(r+z)^2}\left(-r^2+x^2+\frac{2\,r\,x^2}{r+z}\right)\right] \\
\varepsilon_{xz} &= \varepsilon_{zx} = \frac{3\,|\mathbf{F}|(1+\nu)\,z\,x^2}{2\,\pi\,\mu\,r^5} \\
\varepsilon_{yz} &= \varepsilon_{zy} = \frac{3\,|\mathbf{F}|(1+\nu)\,x\,y\,z}{2\,\pi\,\mu\,r^5}.
\end{aligned} \tag{A.11}$$

These expressions simplify considerably if the $z$-dependence is neglected by setting $z = 0$:

$$\begin{aligned}
\varepsilon_{xx} &= \frac{|\mathbf{F}|\,x}{\pi\,\mu\,r^5}\left[-x^2(1+4\nu-6\nu^2) - y^2(1-\nu-3\nu^2)\right] \\
\varepsilon_{yy} &= \frac{|\mathbf{F}|\,\nu\,x}{\pi\,\mu\,r^5}\left[x^2(1+\nu) - y^2(5-4\nu)\right] \\
\varepsilon_{zz} &= \frac{|\mathbf{F}|\,\nu\,x}{2\,\pi\,\mu\,r^5}\left[2\,x^2(1-\nu) - y^2(1-11\nu+6\nu^2)\right] \\
\varepsilon_{xy} &= \varepsilon_{yx} = \frac{|\mathbf{F}|\,x}{\pi\,\mu\,r^3}\left[\nu(1-\nu)\right] \\
\varepsilon_{xz} &= \varepsilon_{yz} = \varepsilon_{zx} = \varepsilon_{zy} = 0.
\end{aligned} \tag{A.12}$$

# B.

# Appendix – Anisotropic strain

For a complete modelling of the elastic strain on crystal surfaces it is indispensable to include anisotropy effects. This can be done by the use of the Green's tensor formalism from elasticity theory. The complete set of equations for the strain field for the general case are quite involved, instead the strain will be derived below for the special case of a cubic crystal. However, the cubic symmetry is assumed by many relevant semiconductor materials like $GaAs$ and $SiGe$.

## B.1 Green's tensor formalism

An anisotropic crystal that is subjected to external forces $P_j(\mathbf{r})$ acting on its surface will respond with a deformation that is represented by the elastic displacement field $u(\mathbf{r})$. The displacements are determined by the equilibrium equations of elastic theory in the bulk [Lan70], using the summation convention over equal indices,

$$\nabla_j \left[\lambda_{ijlm}(\mathbf{r}) \nabla_l \, u_m(\mathbf{r})\right] \quad = \quad 0 \tag{B.1}$$

where vanishing body forces are assumed. The forces acting along the boundary $S$ enter the boundary conditions

$$n_j(\mathbf{r}) \left[\lambda_{ijlm}(\mathbf{r}) \nabla_l \, u_m(\mathbf{r})\right] \mid_S \quad = \quad P_j(\mathbf{r}) \tag{B.2}$$

where $n_j(\mathbf{r})$ is the external normal to the crystal surface.

Formally, eq.B.1 with the boundary conditions B.2 can be solved by the solution of an equivalent set of equations

$$\nabla_j \left[\lambda_{ijlm}(\mathbf{r}) \nabla_l \, G_{mp}(\mathbf{r}, \mathbf{r}')\right] \quad = \quad \delta_{ip} \delta(\mathbf{r} - \mathbf{r}') \tag{B.3}$$

where $G(\mathbf{r}, \mathbf{r}')$ is the static Green's tensor of elasticity theory. Its components $G_{mp}(\mathbf{r}, \mathbf{r}')$ are the elastic deformations $u_p(\mathbf{r}')$ caused by a unit force acting at point $\mathbf{r}$ in direction $m$. These components satisfy the stress free boundary conditions of a crystal surface

$$n_j(\mathbf{r}) \left[\lambda_{ijlm}(\mathbf{r}) \nabla_l \, G_{mp}(\mathbf{r}, \mathbf{r}')\right] \mid_S \quad = \quad 0 \tag{B.4}$$

The elastic displacements $u_i(\mathbf{r})$ can be obtained from eq.B.3 by multiplying both sides by $u_i(\mathbf{r})$ and integrating over all space

$$\int_V d^3r\, u_i(\mathbf{r})\nabla_j \left[\lambda_{ijlm}(\mathbf{r})\nabla_l\, G_{mp}(\mathbf{r},\mathbf{r}')\right] \;=\; \int_V d^3r\, u_i(r)\delta_{ip}\delta(\mathbf{r}-\mathbf{r}') \tag{B.5}$$

Integration by parts gives

$$\oint_S d^2r\, u_i(\mathbf{r})\lambda_{ijlm}(\mathbf{r})\nabla_l G_{mp}(\mathbf{r},\mathbf{r}') - \int_V d^3r\, \left[\lambda_{ijlm}(\mathbf{r})\nabla_j u_i(\mathbf{r})\right]\nabla_l\, G_{mp}(\mathbf{r},\mathbf{r}') \;=\; u_p(\mathbf{r}') \tag{B.6}$$

The surface integral vanishes by inserting the boundary conditions B.4. Then, by applying the symmetry relation $\lambda_{ij\,lm} = \lambda_{lm\,ij}$ and another integration by parts of the second integral in eq.B.6 one obtains

$$-\oint_S d^2r\, G_{mp}(\mathbf{r},\mathbf{r}')\lambda_{lmij}(\mathbf{r})\nabla_j u_i(\mathbf{r}) + \int_V d^3r\, G_{mp}(\mathbf{r},\mathbf{r}')\nabla_l\left[\lambda_{lmij}(\mathbf{r})\nabla_j u_i(\mathbf{r})\right] \;=\; u_p(\mathbf{r}') \tag{B.7}$$

The second summand is equal to zero as can be seen by substituting the equilibrium eq.B.1. Inserting the boundary conditions B.2, exchanging $\mathbf{r}$ with $\mathbf{r}'$ and applying the theorem of reciprocity for the Green's tensor components $G_{ij}(\mathbf{r},\mathbf{r}') = G_{ji}(\mathbf{r},\mathbf{r}')$ one finds

$$u_i(\mathbf{r}) \;=\; -\oint_S d^2r'\, G_{ij}(\mathbf{r},\mathbf{r}')\, P_j(\mathbf{r}') \tag{B.8}$$

## B.2 Green's tensor components

Now, the Green's tensor components $G_{ij}(\mathbf{r},\mathbf{r}')$ have to be found for the special case of a semi-infinite crystal with a planar, stress free surface at $z = 0$. Furthermore, the crystal will be assumed to be homogeneous throughout the lower half plane ($z < 0$). Then the components of the Green's tensor depend only on the distances $\Delta x = x' - x$ and $\Delta y = y' - y$. If one restricts all considerations to the surface of the crystal, the z-components of $\mathbf{r}$ and $\mathbf{r}'$ are equal to zero and one finds

$$G(\mathbf{r},\mathbf{r}') \;=\; G(\Delta x, \Delta y) \tag{B.9}$$

For the following derivation of the Green's tensor components it will be most convenient to carry out a transformation into Fourier space. To this end forward and backward Fourier transformations of a quantity $A(\mathbf{r})$ are defined as

$$\tilde{A}(\mathbf{k}) \;=\; \int d^2r\, e^{-i\mathbf{kr}} A(\mathbf{r}) \tag{B.10}$$

$$A(\mathbf{r}) \;=\; \frac{1}{2\pi}\int d^2r\, e^{i\mathbf{kr}} \tilde{A}(\mathbf{k}) \tag{B.11}$$

Eq.B.8 in Fourier space then reads

$$\tilde{u}_i(\mathbf{k}) \;=\; -\tilde{G}_{ij}(\mathbf{k})\, \tilde{P}_j(\mathbf{k}) \tag{B.12}$$

Now, the static Green's tensor for a cubic crystal in $k$-space has been derived by Portz and Maradudin [Por77]. Unfortunately, the vectorial basis for the above considerations will in general

not be the same as for the tensor components $g_{lm}(\mathbf{k})$ used in [Por77]. To find the components $\tilde{G}_{ij}(\mathbf{k})$ it is necessary to introduce a rotation of coordinate space by an angle $\Phi$ so that $\tilde{G}_{ij}$ can be expressed in terms of $g_{lm}$.

This rotation may be expressed by the transformation $S_{il}$ and its back transformation $S_{il}^{-1}$ like

$$S_{il} = \begin{pmatrix} n_x & -n_y & 0 \\ n_y & n_x & 0 \\ 0 & 0 & 1 \end{pmatrix}, \qquad S_{il}^{-1} = \begin{pmatrix} n_x & n_y & 0 \\ -n_y & n_x & 0 \\ 0 & 0 & 1 \end{pmatrix}. \tag{B.13}$$

where $n_x = \cos\Phi$ and $n_y = \sin\Phi$ are the components of the two dimensional unit vector $\mathbf{n}$ in direction of $\mathbf{k}$. Then the components of the Green's tensor in Fourier space $\tilde{G}_{ij}$ are given as

$$\tilde{G}_{ij}(\mathbf{k}) = \sum_{lm} S_{il}^{-1}\, g_{lm}(\mathbf{k})\, S_{mj} \tag{B.14}$$

or explicitly

$$\begin{aligned}
\tilde{G}_{xx}(\mathbf{k}) &= n_x^2\, g_{xx}(\mathbf{k}) - n_x n_y\, g_{xy}(\mathbf{k}) - n_x n_y\, g_{yx}(\mathbf{k}) + n_y^2\, g_{yy}(\mathbf{k}) \\
\tilde{G}_{xy}(\mathbf{k}) &= n_x n_y\, g_{xx}(\mathbf{k}) + n_x^2\, g_{xy}(\mathbf{k}) - n_y^2\, g_{yx}(\mathbf{k}) - n_x n_y\, g_{yy}(\mathbf{k}) \\
\tilde{G}_{yx}(\mathbf{k}) &= n_x n_y\, g_{xx}(\mathbf{k}) - n_y^2\, g_{xy}(\mathbf{k}) + n_x^2\, g_{yx}(\mathbf{k}) - n_x n_y\, g_{yy}(\mathbf{k}) \\
\tilde{G}_{yy}(\mathbf{k}) &= n_y^2\, g_{xx}(\mathbf{k}) + n_x n_y\, g_{xy}(\mathbf{k}) + n_x n_y\, g_{yx}(\mathbf{k}) + n_x^2\, g_{yy}(\mathbf{k})
\end{aligned} \tag{B.15}$$

From [Por77] the form of the Green's tensor components of a cubic crystal at the crystal surface is known to be

$$g_{lm}(\mathbf{k}) = \frac{1}{c_{44}k}\mathcal{H}_{lm}(\mathbf{n}) \tag{B.16}$$

with $c_{44} = \lambda_{yzyz}$ the shear modulus of a cubic crystal and $\mathcal{H}_{lm}$ dimensionless polynomials, that reflect the angular dependence of anisotropic strain. The polynomials $\mathcal{H}_{lm}$ depend only on ratios of elastic moduli and the direction of $\mathbf{k}$. By retaining only the two lowest order polynomials, $\mathcal{H}_{lm}$ can be approximated to be

$$\begin{aligned}
\mathcal{H}_{xx}(\mathbf{n}) &= \left[A_{11} + 8\,B_{11}\left(n_x^2\, n_y^2 - \frac{1}{8}\right)\right] \\
\mathcal{H}_{xy}(\mathbf{n}) &= 4\,B_{12}\, n_x\, n_y (n_y^2 - n_x^2)\left[1 + 8\,C_{12}\left(n_x^2\, n_y^2 - \frac{1}{8}\right)\right] \\
\mathcal{H}_{yx}(\mathbf{n}) &= 4\,B_{21}\, n_x\, n_y (n_y^2 - n_x^2)\left[1 + 8\,C_{21}\left(n_x^2\, n_y^2 - \frac{1}{8}\right)\right] \\
\mathcal{H}_{yy}(\mathbf{n}) &= \left[A_{22} + 8\,B_{22}\left(n_x^2\, n_y^2 - \frac{1}{8}\right)\right]
\end{aligned} \tag{B.17}$$

while the necessesary symmetry properties are still obeyed. These interpolated formulas show good agreement with the exact solutions obtained numerically in [Por77] (see also Fig.B.1). The constants $A_{11}$, $A_{22}$, $B_{11}$, $B_{12}$, $B_{21}$, $B_{22}$, $C_{12}$ and $C_{21}$ contain the material parameters, that determine the anisotropic parameters of the crystal. The cubic anisotropy can be eliminated by setting $B_{11} = B_{12} = B_{21} = B_{22} = 0$. This is done in Appendix C to show the equivalence of strain fields for the isotropic and the anisotropic expressions.

To find the Green's tensor components in real space, eqns.B.17 have to be inserted into eqns.B.15 and the Fourier back transform to be applied. As it turns out after lengthy and cumbersome evaluations of Fourier integrals of up to sixth order polynomials [Shc99b], the Fourier back transform is rather simple. It can be obtained simply by the following substitutions

$$\frac{1}{k} \;\rightarrow\; \frac{1}{2\pi\, r}, \qquad n_x^2 \;\rightarrow\; m_y^2, \qquad n_x\, n_y \;\rightarrow\; -m_y\, m_x, \qquad n_y^2 \;\rightarrow\; m_x^2 \tag{B.18}$$

where $\mathbf{m}$ is the unit vector in real space with $m_x = x/r$ and $m_y = y/r$; The back transform then yields for the Green's tensor components

$$\begin{aligned}
G_{xx}(\mathbf{r}) &= \frac{1}{2\pi\, c_{44}}\,\frac{1}{r}\left[m_y^2\, h_{xx}(\mathbf{m}) + m_x\, m_y\, h_{xy}(\mathbf{m}) + m_x\, m_y\, h_{yx}(\mathbf{m}) + m_x^2\, h_{yy}(\mathbf{m})\right] \\
G_{xy}(\mathbf{r}) &= \frac{1}{2\pi\, c_{44}}\,\frac{1}{r}\left[-m_x\, m_y\, h_{xx}(\mathbf{m}) + m_y^2\, h_{xy}(\mathbf{m}) - m_x^2\, h_{yx}(\mathbf{m}) + m_x\, m_y\, h_{yy}(\mathbf{m})\right] \\
G_{yx}(\mathbf{r}) &= \frac{1}{2\pi\, c_{44}}\,\frac{1}{r}\left[-m_x\, m_y\, h_{xx}(\mathbf{m}) - m_x^2\, h_{xy}(\mathbf{m}) + m_y^2\, h_{yx}(\mathbf{m}) + m_x\, m_y\, h_{yy}(\mathbf{m})\right] \\
G_{yy}(\mathbf{r}) &= \frac{1}{2\pi\, c_{44}}\,\frac{1}{r}\left[m_x^2\, h_{xx}(\mathbf{m}) - m_x\, m_y\, h_{xy}(\mathbf{m}) - m_x\, m_y\, h_{yx}(\mathbf{m}) + m_y^2\, h_{yy}(\mathbf{m})\right]
\end{aligned} \tag{B.19}$$

with the angular dependent functions

$$\begin{aligned}
h_{xx}(\mathbf{m}) &= \left[A_{11} + 8\, B_{11}\left(m_x^2\, m_y^2 - \frac{1}{8}\right)\right] \\
h_{xy}(\mathbf{m}) &= 4\, B_{12}\, m_x\, m_y (m_y^2 - m_x^2)\left[1 + 8\, C_{12}\left(m_x^2\, m_y^2 - \frac{1}{8}\right)\right] \\
h_{yx}(\mathbf{m}) &= 4\, B_{21}\, m_x\, m_y (m_y^2 - m_x^2)\left[1 + 8\, C_{21}\left(m_x^2\, m_y^2 - \frac{1}{8}\right)\right] \\
h_{yy}(\mathbf{m}) &= \left[A_{22} + 8\, B_{22}\left(m_x^2\, m_y^2 - \frac{1}{8}\right)\right]
\end{aligned} \tag{B.20}$$

## B.3 Material Parameters

Now, the last task is to determine the material parameters $A_{ij}$, $B_{ij}$ and $C_{ij}$. The values for $A_{11}$, $A_{22}$, $B_{11}$ and $B_{22}$ can be expressed analytically in terms of the elastic constants $c_{11}$, $c_{12}$ and $c_{44}$ in Voigt notation [Shc99b, Shc95a].

$$\begin{aligned}
A_{11} &= \frac{1}{2}\left[\frac{-A\, c_{11}\sqrt{-2\Delta\,\frac{(c_{11}+c_{12})}{c_{11}} + 4}}{2(c_{11}+c_{12})} - \frac{c_{11}\, c_{44}\sqrt{-\Delta\left(2\frac{c_{12}}{c_{11}} + 1\right) + 2\sqrt{\Delta\,\frac{c_{44}+c_{12}}{c_{11}}}}}{c_{11}\, c_{44}\Delta + c_{12}(c_{11} - c_{12})}\right] \\
A_{22} &= -\frac{1}{2}\left[1 + \sqrt{A}\right] \\
B_{11} &= \frac{1}{2}\left[\frac{-A\, c_{11}\sqrt{-2\Delta\,\frac{(c_{11}+c_{12})}{c_{11}} + 4}}{2(c_{11}+c_{12})} + \frac{c_{11}\, c_{44}\sqrt{-\Delta\left(2\frac{c_{12}}{c_{11}} + 1\right) + 2\sqrt{\Delta\,\frac{c_{44}+c_{12}}{c_{11}}}}}{c_{11}\, c_{44}\Delta + c_{12}(c_{11} - c_{12})}\right] \\
B_{22} &= -\frac{1}{2}\left[1 - \sqrt{A}\right]
\end{aligned} \tag{B.21}$$

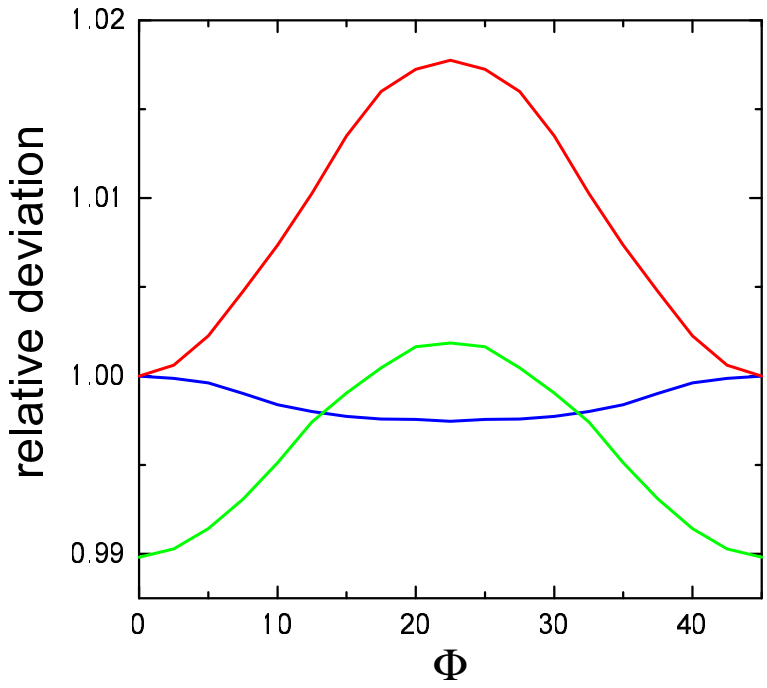


Fig. B.1: Relative deviation of the interpolated formulas $\mathcal{H}^{int}$ given by eqns.B.17 from the numerically exact solutions $\mathcal{H}$ in dependence of the azimuthal angle $\Phi$ where $\Phi = 0$ corresponds to the $\langle 110 \rangle$direction and $\Phi = 45^o$ corresponds to the $\langle 100 \rangle$direction. Plotted are $\mathcal{H}^{int}_{xx}/\mathcal{H}_{xx}$ in blue, $\mathcal{H}^{int}_{yy}/\mathcal{H}_{yy}$ in red and $\mathcal{H}^{int}_{xy}/\mathcal{H}_{xy}$ in green.

where the the cubic anisotropy $A$ as defined in eq.II.10 has been used as well as the derived quantity $\Delta$

$$\Delta \quad = \quad \left(\frac{1}{A} - 1\right). \tag{B.22}$$

It is possible to give explicit expressions for these parameters, since the dependence of $g_{11}(\mathbf{k})$ and $g_{22}(\mathbf{k})$ on the elastic constants $c_{11}$, $c_{12}$ and $c_{44}$ is known from [Shc95a]. By a numerical evaluation of the exact equations for $\mathcal{H}_{12}$ and $\mathcal{H}_{21}$ from [Por77], the parameters $B_{12}$, $B_{21}$, $C_{12}$ and $C_{21}$ can be obtained from a fit to the numerically exact solutions.

Exemplarily, the parameters $A_{11}, \ldots, C_{21}$ are given for the material systems $GaAs$ and $Si_{0.75}Ge_{0.25}$ in table B.1. The elastic constants $c_{11}$, $c_{12}$ and $c_{44}$ for various semiconductors with zinc-blend or diamond structure are shown in table B.2.

To show the good agreement of the interpolated formulas eqns.B.17 with the exact solutions obtained by numerical evaluations of the complete equations in [Por77], Fig.B.1 shows the angular dependence of the relative deviations $\mathcal{H}^{int}/\mathcal{H}$ for $GaAs$ parameters [Shc99b]. The parameters for $\mathcal{H}^{int}_{xx}$ and $\mathcal{H}^{int}_{yy}$ have been calculated directly from the elastic constants of $GaAs$ while the parameters in $\mathcal{H}^{int}_{xy}$ have been obtained by a fit to numerically obtained exact solutions. All deviations are well below two percent.

| Parameter | $GaAs$ | $Si_{0.75}Ge_{0.25}$ |
|---|---|---|
| $A_{11}$ | -0.9661 | 0.4193 |
| $A_{22}$ | -1.1765 | -1.1251 |
| $B_{11}$ | -0.0677 | 0.0697 |
| $B_{12} = B_{21}$ | 0.0926 | -0.0534 |
| $B_{22}$ | 0.1765 | 0.1251 |
| $C_{12} = C_{21}$ | -0.0780 | 0.0962 |

Table B.1: Elastic parameters for the cubic semiconductors $SiGe$ and $GaAs$. The elastic constants for the compound $Si_{0.75}Ge_{0.25}$ are obtained in linear approximation from the bulk values of $Si$ and $Ge$.

| | $c_{11}$ [$10^{11}$erg/cm$^3$] | $c_{12}$ [$10^{11}$erg/cm$^3$] | $c_{44}$ [$10^{11}$erg/cm$^3$] |
|---|---|---|---|
| $C$ | 10.76 | 1.25 | 5.77 |
| $Si$ | 16.58 | 6.39 | 7.96 |
| $Ge$ | 12.85 | 4.83 | 6.68 |
| $Si_{0.75}Ge_{0.25}$ | 15.79 | 6.00 | 7.65 |
| $AlP$ | 13.20 | 6.30 | 6.15 |
| $AlAs$ | 12.50 | 5.34 | 5.42 |
| $AlSb$ | 8.77 | 4.34 | 4.08 |
| $GaP$ | 14.12 | 6.25 | 7.05 |
| $GaAs$ | 11.81 | 5.32 | 5.94 |
| $GaSb$ | 8.84 | 4.03 | 4.32 |
| $InP$ | 10.22 | 5.76 | 4.60 |
| $InAs$ | 8.33 | 4.53 | 3.96 |
| $InSb$ | 6.58 | 3.57 | 2.98 |
| $ZnS$ | 10.32 | 6.46 | 4.62 |
| $ZnSe$ | 8.10 | 4.88 | 4.41 |
| $ZnTe$ | 7.13 | 4.07 | 3.12 |
| $CdTe$ | 5.35 | 3.68 | 1.99 |
| $HgSe$ | 6.90 | 5.19 | 2.33 |
| $HgTe$ | 5.08 | 3.58 | 2.05 |

Table B.2: Elastic constants for semiconductors with zinc-blend or diamond structure [Hel82]. The elastic constants for the compound $Si_{0.75}Ge_{0.25}$ are obtained in linear approximation from the bulk values of $Si$ and $Ge$.

## B.4 Anisotropic strain field

Once the static Green's functions are known, it is possible to derive the strain field $\varepsilon(\boldsymbol{r})$ from the derivatives of the displacement field $u(\boldsymbol{r})$ given by eq.B.8. One has

$$\begin{aligned}\varepsilon_{ik}(\mathbf{r}) &= \frac{1}{2}\left(\frac{\partial u_i(\mathbf{r})}{\partial x_k}+\frac{\partial u_k(\mathbf{r})}{\partial x_i}\right)\\ &= \frac{1}{2}\left[\frac{\partial}{\partial x_k}\oint_S d^2r'\,G_{ij}(\mathbf{r},\mathbf{r}')\,P_j(\mathbf{r}')+\frac{\partial}{\partial x_i}\oint_S d^2r'\,G_{kj}(\mathbf{r},\mathbf{r}')\,P_j(\mathbf{r}')\right]\end{aligned} \tag{B.23}$$

By approximating the boundary of an island by straight line segments of length $L$ where the line forces $P_j(\mathbf{r}')$ act, the surface integral can be broken down into a sum. The summation will be carried out at all discrete places $\mathbf{r}''$ where $\mathbf{r}'' = \{\mathbf{r}' \mid P_j(\mathbf{r}') \neq 0\}$. One finds

$$\varepsilon_{ik}(\mathbf{r}) = L\sum_{\mathbf{r}''}\frac{\partial G_{ij}(\mathbf{r},\mathbf{r}'')}{\partial x_k}\,P_j(r'') \tag{B.24}$$

The partial derivatives of $G_{ij}(\mathbf{r},\mathbf{r}')$ can be easily obtained but the calculations are lengthy and will not be presented here.

# C.

# Appendix – Equivalence of strain models

In the isotropic limit the anisotropic formulas for the elastic strain as defined in Appendix B reduce to the isotropic formulas from Appendix A, as is shown below. In both cases the equilibrium equations of elasticity theory have been solved and, consequently, the Green's formalism from Appendix B can be understood to be a mathematical extension of the potential ansatz made in Appendix A.

## C.1 Anisotropic formulas

Following the definitions from the previous section Appendix B, the displacement field in an anisotropic crystal is given by

$$u_i(\mathbf{r}) \quad = \quad -\oint\limits_S d^2\mathbf{r}' G_{ij}(\mathbf{r},\mathbf{r}') P_j(\mathbf{r}') \tag{C.1}$$

were the body forces are assumed to be zero and the crystal to be homogeneous.

### C.1.1 Fully anisotropic case

By examining surface forces only, the dependence on the $z$-direction can be neglected and only the surface components of the Green's tensor

$$\begin{aligned}
G_{xx}(\mathbf{r}) &= \frac{1}{2\pi c_{44}} \frac{1}{r^3} \left[ y^2 h_{11} + xy h_{12} + xy h_{21} + x^2 h_{22} \right] \\
G_{xy}(\mathbf{r}) &= \frac{1}{2\pi c_{44}} \frac{1}{r^3} \left[ -xy h_{11} + y^2 h_{12} - x^2 h_{21} + xy h_{22} \right] \\
G_{yx}(\mathbf{r}) &= \frac{1}{2\pi c_{44}} \frac{1}{r^3} \left[ -xy h_{11} - x^2 h_{12} + y^2 h_{21} + xy h_{22} \right]
\end{aligned}$$

$$G_{yy}(\mathbf{r}) = \frac{1}{2\pi c_{44}}\frac{1}{r^3}\left[x^2 h_{11} - xy h_{12} - xy h_{21} + y^2 h_{22}\right] \tag{C.2}$$

with $h(m)$ given by eqns.B.20 need to be considered.

### C.1.2 Isotropic reduction

To compare the analytical formulas for the anisotropic case to the isotropic one we set $B_{11} = B_{12} = B_{21} = B_{22} = 0$. The Green's functions then simplify to

$$\begin{aligned} G_{xx}(\mathbf{r}) &= \frac{1}{2\pi c_{44}}\frac{1}{r^3}\left[A_{11}y^2 + A_{22}x^2\right] \\ G_{yy}(\mathbf{r}) &= \frac{1}{2\pi c_{44}}\frac{1}{r^3}\left[A_{11}x^2 + A_{22}y^2\right] \\ G_{xy}(\mathbf{r}) &= G_{yx}(\mathbf{r}) = \frac{1}{2\pi c_{44}}\frac{1}{r^3}\left[-A_{11}xy + A_{22}xy\right] \end{aligned} \tag{C.3}$$

For a $\delta$-like force acting along the x-direction (tangential to the surface) $P(r) = P\delta(x)$, one gets:

$$\begin{aligned} u_x(\mathbf{r}) &= -\oint_S d^2r' G_{xx}(r,r')P\delta(x') = -\frac{P}{2\pi c_{44}}\frac{1}{r^3}\left[A_{11}y^2 + A_{22}x^2\right] \\ &= -\frac{A_{22}}{c_{44}}\frac{P}{2\pi}\frac{1}{r^3}\left[x^2 + \frac{A_{11}}{A_{22}}y^2\right] \end{aligned} \tag{C.4}$$

$$\begin{aligned} u_y(\mathbf{r}) &= -\oint_S d^2r' G_{xy}(r,r')P\delta(x') = -\frac{P}{2\pi c_{44}}\frac{1}{r^3}\left[-A_{11}xy + A_{22}xy\right] \\ &= -\frac{A_{22}}{c_{44}}\frac{P}{2\pi}\frac{1}{r^3}\left[xy\left(\frac{A_{22} - A_{11}}{A_{22}}\right)\right] \end{aligned} \tag{C.5}$$

## C.2 Isotropic displacements as solution of Cerruti's problem

On the other hand, for a force $P$ tangential to the crystal surface acting at one point along the $x$-direction the solution in terms of displacements is given by [Saa74]

$$\begin{aligned} u_x(\mathbf{r}) &= \frac{P}{4\pi G}\frac{1}{r}\left[1 + \frac{x^2}{r^2} + (1-2\nu)\left[\frac{r}{r+z} - \frac{x^2}{(r+z)^2}\right]\right] \\ &\overset{z=0}{=} \frac{1}{G}\frac{P}{2\pi}\frac{1}{r^3}\left[x^2 + (1-\nu)y^2\right] \end{aligned} \tag{C.6}$$

$$u_y(\mathbf{r}) = \frac{P}{4\pi G}\frac{1}{r}\left[\frac{xy}{r^2} - \frac{(1-2\nu)x}{(r+z)^2}\right] \overset{z=0}{=} \frac{1}{G}\frac{P}{2\pi}\frac{1}{r^3}\left[\nu xy\right] \tag{C.7}$$

With the choice of constants for Poisson's ratio $\nu$ and the shear modulus $G = \mu$, which can be gained from eqns.B.21 by assuming isotropic conditions with $\Delta = 0$ and $A = 1$,

$$\begin{aligned} \nu &= \frac{A_{22} - A_{11}}{A_{22}} \\ \mu = G &= -\frac{c_{44}}{A_{22}} \end{aligned} \tag{C.8}$$

it is easy to show that the eqations (C.4, C.5) and (C.6, C.7) are indeed equivalent.

# Bibliography


[Abs96] G. Abstreiter, P. Schittenhelm, C. Engel, E. Silveria, A. Zrenner, D. Meertens, and W. Jäger. *Growth and characterization of self-assembled Ge-rich islands on Si.* Semicond. Sci. Technol., **11**, 1521 (1996).

[Ale88] O. L. Alerhand, D. Vanderbilt, R. D. Maede, and J. D. Joannopoulos. *Spontaneous formation of stress domains on crystal surfaces.* Phys. Rev. Lett., **61**, 1973 (1988).

[Bal94] G. S. Bales and D. C. Chrzan. *Dynamics of irreversible island growth during submonolayer epitaxy.* Phys. Rev. B, **50**, 6057 (1994).

[Bar92] M. C. Bartelt and J. W. Evans. *Scaling analysis of diffusion-mediated island growth in surface adsorption processes.* Phys. Rev. B, **46**, 12675 (1992).

[Bar95] A.-L. Barabási and H. E. Stanley. *Fractal concepts in surface growth* (Cambridge University Press, Cambridge, U.K., 1995).

[Bar97a] A.-L. Barabási. *Self-assembled island formation in heteroepitaxial growth.* Appl. Phys. Lett., **70**, 2565 (1997).

[Bar97b] A.-L. Barabási. *Self-organized superlattice formation in $II-VI$ and $III-V$ semiconductors.* Appl. Phys. Lett., **70**, 764 (1997).

[Bau85] E. Bauser. In: E. Kalidis (ed.), *Crystal Growth of Electronic Materials*, 41 (Elsevier, New York, 1985).

[Bea00] K. M. Beatty and K. A. Jackson. *Monte Carlo modeling of silicon crystal growth.* J. of Crystal Growth, **211**, 13 (2000).

[Bim96] D. Bimberg, N. N. Ledentsov, M. Grundmann, N. Kirstaedter, O. G. Schmidt, M. H. Mao, V. Ustinov, A. Egorov, A. Zhukov, P. Kop'ev, Z. Alferov, S. Ruvimov, U. Gösele, and J. Heydenreich. *InAs-GaAs quantum pyramid lasers: in situ growth, radiative lifetimes and polarization properties.* Jpn. J. Appl. Phys., **35**, 1311 (1996).

[Bim99] D. Bimberg, M. Grundmann, and N. Ledentsov. *Quantum Dot Heterostructures* (John Wiley & Sons Ltd., New York, 1999).

[Boi95] G. Boisvert, L. J. Lewis, M. J. Puska, and R. M. Nieminen. *Energetics of diffusion on the $(100)$ and $(111)$ surfaces of $Ag$, $Au$ and $Ir$ from first principles.* Phys. Rev. B, **52**, 9078 (1995).

[Boi98] G. Boisvert and L. J. Lewis. *Island morphology and adatom self-diffusion on $Pt(111)$.* Phys. Rev. B, **57**, 1881 (1998).

[Bor75] A. B. Bortz, M. H. Kalos, and J. L. Lebowitz. *A new algorithm for Monte Carlo simulations of Ising spin systems.* J. Comp. Phys., **17**, 10 (1975).

[Bos99a] S. Bose and E. Schöll. *Kinetic Monte Carlo Simulation of the Nucleation of Self-Assembled Quantum Dots.* In: D. Gershoni (ed.), *Proc. 24th International Conference on The Physics of Semiconductors (ICPS-24), Jerusalem, Israel* (World Scientific, Singapore, 1999).

[Bos99b] S. Bose and E. Schöll. *Optimization of the size distribution of self-organized quantum dots.* In: *Proceedings of the $7^{th}$ International Symposium on Nanostructure: Physics and Technology*, 506–509 (Ioffe Institut, St. Petersburg, 1999).

[Bos00] S. Bose. *Pattern formation at semiconductor interfaces and surfaces.* Ph.D. thesis, Technische Universität Berlin (2000).

[Car98] A. Carlsson, L. R. Wallenberg, C. Persson, and W. Seifert. *Strain state in semiconductor quantum dots on surfaces: a comparison of electron microscopy and finite element calculations.* Surf. Sci., **406**, 48 (1998).

[CC95] C. Carter-Coman, A. S. Brown, R. Bicknell-Tassius, N. M. Jokerst, F. Fournier, and D. E. Dawson. *Strain-modulated epitaxy: Modification of growth kinetics via patterened, compliant substrates.* J. Vac. Sci. Technol. B, **14**, 2170 (1995).

[Cla91] S. Clarke, M. R. Wilby, and D. D. Vvedensky. *Theory of homoepitaxy on Si(001).* Surf. Sci., **255**, 91 (1991).

[Cop90] M. Copel, M. C. Reuter, M. H. von Hoegen, and R. M. Tromp. *Influence of surfactants in $Ge$ and $Si$ epitaxy on $Si(001)$.* Phys. Rev. B, **42**, 11682 (1990).

[Dar97] I. Daruka and A.-L. Barabási. *Dislocation-Free Island Formation in Heteroepitaxial Growth: A Study at Equilibrium.* Phys. Rev. Lett., **79**, 3708 (1997).

[Dar98] I. Daruka and A.-L. Barabási. *Equilibrium phase diagrams for dislocation free self-assembled quantum dots.* Appl. Phys. Lett., **72**, 2102 (1998).

[Dar99a] I. Daruka, A.-L. Barabási, S. J. Zhou, T. C. Germann, P. S. Lomdahl, and A. R. Bishop. *Molecular-dynamics investigation of the surface stress distribution in a $Ge/Si$ quantum dot superlattice.* Phys. Rev. B, **60**, R2150 (1999).

[Dar99b] I. Daruka, J. Tersoff, and A.-L. Barabási. *Shape Transition in Growth of Strained Islands.* Phys. Rev. Lett., **82**, 2753 (1999).

[DeL99] P. M. DeLuca and S. A. Barnett. *An ion beam technique for real-time measurment of two-dimensional islands during epitaxial growth.* Surf. Sci., **426**, L407 (1999).

[Dob97] H. T. Dobbs, D. D. Vvedensky, A. Zangwill, J. Johansson, N. Carlsson, and W. Seifert. *Mean-Field Theory of Quantum Dot Formation.* Phys. Rev. Lett., **79**, 897 (1997).

[Dor98a] W. Dorsch, B. Steiner, M. Albrecht, H. P. Strunk, H. Wawra, and G. Wagner. *The transition from ripples to islands in strained heteroepitaxial growth under low driving forces.* J. of Crystal Growth, **183**, 305 (1998).

[Dor98b] W. Dorsch, H. P. Strunk, H. Wawra, G. Wagner, J. Groenen, and R. Carles. *Strain-induced island scaling during $Si_{x-1}Ge_x$ heteroepitaxy.* Appl. Phys. Lett., **72**, 179 (1998).

[Dou98] I. Doudevski, W. A. Hayes, and D. K. Schwartz. *Submonolayer Island Nucleation and Growth Kinetics during Self-Assembled Monolayer Formation.* Phys. Rev. Lett., **81**, 4927 (1998).

[Dow97] J. R. Downes, D. A. Faux, and E. P. O'Reilly. *A simple method for calculating strain distributions in quantum dot structures.* J. Appl. Phys., **81**, 6700 (1997).

[Eis99] H. Eisele, O. Flebbe, T. Kalka, C. Preinesberger, F. Heinrichsdorff, and A. Krost. *Cross-sectional scanning-tunneling microscopy of stacked InAs quantum dots.* Appl. Phys. Lett., **75**, 106 (1999).

[Evt99] V. P. Evtikhiev, V. E. Tokranov, A. K. Kryganovskii, A. M. Boiko, R. A. Suris, and A. N. Titkov. *Characteristics of the InAs quantum dots MBE grown of the vincinal GaAs(001) surface misoriented to the [010] direction.* Journal of Crystal Growth, **201/202**, 1154 (1999).

[Fle99] O. Flebbe, H. Eisele, T. Kalka, F. Heinrichsdorff, A. Krost, D. Bimberg, , and M. Dähne-Prietsch. *Atomic structure of stacked InAs quantum dots grown by metal-organic chemical-vapor depostion.* J. Vac. Sci. Technol. B, **17**, 1639 (1999).

[Fra49] F. C. Frank and J. H. van der Merwe. *One-dimensional dislocations. I. Static theory.* Proc. R. Soc. London, Ser. A, **198**, 205 (1949).

[Gar97] J. M. García, G. Medeiros-Ribeiro, K. Schmidt, T. Ngo, J. L. Feng, A. Lorke, J. Kotthaus, and P. M. Petroff. *Intermixing and shape changes during the formation of $InAs$ self-assembled quantum dots.* Appl. Phys. Lett., **71**, 2014 (1997).

[Gha88a] S. V. Ghaisas and A. Madhukar. *Computer simulations of the role of surface reconstruction, stoichiometry and strain in molecular beam epitaxical growth and defect formation.* In: A. Madhukar (ed.), *Proceedings of the SPIE Symposium on Growth of Compound Semiconductor Structures II*, vol. 944, 16 (SPIE Press, Bellingham, WA, 1988).

[Gha88b] S. V. Ghaisas and A. Madhukar. *Influence of compressive and tensile strain on growth mode during epitaxical growth: A computer simulation study.* Appl. Phys. Lett., **53**, 1599 (1988).

[Gha89] S. V. Ghaisas and A. Madhukar. *Kinetic aspects of growth front surface morphology and defect formation during molecular-beam epitaxy growth of strained thin films.* J. Vac. Sci. Technol. B, **7**, 264 (1989).

[Gha92] S. V. Ghaisas and S. Das Sarma. *Surface diffusion length under kinetic growth conditions.* Phys. Rev. B, **46**, 7308 (1992).

[Gla41] S. Glasstone, K. Laidler, and H. Eyring. *The theory of rate processes* (McGraw Hill, New York, 1941).

[Gro00] F. Grosse and R. Zimmermann. *Monte Carlo growth simulation for $Al_xGa_{1-x}As$ heteroepitaxy.* J. of Crystal Growth, **212**, 128 (2000).

[Gru95] M. Grundmann, O. Stier, and D. Bimberg. *InAs/GaAs quantum pyramids: strain distribution, optical phonons and electronic structure.* Phys. Rev. B, **52**, 11969 (1995).

[Hei97] F. Heinrichsdorff, N. K. M.-H. Mao, A. Krost, D. Bimberg, A. O. Kosogov, and P. Werner. *Room-temperature continuous-wave lasing from stacked InAs/GaAs quantum dots grown by metalorganic chemical vapor deposition.* Appl. Phys. Lett., **71**, 22 (1997).

[Hei98] R. Heitz, A. Kalburge, Q. Xie, M. Grundmann, P. Chen, A. Hoffmann, A. Madhukar, and D. Bimberg. *Excited states and energy relaxation in stacked $InAs/GaAs$ quantum dots.* Phys. Rev. B, **57**, 9050 (1998).

[Hel82] K. Hellwege and O. Madelung (eds.). *Landolt-Börnstein: Numerical Data and Functional Relationships in Science and Technology*, vol. III/17a (Springer, Berlin, Heidelberg, New York, 1982).

[Hey97] C. Heyn, T. Franke, R. Anton, and M. Harsdorff. *Correlation between island-formation kinetics, surface roughening, and RHEED oscillation damping during GaAs homoepitaxy.* Phys. Rev. B, **56**, 13483 (1997).

[Hir82] J. P. Hirth and J. Lothe. *Theory of Dislocations* (McGraw Hill, Tokyo, 1982).

[Hol99] V. Holý, G. Springholz, M. Pinczolits, and G. Bauer. *Strain induced vertical and lateral correlations in quantum dot superlattices.* Phys. Rev. Lett., **83**, 356 (1999).

[Hwa98] I.-S. Hwang, T.-C. Chang, and T. T. Tsong. *Exchange-Barrier Effects on Nucleation and Growth of Surfactant-Mediated Epitaxy.* Phys. Rev. Lett., **80**, 4229 (1998).

[Ipa98] I. P. Ipatova, V. G. Malyshkin, A. A. Maradudin, V. A. Shchukin, and R. F. Wallis. *Kinetic instability of semiconductor alloy growth.* Phys. Rev. B, **57**, 12968 (1998).

[Iri96] T. Irisawa and Y. Arima. *Structural feature of surface in MBE growth Monte Carlo simulation.* J. of Crystal Growth, **163**, 22 (1996).

[Ish98] A. Ishii and T. Kawamura. *Kinetics of homoepitaxial growth on $GaAs(100)$ studied by two-component Monte Carlo simulation.* Appl. Surf. Sci., **130-132**, 403 (1998).

[Ish99] A. Ishii and T. Kawamura. *Monte Carlo simulation of homoepitaxial growth on two-component compound semiconductor surfaces.* Surf. Sci., **436**, 38 (1999).

[Jen94] P. Jensen, A.-L. Barabási, H. Larralde, S. Havlin, and H. E. Stanley. *Model incorporating deposition, diffusion, and aggregation in submonolayer nanostructures.* Phys. Rev. E, **50**, 618 (1994).

[Jes98] D. E. Jesson, G. Chen, K. M. Chen, and S. J. Pennycook. *Self-Limiting Growth of Strained Faceted Islands.* Phys. Rev. Lett., **80**, 5156 (1998).

[Kam94] A. Y. Kaminskii and R. A. Suris. *2D nuclei evolution during epitaxial growth.* Sol. Stat. Comm., **89**, 697 (1994).

[Kam96] A. Y. Kaminskii and R. A. Suris. *Smoothing of crystal surfaces during growth interruption.* Appl. Surf. Sci., **104/105**, 312 (1996).

[Kan95] D. Kandel and E. Kaxiras. *Surfactant Mediated Crystal Growth of Semiconductors.* Phys. Rev. Lett., **75**, 2742 (1995).

[Käs99] M. Kästner and B. Voigtländer. *Kinetically Self-Limiting Growth of $Ge$ Islands on $Si(001)$.* Phys. Rev. Lett., **82**, 2745 (1999).

[Kat99] T. Kato, M. Uchibe, H. Tochihara, and W. Shimada. *Monte-Carlo simulation on growth patterns of DAS structure on quenched $Si(111)$ surface.* Surf. Sci., **433**, 745 (1999).

[Kau95] S. Kaufmann. *At Home in the Universe* (Oxford University Press, New York, 1995).

[Kaw66] K. Kawasaki. *Diffusion Constants near the Critical Point for Time Dependent Ising Models. I.* Phys. Rev., **145**, 224 (1966).

[Kaw99] T. Kawamura and A. Ishii. *Role of $As$ during homoepitaxial growth on $GaAs(001)$ studied using Monte Carlo simulation.* Surf. Sci., **438**, 155 (1999).

[Keg00] I. Kegel, T. H. Metzger, A. Lorke, J. Peisl, J. Stangl, G. Bauer, J. M. García, and P. M. Petroff. *Nanometer-Scale Resolution of Strain and Interdiffusion in Self-Assembled $InAs/GaAs$ Quantum Dots.* Phys. Rev. Lett., **85**, 1694 (2000).

[Kho00] K. E. Khor and S. D. Sarma. *Quantum dot self-assembly in growth of strained-layer thin films: A kinetic Monte Carlo study.* Phys. Rev. B, **62**, 16657 (2000).

[Köh00] U. Köhler, C. Jensen, C. Wolf, A. C. Schindler, L. Brendel, and D. E. Wolf. *Investigation of homoepitaxial growth on bcc surfaces with STM and kinetic Monte Carlo simulation.* Surf. Sci., **454-456**, 676 (2000).

[Kon98a] A. Konkar, R. Heitz, T. R. Ramachandran, P. Chen, and A. Madhukar. *Fabrication of strained $InAs$ island ensembles on nonplanar patterned $GaAs(001)$ substrates.* J. Vac. Sci. Technol. B, **16**, 1334 (1998).

[Kon98b] A. Konkar, A. Madhukar, and P. Chen. *Stress-engineered spatially selective self-assembly of strained $InAs$ quantum dots on nonplanar $GaAs(001)$ substrates.* Appl. Phys. Lett., **72**, 220 (1998).

[Kra98] P. Kratzer, C. G. Morgan, and M. Scheffler. *Density functional theory studies on microscopic processes of GaAs growth.* Progress in Surf. Sci., **59**, 135 (1998).

[Kra99] P. Kratzer, C. G. Morgan, and M. Scheffler. *Model for nucleation in GaAs homoepitaxy derived from first principles.* Phys. Rev. B, **59**, 2790 (1999).

[Kun90] R. Kunkel, B. Poelsema, L. K. Verheij, and G. Comsa. *Reentrant Layer-by-Layer Growth during Molecular-Beam Epitaxy of Metal-on-Metal Substrates.* Phys. Rev. Lett., **65**, 733 (1990).

[Kun00] R. Kunert. *Monte-Carlo-Simulation der Wachstumskinetik von Quantenpunkten im Nukleationsstadium.* Master's thesis, TU Berlin (2000).

[Lai91] B. Laikhtman. *Current-voltage instabilities in superlattices.* Phys. Rev. B, **44**(20), 11260 (1991).

[Lan70] L. D. Landau and E. M. Lifschitz. *Theory of elasticity* (Pergamon, New York, 1970).

[Lee98a] C. Lee and A.-L. Barabási. *Spatial ordering of islands grown on patterned surfaces.* Appl. Phys. Lett., **73**, 2652 (1998).

[Lee98b] S. Lee, I. Daruka, C. S. Kim, A.-L. Barabási, J. L. Merz, and J. K. Furdyna. *Dynamics of Ripening of Self-Assebled $II-IV$ Semiconductor Quantum Dots.* Phys. Rev. Lett., **81**, 3479 (1998).

[Leo94] D. Leonard, K. Pond, and P. M. Petroff. *Critical layer thickness for self-assembled InAs islands on GaAs.* Phys. Rev. B, **50**, 11687 (1994).

[Lev98] S. W. Levine, J. R. Engstrom, and P. Clancy. *A kinetic Monte Carlo study of the growth of $Si$ on $Si(100)$ at varying angles of incident deposition.* Surf. Sci., **401**, 112 (1998).

[Li93] W. Li, G. Vidali, and O. Biham. *Scaling of island growth in $Pb$ overlayers on $Cu(001)$.* Phys. Rev. B, **48**, 8336 (1993).

[Lia99] X. Z. Liao, J. Zou, D. J. H. Cockayne, J. Qin, Z. M. Jiang, X. Wang, and R. Leon. *Strain relaxation by alloying effects in $Ge$ islands grown on $Si(001)$.* Phys. Rev. B, **60**, 15605 (1999).

[Liu99a] B.-G. Liu, J. Wu, E. G. Wang, and Z. Zhang. *Two-dimensional pattern formation in surfactant-mediated epitaxial growth.* Phys. Rev. Lett., **83**, 1195 (1999).

[Liu99b] F. Liu, S. E. Davenport, H. M. Evans, and M. G. Lagally. *Self-Organized Replication of 3D Coherent Island Size and Shape in Multilayer Heteroepitaxial Films.* Phys. Rev. Lett., **82**, 2528 (1999).

[Liu00] C.-P. Liu, J. M. Gibson, D. G. Cahill, T. I. Kamins, D. P. Basile, and R. S. Williams. *Strain Evolution in Coherent $Ge/Si$ Islands.* Phys. Rev. Lett., **84**, 1958 (2000).

[Liu01] B.-G. Liu and E. Schöll. *Strained growth in surfactant mediated heteroepitaxy.* Vacuum, **61**, 145 (2001).

[Lor00] A. Lorke, R. J. Luyken, A. O. Govorov, J. P. Kotthaus, J. M. Garcia, and P. M. Petroff. *Spectroscopy of Nanoscopic Semiconductor Rings.* Phys. Rev. Lett., **84**, 2223 (2000).

[Mad83] A. Madhukar. *Far from equilibrium vapour phase growth of lattice matched $III$-$IV$ compound semiconductor interfaces: Some basic concepts and Monte Carlo computer simulations.* Surf. Sci., **132**, 344 (1983).

[Mad96] A. Madhukar. *A unified atomistic and kinetic framework growth front morphology evolution and defect initiation in strained epitaxy.* Journal of Crystal Growth, **163**, 149 (1996).

[Mah97] K. Mahalingam, D. L. Dorsey, K. R. Evans, and R. Venkatasubramanian. *A Monte Carlo study of gallium desorption kinetics during MBE of $(100) - GaAs/AlGaAs$ heterostructures.* J. of Crystal Growth, **175**, 211 (1997).

[Mao99] H. Mao, S. Lee, and S.-J. Park. *The Monte Carlo simulation of epitaxial growth of hexagonal $GaN$.* Surf. Sci., **432**, L617 (1999).

[Max98] M. V. Maximov, Y. M. Shernyakov, A. F. Tsatsul'nikov, A. V. Lunev, A. V. Sakharnov, V. M. Ustinov, A. Y. Egorov, A. E. Zhukov, A. R. Kovsh, P. S. Kop'ev, L. V. Asryan, Z. I. Alferov, N. N. Ledentsov, D. Bimberg, A. O. Kosogov, and P. Werner. *High-power continuous-wave operation of a InGaAs/AlGaAs quantum dot laser*. J. Appl. Phys., **83**, 5561 (1998).

[Mei97a] M. Meixner, S. Bose, and E. Schöll. *Analysis of chaotic patterns near a codimension-2 Turing-Hopf point in a reaction-diffusion model.* Physica D, **109**, 128 (1997).

[Mei97b] M. Meixner, A. De Wit, S. Bose, and E. Schöll. *Generic spatio-temporal dynamics near Turing-Hopf codimension-two bifurcations.* Phys. Rev. E, **55**, 6690 (1997).

[Mei97c] M. Meixner, P. Rodin, and E. Schöll. *Global control of front propagation in layered semiconductor structures.* phys. status solidi (b), **204**, 493 (1997).

[Mei98a] M. Meixner, P. Rodin, and E. Schöll. *Accelerated, decelerated and oscillating fronts in a globally coupled bistable semiconductor system.* Phys. Rev. E, **58**(3), 2796 (1998).

[Mei98b] M. Meixner, P. Rodin, and E. Schöll. *Fronts in a bistable medium with two global constraints: Oscillatory instability and large-amplitude limit-cycle motion.* Phys. Rev. E, **58**(5), 5586 (1998).

[Mei99] M. Meixner, P. Rodin, E. Schöll, and A. Wacker. *Dynamics and stability of lateral current density patterns in resonant-tunneling structures*. In: *Proceedings of the $7^{th}$*

*International Symposium on Nanostructure: Physics and Technology*, 280–283 (Ioffe Institute, St. Petersburg, 1999).

[Mei00a] M. Meixner, R. Kunert, S. Bose, E. Schöll, V. A. Shchukin, D. Bimberg, E. Penev, and P. Kratzer. *Monte-Carlo-Simulation des Wachstums selbstorganisierter Quantenpunkte mit anisotroper Oberflächendiffusion.* DPG-Frühjahrstagung Regensburg (2000).

[Mei00b] M. Meixner, P. Rodin, E. Schöll, and A. Wacker. *Lateral current density fronts in globally coupled bistable semiconductors with S- or Z-shaped current voltage characteristic.* Eur. Phys. J. B, **13**, 157 (2000).

[Mei00c] M. Meixner, S. Zoldi, S. Bose, and E. Schöll. *Karhunen-Loève local characterization of spatio-temporal chaos in a reaction-diffusion system.* Phys. Rev. E, **61**, 1382 (2000).

[Mei01a] M. Meixner, R. Kunert, S. Bose, E. Schöll, V. A. Shchukin, D. Bimberg, E. Penev, and P. Kratzer. *Monte Carlo simulation of the self-organized growth of quantum dots with anisotropic surface diffusion.* In: N. Miura and T. Ando (eds.), *Proc. 25th International Conference on the Physics of Semiconductors (ICPS-25), Osaka 2000*, 381 (Springer, Berlin, 2001).

[Mei01b] M. Meixner, E. Schöll, M. Schmidbauer, H. Raidt, and R. Köhler. *Formation of Island Chains in SiGe/Si Heteroepitaxy by Elastic Anisotropy – A Monte Carlo Study.* Phys. Rev. B, **64**, 245307 (2001).

[Mei01c] M. Meixner, E. Schöll, V. A. Shchukin, and D. Bimberg. *Self-assembled quantum dots: Crossover from kinetically controlled to thermodynamically limited growth.* Phys. Rev. Lett., **87**, 236101. Ibid **88**, 059901 (2002) (2001).

[Met49] N. Metropolis and S. Ulam. *The Monte Carlo method.* J. Am. Stat. Assoc., **44**, 335 (1949).

[Met53] N. Metropolis, A. W. Rosenbluth, M. N. Rosenbluth, A. H. Teller, and E. Teller. *Equation of state calculations for fast computing machines.* J. Chem. Phys., **21**, 1087 (1953).

[Mil99] M. Miller, J. Malm, A. Gustafsson, A. Petersson, S. Carlsson, and B. Gustafson. *Tall stacks of InAs quantum dots in GaAs coupled and contacted as diodes.* In: D. Gershoni (ed.), *Proceedings of the 24th Int. Conf. on the Physics of Semiconductors* (World Scientific, Singapore, 1999). Section X.B5 on CD-Rom.

[Mo91] Y.-W. Mo, J. Kleiner, M. B. Webb, and M. G. Lagally. *Activation energy for surface diffusion of $Si$ on $Si(001)$: a scanning-tunnelling-microscopy study.* Phys. Rev. Lett., **66**, 1998 (1991).

[Mo92] Y.-W. Mo, J. Kleiner, M. B. Webb, and M. G. Lagally. *Surface self diffusion of $Si$ on $Si(001)$.* Surf. Sci., **268**, 275 (1992).

[Mol96] N. Moll, A. Kley, E. Pehlke, and M. Scheffler. *GaAs equilibrium crystal shape from first-principles.* Phys. Rev. B, **54**, 8844 (1996).

[Mol98] N. Moll, M. Scheffler, and E. Pehlke. *Influence of surface stress on the equilibrium shape of strained quantum dots.* Phys. Rev. B, **58**, 4566 (1998).

[Muk98] I. Mukhametzhanov, R. Heitz, J. Zeng, P. Chen, and A. Madhukar. *Independent manipulation of density and size of stress-driven self-assembled quantum dots.* Appl. Phys. Lett., **73**, 1841 (1998).

[Muk99] I. Mukhametzhanov, Z. Wei, R. Heitz, and A. Madhukar. *Punctuated island growth: An approach to examination and control of quantum dot density, size, and shape evolution.* Appl. Phys. Lett., **75**, 85 (1999).

[Mus98] K. Mussawisade, T. Wichmann, and K. W. Kehr. *Single-particle diffusion coefficient on surfaces with Ehrlich-Schwoebel barriers*. Surf. Sci., **412**, 55 (1998).

[New99] M. E. J. Newman and T. Barkema. *Monte Carlo Methods in Statistical Physics* (Oxford University Press, Oxford, 1999).

[Ng95] K.-O. Ng and D. Vanderbilt. *Stability of periodic domain structures in a two-dimensional dipolar model*. Phys. Rev. B, **52**, 2177 (1995).

[Nie88] F. Niedermayer. *General cluster updating method for Monte Carlo simulations.* Phys. Rev. Lett., **61**, 2026 (1988).

[Nie98] F. Nieto, C. Uebing, and V. Pereyra. *The influence of surface reconstruction on the collective motion of adsorbed atoms.* Surf. Sci., **416**, 152 (1998).

[Nöt96] R. Nötzel. *Self-organized growth of quantum-dot structures*. Semicond. Sci. Technol., **11**, 1365 (1996).

[Oka98] M. Okamoto, T. Yokoyama, and K. Takayanagi. *Strain fiels around a single-dimer vacancy of $Si(100)$ surface studied by a Monte Carlo simulation.* Surf. Sci., **402-404**, 851 (1998).

[Orr92] B. G. Orr, D. Kessler, C. W. Snyder, and L. Sander. *A Model for Strain-Induced Roughening and Coherent Island Growth.* Europhys. Lett., **19**, 33 (1992).

[Par98] K.-H. Park, J. S. Ha, W. S. Yun, and E.-H. Lee. *Self-organization of uniform $Ag$ nanoclusters on Sb-terminated $Si(100)$ surface.* Surf. Sci., **415**, 320 (1998).

[Peh96] E. Pehlke, N. Moll, and M. Scheffler. *The equilibrium shape of InAs quantum dots grown on a GaAs(001) substrate*. In: M. Scheffler and R. Zimmermann (eds.), *Proc. 23rd Int. Conf. Phys. Semicond., Berlin 1996*, vol. 2, 1301–1304 (World Scientific, Singapore, 1996).

[Pen01] E. Penev, P. Kratzer, and M. Scheffler. *Effect of strain on surface diffusion in semiconductor heteroepitaxy.* Phys. Rev. B. Submitted (2001).

[Pim91] S. L. Pimm. *Balance of nature? Exological issues in the conservation of species and communities* (Plenum Press, Chicago, 1991).

[Pim98] A. Pimpinelli and J. Villain. *Physics of Crystal Growth* (Cambridge University Press, Cambridge, 1998).

[Pin98] M. Pinczolits, G. Springholz, and G. Bauer. *Direct foramtion of self-assembled quantum dots under tensile strain by heteroepitaxy of $PbSe$ on $PbTe(111)$.* Appl. Phys. Lett., **73**, 250 (1998).

[Pin99] M. Pinczolits, G. Springholz, and G. Bauer. *Evolution of hexagonal lateral ordering in strain-symmetrized $PbSe/Pb_{1-x}Eu_xTe$ quantum-dot superlattices.* Phys. Rev. B, **60**, 11524 (1999).

[Por77] K. Portz and A. A. Maradudin. *Surface contribution to the low-temperature specific heat of a cubic crystal.* Phys. Rev. B, **16**, 3535 (1977).

[Pre92] W. H. Press, B. P. Flannery, S. A. Teukolsky, and W. T. Vettering. *Numerical Recipes in C (2nd ed.)* (Cambridge University Press, Cambridge, 1992).

[Pri95] C. Priester and M. Lannoo. *Origin of Self-Assembled Quantum Dots in Highly Mismatched Heteroepitaxy.* Phys. Rev. Lett., **75**, 93 (1995).

[Pry98] C. Pryor, J. Kim, L. W. Wang, A. J. Williamson, and A. Zunger. *Comparison of two methods for describing the strain profiles in quantum dots.* J. Appl. Phys., **83**, 2548 (1998).

[Ram98] T. R. Ramachandran, A. Madhukar, I. Mukhametzhanov, R. Heitz, A. Kalburge, Q. Xie, and P. Chen. *Nature of Stranski-Krastanow growth of $InAs$ an $GaAs(001)$.* J. Vac. Sci. Technol. B, **16**, 1330 (1998).

[Rat94a] C. Ratsch. *Effects of Strain on Heteroepitaxial Growth Dynamics.* Ph.D. thesis, Georgia Institute of Technology (1994).

[Rat94b] C. Ratsch, A. Zangwill, and P. Šmilauer. *Scaling of heteroepitaxial island sizes.* Surf. Sci., **314**, L937 (1994).

[Rat94c] C. Ratsch, A. Zangwill, P. Šmilauer, and D. D. Vvedensky. *Saturation and scaling of epitaxial island densities.* Phys. Rev. Lett., **72**, 3194 (1994).

[Rat96] C. Ratsch, P. Šmilauer, A. Zangwill, and D. Vvedensky. *Mechanism for coherent island formation during heteroepitaxy.* J. Phys. I, **6**, 575 (1996).

[Rat97a] C. Ratsch, P. Ruggerone, and M. Scheffler. *Density-functional theory of surface diffusion and epitaxial growth of metals.* In: M. Tringides (ed.), *Surface Diffusion: Atomistic and Collective Processes*, NATO ASI Series B: Physics Vol. 360, 83 (Plenum Press, New York, 1997).

[Rat97b] C. Ratsch, A. P. Seitsonen, and M. Scheffler. *Strain dependence of surface diffusion: Ag(111) and Pt(111).* Phys. Rev. B, **55**, 6750 (1997).

[Rat98] C. Ratsch and M. Scheffler. *Density-functional theory calculations of hopping rates of surface diffusion.* Phys. Rev. B, **58**, 13163 (1998).

[Rob98] Y. Robach, M. Phaner, A. Solère, M. Gendry, and L. Porte. *Strain-induced formation of self-assembled nanostructures in the epitaxial growth of $InAs$ and $GaAs$ on $InP(001)$.* Appl. Phys. A, **66**, S1031 (1998).

[Ros98] F. M. Ross, J. Tersoff, and R. M. Tromp. *Coarsening of Self-Assembled $Ge$ Quantum Dots on $Si(001)$.* Phys. Rev. Lett., **80**, 984 (1998).

[Rou98] M. D. Rouhani, R. Malek, and D. Estève. *Monte Carlo simulation of mismatch relaxation and island coalescence during heteroepitaxial growth.* Thin Solid Films, **318**, 61 (1998).

[RP98] A. J. Ramirez-Pastor, J. L. Riccardo, and V. D. Pereyra. *Monte Carlo study of dimer adsorption at monolayer at square lattices.* Surf. Sci., **411**, 294 (1998).

[Saa74] A. S. Saada. *Elasticity - Theory and applications* (Pergamon, New York, 1974).

[Sar92] S. D. Sarma. *Molecular-beam epitaxial growth as a self-organized critical phenomenon.* J. Vac. Sci. Technol. B, **10**, 1695 (1992).

[Sch87] E. Schöll. *Nonequilibrium Phase Transitions in Semiconductors* (Springer, Berlin, 1987).

[Sch95] M. Schroeder and D. E. Wolf. *Magic islands and submonolayer scaling in molecular beam epitaxy.* Phys. Rev. Lett., **74**, 2062 (1995).

[Sch97a] K. H. Schmidt, G. Medeiros-Ribeiro, J. Garcia, and P. M. Petroff. *Size quantisation effects in InAs self-assembled quantum dots.* Appl. Phys. Lett., **70**, 1727 (1997).

[Sch97b] M. Schroeder and D. E. Wolf. *Diffusion on strained surfaces.* Surf. Sci., **375**, 129 (1997).

[Sch98a] P. Schittenhelm, C. Engel, F. Findeis, G. Abstreiter, A. A. Darhuber, G. Bauer, A. O. Kosogov, and P. Werner. *Self-assembled $Ge$ dots: Growth, characterization, ordering, and applications.* J. Vac. Sci. Technol. B, **16**, 1575 (1998).

[Sch98b] M. Schmidbauer, T. Wiebach, H. Raid, M. Hanke, R. Köhler, and H. Wawra. *Ordering of self-assembled $Si_{1-x}Ge_x$ islands studied by grazing incidence small-angle x-ray scattering and atomic force microscopy.* Phys. Rev. B, **58**, 10523 (1998).

[Sch98c] M. Schmidbauer, T. Wiebach, H. Raidt, M. Hanke, R. Köhler, and H. Wawra. *Self-organized ordering of $Si_{1-x}Ge_x$ nanoscale islands studied by grazing incidence small-angle x-ray scattering.* J. Phys. D: Appl. Phys., **32**, A230 (1998).

[Sch98d] Schöll and S. Bose. *Kinetic Monte Carlo Simulation of the Nucleation Stage of the Self-organized Growth of Quantum Dots.* Sol. State El., **42**, 1587 (1998).

[Sch01] E. Schöll. *Nonlinear spatio-temporal dynamics and chaos in semiconductors* (Cambridge University Press, Cambridge, 2001). Nonlinear Science Series, Vol. 10.

[Shc95a] V. A. Shchukin, A. J. Borovkov, N. N. Ledentsov, and D. Bimberg. *Tuning and breakdown of faceting under externally applied stress.* Phys. Rev. B, **51**, 10104 (1995).

[Shc95b] V. A. Shchukin, N. N. Ledentsov, P. S. Kop'ev, and D. Bimberg. *Spontaneous ordering of arrays of coherent strained islands.* Phys. Rev. Lett., **75**, 2968 (1995).

[Shc98a] V. A. Shchukin and D. Bimberg. *Strain-driven self-organisation of nanostructures on semiconductor surfaces.* Appl. Phys. A, **67**, 687 (1998).

[Shc98b] V. A. Shchukin, D. Bimberg, V. G. Malyshkin, and N. N. Ledentsov. *Vertical correlations and anticorrelations in multisheet arrays of two-dimensional islands.* Phys. Rev. B, **57**, 12262 (1998).

[Shc99a] V. Shchukin and D. Bimberg. *Spontaneous ordering of nanostructures on crystal surfaces.* Rev. Mod. Phys., **71**, 1125 (1999).

[Shc99b] V. A. Shchukin. *Green's tensor in elastically anisotropic cubic crystals.* Private communication (1999).

[Shc00] V. A. Shchukin, N. N. Ledentsov, and D. Bimberg. *Spontaneous formation of arrays of strained islands: Thermodynamics versus kinetics.* In: *Mat. Res. Soc. Symp. Proc. V.*, vol. 583, 23 (Pittsburgh, USA, 2000).

[Shk98] A. A. Shklyaev, M. Shibata, and M. Ichikawa. *$Ge$ islands on $Si(111)$ at coverages near the transition from two-dimensional to three-dimensional growth.* Surf. Sci., **416**, 192 (1998).

[Sol96] G. S. Solomon, J. A. Trezza, A. F. Marshall, and J. S. Harris. *Vertically Aligned and Electrically Coupled Growth Induced $InAs$ Islands on $GaAs$.* Phys. Rev. Lett., **76**, 952 (1996).

[Spr94] G. Springholz, N. Frank, and G. Bauer. *Surface roughening transition and critical layer thickness in strained-layer heteroepitaxy of $EuTe$ on $PbTe(111)$.* Appl. Phys. Lett., **64**, 2970 (1994).

[Spr98] G. Springholz, V. Holý, M. Pinczolits, and G. Bauer. *Self-Organized Growth of Three-Dimensional Quantum-Dot Crystals with fcc-like Stacking and Tunable Lattice Constant.* Science, **282**, 734 (1998).

[Spr00] G. Springholz, M. Pinczolits, P. Mayer, V. Holy, G. Bauer, H. H. Kang, and L. Salamanca-Riba. *Tuning of vertical and lateral correlations in self-organized $PbSe/Pb_{1-x}Eu_xTe$ quantum dot superlattices.* Phys. Rev. Lett., **84**, 4669 (2000).

[Ste97] E. Steimetz, F. Schienle, J.-T. Zettler, and W. Richter. *Stranski-Krastanov formation of InAs quantum dots monitored during growth by reflectance anisotropy spectroscopy and spectroscopic ellipsometry.* Journal of Crystal Growth, **170**, 208 (1997).

[Sto94] P. Stolze. *Simulation of surface defects.* J. Phys.: Condens. Matter, **6**, 9495 (1994).

[Str39] I. N. Stranski and L. Krastanow. *Sitzungsberichte der Akademie der Wissenschaften in Wien.* Akad. Wiss. Lit. Mainz Math.-Natur. Kl. IIb, **146**, 797 (1939).

[Str98] M. Strassburg, V. Kutzer, U. W. Pohl, A. Hoffmann, I. Broser, N. N. Ledentsov, D. Bimberg, A. Rosenauer, U. Fischer, D. Gerthsen, I. L. Krestnikov, M. V. Maximov, P. S. Kop'ev, and Z. I. Alferov. *Gain studies of (Cd, Zn)Se quantum islands in a ZnSe matrix.* Appl. Phys. Lett., **72**, 942 (1998).

[Swe87] R. H. Swendsen and J.-S. Wang. *Nonuniversal, critical dynamics in Monte Carlo simulations.* Phys. Rev. Lett., **58**, 86 (1987).

[Tan97] S. Tan, A. Ghazali, and J.-C. S. Lévi. *Monte Carlo simulation of epitaxial growth on a* $(111)$ *layer with mismatch.* Surf. Sci., **377-379**, 997 (1997).

[Tei98] C. Teichert, J. C. Bean, and M. C. Lagally. *Self-organized nanostructures in* $Si_{1-x}Ge_x$ *films on* $Si(001)$. Appl. Phys. A, **67**, 675 (1998).

[Ter94] J. Tersoff, A. W. D. van der Gon, and R. M. Tromp. *Critical Island Size for Layer-by-Layer Growth.* Phys. Rev. Lett., **72**, 266 (1994).

[Ter95] J. Tersoff. *Step energies and roughening of strained layers.* Phys. Rev. Lett., **74**, 4962 (1995).

[Ter96] J. Tersoff, C. Teichert, and M. G. Lagally. *Self-Organization in Growth of Quantum Dot Superlattices.* Phys. Rev. Lett., **76**, 1675 (1996).

[Ter98] J. Tersoff. *Enhanced Nucleation and Enrichment of Strained-Alloy Quantum Dots*. Phys. Rev. Lett., **81**, 3183 (1998).

[Tür96] K. Türmer, R. Koch, P. Schilbe, and K. H. Rieder. *Pyramidal growth on bcc*$(001)$ *stabilises facets close to* $\{012\}$*: A Monte Carlo study.* Surf. Sci., **395**, 12 (1996).

[Ven84] J. A. Venables, G. D. T. Spiller, and M. Hanbücken. *Nucleation and growth of thin films.* Rep. Prog. Phys., **47**, 399 (1984).

[Vin57] G. Vineyard. *Frequency factors and isotope effects in solid state rate processes.* J. Phys. Chem. Solids, **3**, 121 (1957).

[Vog99a] P. Vogt, A. M. Frisch, T. Hannappel, S. Visbeck, F. Willig, C. Jung, N. Esser, W. Braun, and W. Richter. *Atomic Surface Structure of MOVPE-Grown InP(001).* phys. status solidi (b), **215**, 737 (1999).

[Vog99b] P. Vogt, T. Hannappel, S. Visbeck, K. Knorr, N. Esser, and W. Richter. *Atomic surface structure of the phosphorous-terminated InP(001) grown by MOVPE*. Phys. Rev. B, **60**, R5117 (1999).

[Vol26] M. Volmer and A. Weber. *Novel growth mechanism in heteroepitaxial semiconductor growth.* Z. Phys. Chem., **119**, 277 (1926).

[Wan91] R. Q. Wang, J. Schröder, C. Günther, and R. J. Behm. *Fractal growth of two-dimensional islands: $Au$ on $Ru(0001)$.* Phys. Rev. Lett., **67**, 3279 (1991).

[Wan97] X. Wang, Z. Jiang, H. Zhu, F. Lu, D. Huang, and X. Liu. *Germanium dots with highly uniform size distribution grown on $Si(100)$ substrate by molecular beam epitaxy.* Appl. Phys. Lett., **71**, 3543 (1997).

[Wan99] L. G. Wang, P. Kratzer, M. Scheffler, and N. Moll. *Formation and stability of self-assembled coherent islands in highly mismatched heteroepitaxy.* Phys. Rev. Lett., **82**, 4042 (1999).

[Wan00] Z. Wang, Y. Li, and J. B. Adams. *Kinetic lattice Monte Carlo simulation of facet growth rate.* Surf. Sci., **450**, 51 (2000).

[Wat97] T. Watanabe, T. Hoshino, and I. Ohdomari. *Monte Carlo study on formation of periodic structures on $Si(111)$ surfaces.* Surf. Sci., **389**, 375 (1997).

[Wic94] D. K. Wickenden, C. B. Bargeron, W. A. Bryden, J. Miragliotta, and T. J. Kistenmacher. *High quality self-nucleated $Al_xGa_{1-x}N$ layers on $(00.1)$ sapphire by low-pressure metalorganic chemical vapor deposition.* Appl. Phys. Lett., **65**, 2024 (1994).

[Wol89] U. Wolff. *Collective Monte Carlo updating for spin systems.* Phys. Rev. Lett., **62**, 361 (1989).

[Xia88] R.-F. Xiao, J. I. D. Alexander, and F. Rosenberger. *Morphological evolution of growing crystals: A Monte Carlo simulation.* Phys. Rev. A, **38**, 2447 (1988).

[Xie94] Q. Xie, P. Chen, and A. Madhukar. *InAs island-induced-strain driven adatom migration during GaAs overlayer growth.* Appl. Phys. Lett., **65**, 2051 (1994).

[Xie95a] Q. Xie, N. P. Kobayashi, T. R. Ramachandran, A. Kalburge, P. Chen, and A. Madhukar. *Strained coherent $InAs$ quantum box islands on $GaAs(100)$: Size equalization, vertical self-organization, and optical properties.* J. Vac. Sci. Technol. B, **14**, 2203 (1995).

[Xie95b] Q. Xie, A. Konkar, A. Kalburge, T. R. Ramachandran, P. Chen, R. Cartland, A. Madhukar, H. T. Lin, and D. H. Rich. *Structural and optical behavior of strained $InAs$ quantum boxes grown on planar and patterned $GaAs(100)$ substrates by molecular-beam epitaxy.* J. Vac. Sci. Technol. B, **13**, 642 (1995).

[Xie95c] Q. Xie, A. Madhukar, P. Chen, and N. P. Kobayashi. *Vertically self-Organized InAs Quantum Box Islands on GaAs(100).* Phys. Rev. Lett., **75**, 2542 (1995).

[Zan88] A. Zangwill. *Physics at surfaces* (Cambridge University Press, Cambridge, 1988).

[Zha64] A. M. Zhabotinskii. *Periodic processes of the oxidation of malonic acid in solution.* Biofizika, **9**, 306. Study of the kinetics of Belousov's reaction (1964).

[Zha97] C.-M. Zhang, M. C. Bartelt, J.-M. Wen, C. J. Jenks, J. W. Evans, and P. A. Thiel. *The initial stages of $Ag/Ag(001)$ homoepitaxy: scanning tunneling microscopy experiments and Monte Carlo simulations.* J. of Crystal Growth, **174**, 851 (1997).

[Zha98] C.-M. Zhang, M. C. Bartelt, J.-M. Wen, C. J. Jenks, J. W. Evans, and P. A. Thiel. *Submonolayer island formation and the onset of multilayer growth during $Ag/Ag(100)$ homoepitaxy.* Surf. Sci., **406**, 178 (1998).

[Zha99] T.-C. Zhang, I.-S. Hwang, and T. T. Tsong. *Direct Observation of Reaction-Limited Aggregation on Semiconductor Surfaces.* Phys. Rev. Lett., **83**, 1191 (1999).

[Zhd99] V. P. Zhdanov and B. Kasemo. *Nontraditional models of Ostwald ripening on solid surfaces: from physics to biology*. Surf. Sci., **437**, 307 (1999).